Nanoindentations in Kinking Nonlinear Elastic Solids

A Thesis

Submitted to the Faculty

of

Drexel University

by

Anand Murugaiah

in partial fulfillment of the

requirements for the degree

of

Doctor of Philosophy

May 2004

ACKNOWLEDGMENTS

I am very grateful to a lot of people who were instrumental in my studies at Drexel University.

First, I would like to thank my advisors, Dr. Michel W. Barsoum and Dr. Surya Kalidindi for their help, guidance, support and patience during trying times. I have learnt so much under their tutelage. They have been there always to correct me, guide me, motivate me and work with me. I am truly fortunate to have them as my advisors. I am grateful to Dr. Tamer El-Raghy for his help and guidance during my research. I am very thankful to my thesis committee: Prof. Yury Gogotsi, Dr. David Stepp (Army Research Labs) and Dr. El-Raghy for their time, help and assistance in helping me complete my work.

I also would like to thank the Department of Materials Science and Engineering, the faculty, staff and my dear colleagues for their support and those wonderful moments that I shared with them. I would like to thank my family and friends for being there for me when I needed them.

I would like to thank Prof. Y. Gogotsi again for many stimulating and useful discussions and Mr. Thomas F. Juliano, for his help with the nanoindenter. I am also grateful to Dr. T. El-Raghy of 3-ONE-2 LLC for supplying the Ti_3SiC_2 samples. The graphite single crystals were provided by Prof. John A. Jaszczak of Michigan Tech. Dr. S. Piñol, ICMAB, Barcelona, Spain, is gratefully acknowledged for providing the melt textured YBCO samples used herein. Purchase of the Raman spectrometer and FESEM were supported by NSF grants DMR-0116645 and BES-0216343.

I would like to thank Drexel University, DMR Division of National Science Foundation NSF–DMR – 0072067, Army Research Office, DAAD19-00-1-0435 and DAAD19-03-1-0213, and the Office of the Naval Research ONR – N-00014-01-1-0106 for their financial support that made this work possible.

TABLE OF CONTENTS

LIST OF TABLES vi

LIST OF FIGURES vii

ABSTRACT xv

CHAPTER 1: INTRODUCTION 1

1.1 Background 1

1.1.1 Graphite – a century old mystery 1

1.1.2 Deformation in Mica and understanding in geology 7

1.1.3 Deformation in MAX phases 12

1.2 Motivation 17

1.3 Research Goals and Objectives 17

CHAPTER 2: NANOINDENTATION THEORY AND EXPERIMENTAL METHODS 19

2.1 Introduction 19

2.2 Nanoindentation Stress and Strain 21

2.3 Work Done 26

2.4 Nanoindentation Testing Parameters 28

2.5 Sample Description, Processing and Preparation 29

2.5.1 Hot Pressing of Ti_3SiC_2 30

2.5.2 Graphite 31

2.5.3 Mica 33

2.5.4 $YBa_2Cu_3O_{6.5}$ 34

CHAPTER 3: SPHERICAL NANOINDENTATIONS AND KINK BANDS IN Ti_3SiC_2 35
3.1 Introduction 35

3.2 Experimental Details 36

3.3 Results 46

3.3.1 Loading Normal to the c-axis 37

3.3.2 Loading Parallel to the c- axis 45

3.3.3 Dissipated Work 54

3.4 Discussion 56

CHAPTER 4: KINK BANDS, NONLINEAR ELASTICITY AND NANOINDENTATIONS IN GRAPHITE 65
4.1 Introduction 65

4.2 Experimental Details 67

4.3 Results 68

4.4 Discussion 75

4.4.1 Raman spectroscopy 82

4.4.2 Relationship to Previous Work on Graphite and Ti_3SiC_2 85

CHAPTER 5: KINKING NONLINEAR ELASTIC SOLIDS, NANOINDENTATIONS AND GEOLOGY 91
5.1 Introduction 91

5.2 Experimental Details 92

5.3 Results and Discussion 92

5.3.1 Grade C mica 93

5.3.2 Grade B mica 97

5.3.3 Grade A mica 102

5.3.4 Compression tests 107

CHAPTER 6: EVIDENCE THAT $YBa_2Cu_3O_6$ IS A KINKING NONLINEAR ELASTIC SOLID 113
6.1 Introduction 113

6.2 Experimental Details 114

6.3 Results and Discussion 115

CHAPTER 7: CONCLUSIONS AND FUTURE WORK 122

7.1 Conclusions 122

8.2 Future Work 132

LIST OF REFERENCES 134

APPENDIX A: TAPE CASTING, PRESSURELESS SINTERING AND GRAIN GROWTH IN Ti_3SiC_2 COMPACTS 140
A.1 Introduction 140

A.2 Experimental Details 143

A.2.1 Tape Casting 143

A.2.2 Cold Pressing 145

A.3 Results and Discussion 147

VITA 169

LIST OF TABLES

1. Stiffness values of graphite.....5

2. Summary of grain size results as a function of the various heat treatments And anneals carried out in this work 152

LIST OF FIGURES

1. Layered crystal structure of graphite 3

2. Hysteresis observed in bulk polycrystalline graphite in simple compression 6

3. Structure of Mica (Muscovite).....8

4. Possible dislocations and dislocation partials in mica 9

5. Schematic of stress strain response observed in rocks and mica in simple compression 10

6. Rudimentary element of the hysteretic mesoscopic units (HMUs) 11

7. Crystal structure of the MAX phases.....13

8. Hysteretic behavior observed in simple compression tests of Ti_3SiC_2 up to 1 GPa 16

9. Schematic of indentation with a spherical indenter, showing the actual area of contact, at small indentation depths (hc << R). 22

10. Load-displacement and stress strain curves for as obtained data and with correction. The inclined dashed lines in the stress strain curves correspond to a modulus of 320 GPa.....25

11. Comparison of area under elastic stress strain curves for simple compression and nanoindentations for Ti_3SiC_2 and graphite. A modulus value of 325 GPa was used for Ti_3SiC_2 and 36.5 GPa for graphite.....28

12. Custom built sample ball holder for mounting the graphite samples that fits in the nanoindenter, FESEM and Raman microspectrometer.....32

13. Typical microstructures of different grades of mica used: grades A, B, and C 34

14. a) Typical load vs. depth-of-indentation response of a Ti_3SiC_2 surface for which the loading direction is normal to the c-axis. (Sketch on left in this and most other figures shows the indenter/c-axis arrangement). Five curves are shown; three show extensive pop-ins that resulted in delamination cracks shown in the accompanying SEM micrograph; the other two did not delaminate and no trace of the indentation was found in the SEM. Note stochastic nature of load at which the pop-ins occur. b) Same as a, but for repeat indentations, in the same location, to a maximum load of 200 mN. Note first loop is open, but following 4 are closed. c) Expands the low load region. Major hardening occurs between the first and second cycles. d) Contact stress vs. strain for results shown in b. Note full reversibility of repeat loops. e) Contact stress vs. strain for 4 different loads on four different locations. The inclined dashed lines corresponds to modulus of 320 GPa.....38

15. a) Load displacement for indentation normal to the c-axis up to 10 mN. b) Corresponding contact stress vs. strain – note repeatability and reversibility even from the first indents. c) Load displacement curves parallel to the c-axis up to 10 mN. First cycle is characterized by large deformations and low stresses. Second and subsequent cycles are almost identical in shape and size. d) Corresponding contact stress vs. strain; the short inclined colored lines are guides to the eye showing the feeble dependence, if any, of yield points on total strain. However, the subsequent indents have much higher stresses, though loaded to the same maximum load of 10 mN. Such a situation is not possible. e and f) Load displacement and stress strain with corrections for apparent permanent displacement of the first indent – the unloading curves in the stress strain match very well for a modulus of 325 GPa (black dotted line) 42

16. a) Typical load vs. depth-of-indentation response of a Ti_3SiC_2 surface for which the c-axis is normal to the surface. Three curves are shown for 3 different indent locations. In this direction, large pop-ins were not observed; instead features that resembled kinks in carpets shown in SEM micrograph were observed. b) Same as a, but for repeat indentations, in the same location, to a maximum load of 100 mN. c) Expands the low load region. Major hardening occurs between the first and second loops. Note first loop is open, but following 4 appear closed. d) Contact stress vs. strain curves for results shown in b. e) Contact stress vs. strain at 500mN on 3 different locations. Note stochastic nature of the yield points. Also note 3 regions; a linear elastic region; a region II where the hardening is rapid; and region III, where the hardening rate is lower. In both d and e, the parallel inclined dashed lines were drawn assuming a modulus of 320 GPa 46

17. Typical Load displacements and stress strain on fine grained Ti_3SiC_2 (Random orientation of grains). a and b) 10mN, c and d) 100mN, e and f) 500mN, g and h) SEM micrograph of indents at 200mN (g) and 500mN (h).....50

18. a) Log-log plot of energy dissipated per cycle, W_d, versus maximum stress applied, σ for Ti_3SiC_2. The results in the lower left hand corner were obtained from simple compression results of bulk samples[22]. The ones in the upper right were obtained from the stress-strain curves generated in this work. The agreement is good despite the over 6 orders of magnitude range in W_d. The corresponding results for graphite are also shown [51]. b) Same plot but with both axes normalized by either the Young's moduli (bulk) or c_{33}. For Ti_3SiC_2, 325 GPa was used, for graphite 36.5 GPa [1] and for mica 61 GPa [77] 55

19. Schematic of an incipient kink band (IKB), with dimensions α and β. The applied stress keeps the dislocation walls apart that are attached at the ends. The IKB will collapse once the applied stress is removed due to the strong attractive nature of the dislocations 58

20. Typical low load vs. depth-of-indentation response of Ti_3SiC_2 for which: a) Indentations are parallel to the c-axis. The indentations at 5 mN are reproducible Reloading to the same area to 10 mN results in the loop labeled 1st 10 mN indent. On further loadings (2nd 10 mN indent), hardening beyond $\approx$ 5 mN is observed. b) Indentations are normal to the c-axis. Note lack of hardening. Also included in both figures in way of reference are the indentation results for fused silica 61

21. Schematic of, a) Incipient kink band comprised of two walls of dislocations of opposite polarity. As long as the walls remain attached, a strong restoring force exists. b) Same as a, but after the formation of a pair of glissile walls. Note the latter could not have formed without delamination. c) Formation of two IKBs under the indenter. d) same as c, but after massive delaminations and transfer of material from under the indenter to the edges of the indent. Note the crucial role the KBs play in that process. e) Same as c, but after retraction of the indenter, showing possible relaxation 66

22. Spherical indents along the 0001 direction in graphite single crystals, a) Multiple indents at 2, 5 and 10 mN. Only the first two successive indents at each loading are shown for clarity. Note softening in the first loading at 10mN load cycle between 5 and 10 mN. Second and subsequent indents to 10 mN are harder than the first. b) Stress vs. strain curves obtained from results shown in a. Low load indentations show full reversibility, but at 10 mN, the first loop is open. c) Stress vs. strain curves for cyclic loading at 10 mN. First cycle in open; subsequent indents are fully reversible and repeatable with a reproducibility that is noteworthy..... 68

23. a) Load vs. depth-of- indentation response of graphite single crystals loaded along the 0001 direction to 200 mN. The first indent results in an open loop but subsequent indents are harder and their loops encompass a smaller area. Inset shows SEM micrograph of indented area. b) Stress/strain curves for results shown in a. The first loop is open, but subsequent loops are almost fully reversible. A dotted straight line drawn during initial unloading corresponds very well to the elastic loading slope.....72

24. Cyclic loading to 400 mN three times. Massive pop- in observed during second loading. Note hardening subsequent to the pop-in. Third loading is characterized by a bend at ˜ 55 μm. Inset shows details of first and third indentations. b) Nanoindentation with Berkovich indenter: Extensive "pop-ins" or discontinuities resulted in damage even at small loads. Inset magnifies the indentations up to 2 mN. Note fully reversible nature of the loops.....74

25. Compressive cyclic loading-unloading stress-strain curves of polycrystalline graphite at room temperature. a) Successively higher stresses from 36MPa up to 75MPa. b) Cyclic test at 83Mpa. In order to maintain sample alignment, the minimum stress in all tests was about 1–3 MPa 76

26. FESEM secondary micrographs of, a) spherical nanoindentation at 400 mN, the damage crater has a 6 fold symmetry (denoted by a dotted hexagon); b) Berkovich indentation at 10 mN; c) Higher magnification of a, focusing on core of the indentation. Note scale of subgrains; d) Higher magnification of a focusing on edge of the indentation crater clearly showing the formation of kink bands and delaminations. Note such features cannot be formed by any other process 80

27. : Comparison of the Raman spectra obtained from a pristine area (red), and one subjected to a 200 mN spherical indentation (blue). The D-bands at 1360 cm^{-1} are only observed at loads 200 mN or higher 83

28. Raman mapping (dotted rectangle) of spherical nanoindents at 50 mN and 200 mN. a) FESEM micrograph of indented region. Region under the 200 mN indent is visible on the right; the 50 mN indent is invisible. The location of the latter is marked by red circle. b) Full widths at half max of G-band, and c) Intensity of D-band. Note absence of broadening of G-band at the 50 mN indent location and the absence of the D-band in the 50 mN location but their presence under the location of the 200 mN indentation 84

29. Load vs. depth of penetration for the 3 micas studied: Grade A, B and C, the difference between the qualities of the micas are evident from their load displacement. Higher population of defects results in larger hysteresis.....93

30. Variability and scatter in grade C mica. The load displacement response was strongly dependent on the location of the indentation. In case of no pop-ins at higher loads or in cases such as the ones marked as X above, the load displacement showed typical hysteresis loops and good reproducibility between the first and subsequent cycles. The loops marked as Y above are the same as shown in Fig. 1 for grade C mica 94

31. Load displacement response in grade C mica at 50mN. No hardening observed even after the first cycle in this case. b) Stress strain response of a). The initial loading modulus is only 20GPa as compared to 61 GPa for higher quality micas. Back extrapolated indentation yield point is around 0.7 to 0.8 GPa, after which the sample does *not* undergo strain hardening. Also the first and the subsequent loops are identical – no evidence for hardening observed 96

32. a) Typical load vs. depth-of-indentation curves obtained with a spherical diamond indenter, loaded several times in the same location. b) Magnified at low loads, showing repeatability of multiple indents 98

33. Corresponding stress/strain curves for data shown in a. In both cases only cycles 1, 2 and 5 are shown. During unloading, the dotted line represents extrapolation from the initial unloading slope that intersects the loading slope at the origin - indicating full reversibility. The deviation of the data points from the dotted line is most probably due to experimental artifact and noise. Inset is a schematic of how a microstructurally dependent, IKB-based, hysteretic element would behave on loading and unloading 99

34. Loading to higher loads in many cases resulted in pop-ins. b) Load displacement curves showing pop-in during the first indent. Subsequent indents, however, were reproducible. b) Field emission SEM micrographs of indents in mica after massive penetration of the indenter at low magnification showing indent and characteristic pileup around indentation, inset shows the breakup of the pristine sheets of mica into a multitude of smaller domains. c) Higher magnification showing kinks denoted by red arrows. Inset shows typical delaminations.....100

35. a) Typical load vs. depth of penetration for grade A mica at higher loads. A Hertzian response is also plotted (black line). b) Corresponding stress strain response, there is change in modulus value from 61 GPa to 67 GPa, at about 4 GPa in this case, denoted by the arrow 103

36. Hysteretic response observed in grade A micas – a) Load displacement at 200 mN - note full scale or reversibility in the load displacement loops. Also plotted (in blue) is elastic response observed in some locations, plotted here for comparison. b) Corresponding stress strain loops. The black dotted line during loading corresponds to a modulus of 61 GPa. The modulus value during unloading is 67 GPa (dotted red line), similar to what is observed as in cases of purely elastic response 104

37. a) Load vs. displacement showing distinct pop-ins during loading. Further repeated loadings resulted in almost reversible hysteresis loops and repeatability of such pop-ins. The insets show the displacement due to pop-ins ≈ 30 nm and the apparent residual displacement ≈ 18 nm, which is less than the displacement due to pop-ins. This implies the sub-surface delaminations/cracks heal after the load is removed. b) Corresponding stress strain curves show a higher modulus during unloading despite the pop-ins. The loading modulus is 61 GPa (black dotted line) and the unloading modulus (blue dotted line) in this particular case was 120 GPa 106

38. a) Sudden and massive pop-ins at higher loads (500mN) in grade A micas - similar to those observed in grade B at high loads, resulting in permanent deformation. b) due to delamination/damage of the mica layers exposed as a crater. Multiple loading on the same location resulted in loops that were repeatable 108

39. Stress-strain curves obtained by compressing Maycor™ (Ceramic Products Inc, Palisades Park, NJ) cylinders (12.7 mm in diameter; 31mm long). Testing was carried out on a MTS 810 testing machine in load-control mode. The loading and unloading rate were 3kN/second; the strain was measured using a MTS axial extensometer (25mm gauge length) attached directly to the sample 108

40. a) Load vs. depth-of-penetration results for a (001) surface of $YBa_2Cu_3O_6$ containing ≈ 20 vol. % Y_2BaCuO_5 loaded with a 13.5 μm spherical indenter five times in the same location. Cycles 2 to 5 were shifted to the right such that their unloading curves coincided with the first unloading curve. b) Stress-strain of results shown in a. Dashed lines are all parallel to each other, and correspond to a modulus ≈ c_{33} of 150 GPa. Note excellent reproducibility of the repeat cycles in both a and b 116

41. Log-log plot of W_d, versus maximum stress applied for $YBa_2Cu_3O_6$, bulk Ti_3SiC_2[6] and graphite[9], as well as from nanoindentations in Ti_3SiC_2[8] and single crystal graphite[9]. The W_d values for $YBa_2Cu_3O_6$ are comparable to those of Ti_3SiC_2.....120

42. Field emission SEM micrographs of indents on a (001) $YBa_2Cu_3O_6$ surface containing ≈ 20 vol.% Y_2BaCuO_5 (bright phase in micrographs) at: a) low magnification showing indent and characteristic pileup around indentation; b) Higher magnification showing the breakup of the pristine surface into a multitude of smaller domains as a result of the indentation, a necessary component of our model 121

43. Schematic of tape casting process.....143

44. SEM image of the cross section of dried tape.....145

45. Schematic of the fixture used for layering powder in layers 147

46. XRD of Ti_3SiC_2: **a**) as-received powders where the grains are randomly oriented; **b**) Top surface of tape cast and sintered sample, **c**) Top surface of tapped and sintered sample - note intensity of the 008 peaks.....149

47. Typical OM micrographs of polished and etched cross sections of tape cast and sintered Ti_3SiC_2: **a**) Cross-section near corner of sample annealed at 1600 °C for 4 hrs. Note each protrusion represents one tape cast film. **b**) Same as **a**, but emphasizing the differences in size between surface and core grains. White specs in microstructure are TiC_x particles. **c**) Same as a, after further annealing at 1600 °C for 24 hrs. Note center grains are now significantly larger. **d**) Effect of cracks in green body on grain growth.....150

48. Results of grain growth study carried out at 1600 °C in Ar on samples made from the tapped and cold pressed powders. Dashed line represents sample sintered initially in the presence of silicon in a vacuum furnace and subsequently sintered in Ar for 24 hrs. 155

49. Typical OM micrographs of tapped and sintered Ti_3SiC_2 sample sintered at 1600 °C for 24 hrs. a) Top view showing large plate-like grains with their basal planes mostly parallel to the surface. b) Cross-section showing large surface grains. c) In vicinity of cracks, the grains are larger than the core grains. In all micrographs, the white specs are TiCx.....156

50. OM micrographs of sintered Ti_3SiC_2 sample made by building oriented powders layers, one at a time - sintered at 1600 °C for 24 hrs. a) Cross section showing both large surface grains and smaller core grains. b) Grains near the surface. The results were similar to tapped and sintered samples.....159

51. OM micrographs of tapped and sintered Ti_3SiC_2 sample covered with loose Ti_3SiC_2 powders, sintered at 1600 °C for 24 hrs. The surface grains are larger than the core grains. The loose powder surrounding the sample has also densified, the sample had lesser TiC_x.....161

52. Micrographs of Ti_3SiC_2 compacts sintered for 8 hrs and 1650 °C for sample where 10 wt.% Si was mixed with Ti_3SiC_2. a) OM micrograph showing almost no TiC. b) Large voids in the sample possibly due to Si melting and forming aggregates. c) Backscattered SE image of one of the voids showing the plate like grains of Ti_3SiC_2. d) Backscattered SE image in another void showing evidence of a liquid phase that collected through the tiny pores or conduits. e) Magnified image of some of the tiny pores.....162

53. OM micrographs of Ti_3SiC_2 compacts sintered for 8 hrs and 1650 °C for: a) Ti_3SiC_2 compact was placed near, but not in contact with, silicon (note almost total absence of TiC_x). b) Control sample with no Si.....165

54. a) Backscattered SEM micrograph of cross-section of a Ti_3SiC_2 compact sintered near but not in contact with Si. Note dark grain boundary phase, which is most probably$TiSi_2$. Etching the samples dissolves the $TiSi_2$ in the grain boundaries. b) OM of sample shown in a, after further sintering further in Ar, with no Si present. There is no evidence for silicide phases 167

ABSTRACT

Nanoindentations in Kinking Nonlinear Elastic Solids

Anand Murugaiah

Dr. Michel W. Barsoum and Dr. Surya R. Kalidindi

In this work we claim that all solids with high c/a ratios that do not twin are members of a large class of solids labeled kinking non-linear elastic, KNE, solids. These include materials such as micaceous solids, layered silicates and rocks that form the bulk of the earth's surface, graphite, layered ternary carbides and nitrides such as the $M_{n+1}AX_n$ phases, layered oxides, super conductors and semiconductors, boron nitride and probably ice among others. These solids are typically layered and are characterized by fully or near fully reversible stress strain hysteresis loops exhibiting nonlinear elastic behavior, hysteresis and discrete memory. Many materials near earth's surface exhibiting such behavior are modeled phenomenologically by invoking the presence of hysteretic mesoscopic units, (HMUs), whose physical underpinnings are unknown. Similarly the underlying mechanisms of such response of other materials in these KNE solids are not well understood to date, even though some of them have been studied for over a century.

Nanoindentation experiments with a spherical indenter were used to probe the mechanical properties of some of these materials – Ti_3SiC_2, single crystal graphite, mica single crystals and layered superconductor - tetragonal $YBa_2Cu_3O_6$, at very high stresses at the crystal level. Multiple indents on the same location were carried out to study the effect of cycling and it was observed that the first indent usually resulted in a permanent deformation and the subsequent indents resulted in fully reversible, hysteretic response.

Our results, together with much of the literature on the mechanical properties of these layered solids, can be explained by invoking the formation of dislocation based incipient kink bands, IKB's, that give way to mobile dislocation walls that, in turn, coalesce into kink boundaries with increasing stress. The IKB's are fully reversible; the dislocation walls result in plastic deformation, and the kink boundaries result in hardening. Herein we show microstructural evidence for kink bands and the formation of a multitude of subgrains under the indenter.

Remarkably, these dislocation-based mechanisms allow repeated loading without damage, while dissipating significant amounts of energy during each cycle. Since the dislocations are confined to the basal planes, they cannot entangle and can thus move reversibly over relatively large distances resulting in the dissipation of substantial amounts (up to 300 MJ/m^3) of energy (the work done W_d) during each cycle. The values of the work done W_d normalized by the corresponding modulus for these solids along the indenting direction measured herein were in excellent agreement for all these layered solids, confirming that the same mechanisms are operative for these materials despite their differences in the nature of their bonding and the stress levels.

CHAPTER 1: INTRODUCTION

1.1 Background

Layered solids are ubiquitous in nature, rocks, micaceous solids and minerals, ice, graphite, layered superconductors, layered ternary carbides and nitrides (namely the MAX phases), and boron nitride are but a few examples. These materials and their properties have shaped our world, literally, from buildings that are constructed on the surface of the earth to materials used in technological applications such as graphite and other layered engineering materials; however, the mechanical behavior of these solids is not well understood to date. Layered solids have been studied in various fields such as geology, engineering, and physics for sometime, but have been explored mostly individually and not studied as a group. Thus, the effort to understand their mechanical behavior has been diluted due to studies in isolation. One of the intriguing characteristics of theses solids, of particular interest to this study, is that their stress-strain response exhibits a fully reversible, non linear hysteretic response. This is an attempt to study these solids as a whole, at high stresses, to see if a common mechanism exists that can explain their mechanical response. To that effect, a brief background is given for three well studied solids in this class of materials – graphite, mica and the MAX phases.

1.1.1 Graphite – a century old mystery

Graphite is an allotrope of carbon distinguished by its lubricious properties that can be traced to the nature of its bonding. Graphite is non-toxic and chemically inert to acids and alkalis under most conditions. Its layered nature makes it one of the best and most

cost effective solid lubricants, particularly for sliding contact applications under adverse temperatures and pressures. However, under vacuum, its lubricative properties are degraded considerably – its lubricative properties being attributed to the presence of moisture between the sliding surfaces. Graphite is stable up to 3200°C under vacuum or inert/protective atmospheres, though it gets oxidized in air or oxygen around 400°C. This property has resulted in its extensive use for crucibles, refractories and products where continuous contact with liquid metals is required.

The heat resistance of graphite is utilized in rocket nozzles, space shuttle heat shields, hot pressing and hot extrusion dies and nuclear power plants. Due it its lubricity, heat resistance, thermal and electrical conductivity, graphite is used as heating element electrodes and brushes for motors. Structurally, graphite is well known for its use as graphite fibers in composites, where its very high stiffness to weight ratio is remarkable. Its strength at high temperatures (40MPa at 1600°C) has made graphite the default material of choice for hot pressing and extrusion dies. Though not applied exhaustively, graphite has very good damping properties.

The normal structure of graphite is hexagonal, with c = 6.708 Å and a = 2.456 Å, with a c/a ratio is 2.73. Rhombohedral phases also have been observed when graphite is subjected to deformation processes such as grinding and/or powdering [1]. The focus of this study is on the hexagonal phase which is more prevalent and thus all references contained herein are to the hexagonal phase. The crystal structure of graphite is shown in Fig. 1. Dislocations have been observed in graphite, mostly along the basal planes. Like Ti_3SiC_2, basal slip is observed in graphite, with a maximum critical resolved shear stress of 0.3 MPa.

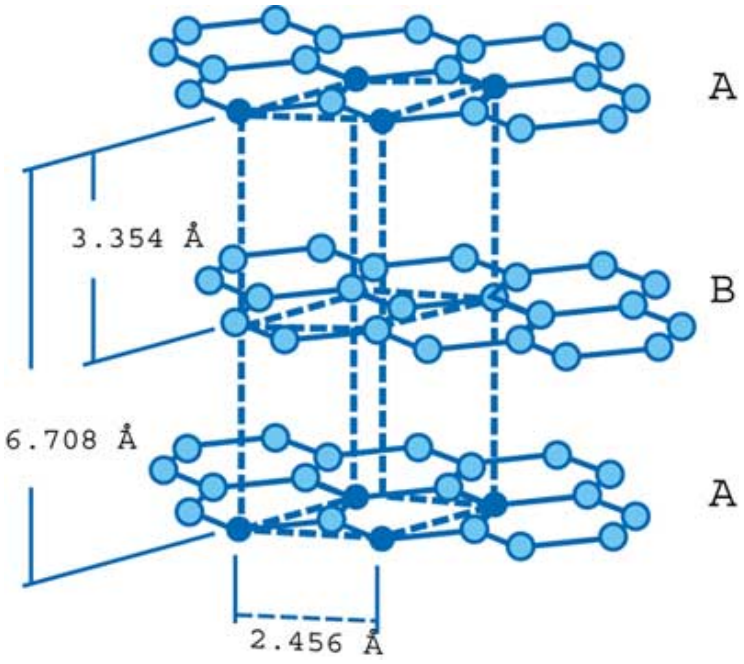

Figure 1: Layered crystal structure of graphite

Apart from point defects, other defects found are tilt and twist boundaries. The basal plane dislocations appear in pairs of partial dislocations: the total dislocation is $1/3a\langle 11\bar{2}0\rangle$ given by

$$1/3a\langle 10\bar{1}0\rangle + 1/3a\langle 1\bar{1}00\rangle = 1/3a\langle 2\bar{1}\bar{1}0\rangle$$

Non-basal dislocations have been observed, particularly in irradiated graphites with a Burger's vector of c/2[0001]. These dislocations are formed as loops, enclosing a stacking fault. However, forming non-basal dislocations are not favored due to the high energies required for their formation. Observation of twins has been reported and different models have been proposed to explain the formation of twins [1]. However, it is

not clear how twins can form despite its high c/a ratio. As shown later, these twins could very well be kink bands.

Graphite has one of the highest elastic anisotropies observed, with a basal plane stiffness (perpendicular to the c-axis) c_{11} = 1060 GPa and (parallel to the c axis) c_{33} = 36.5 GPa. The mechanical anisotropy of graphite in elasticity, plasticity and fracture stems from the very strong covalent bonds between the nearest neighbors in the basal planes and the weak Van der Waal's forces between the layers. The elastic constants of c_{33} and c_{44} are determined by the weaker Van der Waal's forces and conversely the values c_{11} and c_{12} are determined by the strong covalent bonds. c_{13} involves both bonds. The elastic constants are listed in Table 1 [1]. The glissile dislocations in the basal planes reduce the measured value of c_{44}, particularly in perfect crystals. However, in crystals were there is a high concentration of lattice defects, such as in irradiated crystals, the dislocations are not very mobile and thus the values measured in such graphites are closer to that obtained from specific heat data and *ab-initio* calculations.

Studies done on the mechanical response of graphite have shown the stress strain behavior to have hysteresis loops on repeated loadings and thereby indicate significant damping (Fig. 2). It was observed that when the applied stresses and strains are within one order of magnitude lower than the failure stress, the energy loss (the ratio of the area inside the curve to the total area under the curve) increased with strain, and energy losses of the order of 0.1 were realized (the damping measurements were done at ~ 1 Hz) [1]. The deformation and damping in graphite is strongly influenced by the basal plane dislocations. It has been observed that irradiating polycrystalline graphite reduced damping – indicating the effect of glissile basal plane dislocations and plastic flow on

damping. Studies done on internal friction of graphite using torsion pendulums (frequency ~ 1 Hz) also showed similar behavior: the more perfect the crystal, the higher the damping and internal friction.

Table 1: Stiffness values of graphite [1]

Stiffness	Value (GPa)
C11	1060+-20
C12	180+-20
C13	15+-5
C33	36.5+-1
C44	0.18 -0.35

The best supported explanation given so far is that the loss mechanisms associated with crystalline shear processes were responsible for the losses observed. The reasons for the damping and loss could be due to:

1. basal plane dislocations (shear) as mentioned above
2. cyclic propagation of basal cracks

Cyclic propagation of basal cracks can be ruled out as repeated cycling would result in weakening of the sample and thus reduce the value of the modulus which is not observed. A few models have been proposed to explain the hysteresis behavior based on

the basal plane dislocations. One of the more detailed models was presented by Granato and Lucke [as cited in Ref. 1].

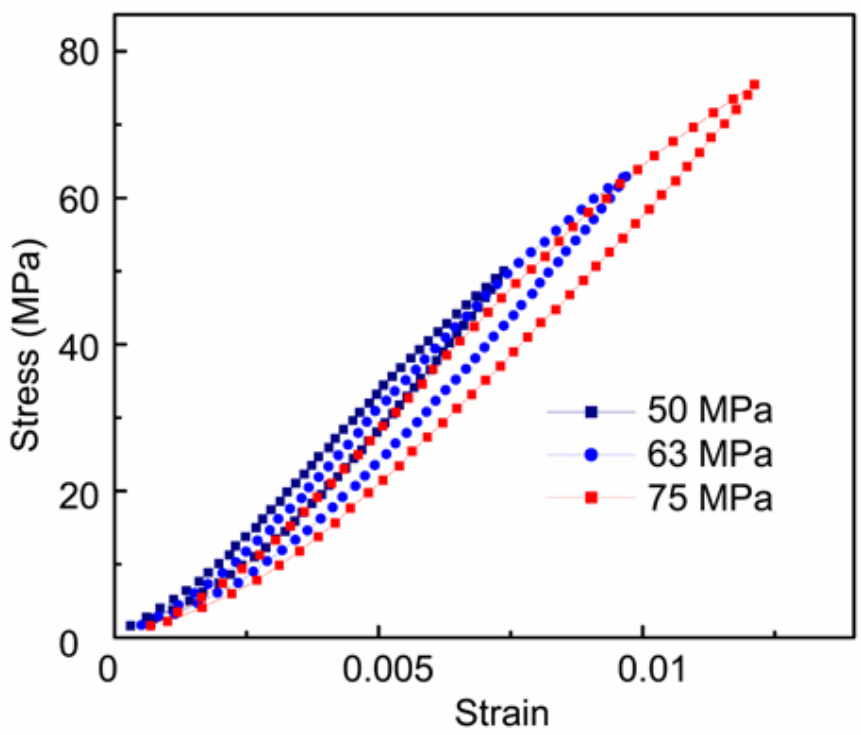

Figure 2: Hysteresis observed in bulk polycrystalline graphite in simple compression

According to this model, the dislocations are pinned at various points along their length, probably by impurities. As the stress is applied, the arcs of dislocation between the pinned points bow out, and could eventually break away from the pinning points at higher stresses, "unzipping" from the pinning points. These dislocations then have longer arcs where they could be pinned by stronger pinning sources. The converse would be true during unloading, where the dislocations zip back, resulting in a hysteretic behavior. The varying pinning point strengths and dislocation lengths in the material would give

different hysteresis loop shapes for different grades of graphites – for example pure and near perfect crystals would have very large loop areas and neutron irradiated graphite with very high dislocation densities would have smaller loop areas.

Recently, reversible hysteresis in nanoindentation curves on glassy carbon materials were explained in terms of the *reversible* slip of graphene planes in nanometer grains [2] and the hysteresis was attributed to sliding friction between the layers due to the compressive stresses [3,4]. More recently, it has been suggested that dislocation pileups may be responsible [2]. However, the exact mechanism of the hysteretic stress strain behavior is not well understood to date.

1.1.2 Deformation in Mica and understanding in geology

Micas and other silicates are layered. The deformations of rocks, and mica in particular, have been studied for quite some time. The structure of mica is shown in Fig. 3. Mica belongs to a family of layered compounds that are formed by sheets of negatively charged silicate layers bonded together by interlayer cations [5] such as sodium or potassium (in the case of muscovite micas). The interlayer bonding is weak compared to the in-plane bonds of the silicate sheets, and thus these micaceous solids can be easily delaminated along their basal planes.

For the purpose of our study, muscovite mica ($KAl_2(AlSi_3)O_{10}(OH)_2$) was chosen due to its availability in pure and high quality single crystals. The mechanical properties of these compounds are strongly influenced by their anisotropy in bonding - strong intraplanar bonding and the much weaker interplanar forces, similar to other layered

materials such as graphite, oxide superconductors and plastic anisotropy as in the case of the MAX phases.

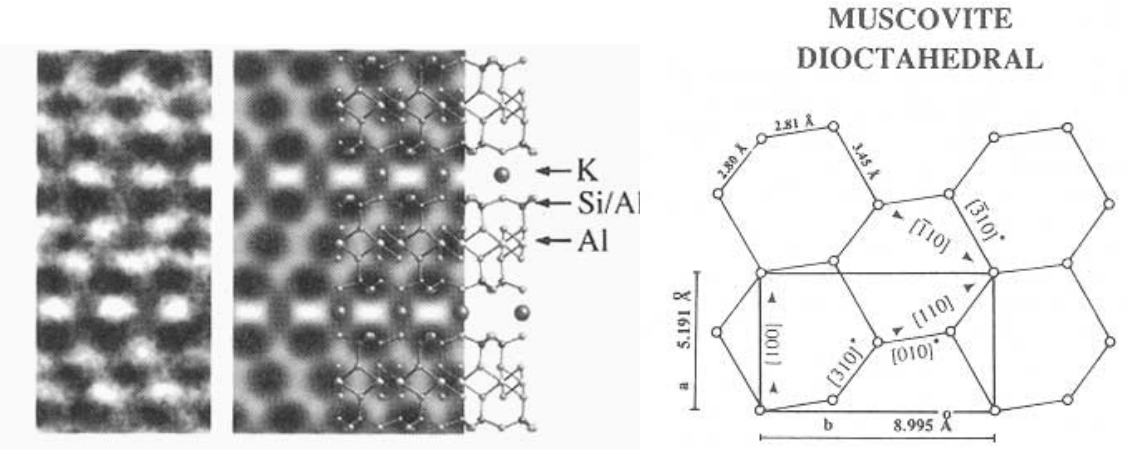

Figure 3: Structure of Mica (Muscovite)

These solids are also characterized by a high c/a ratio > 2 [5], and deformation of mica usually occurs by shear along the basal planes, implying basal plane dislocations are active and responsible for some deformation. Dislocations have been observed in the basal planes as partial dislocations [6] as shown in Fig. 4 such as:

$$(1/2)[\bar{1}10] \rightarrow (1/6)[\bar{3}10] + (1/3)[010],$$

$$(1/2)[110] \rightarrow (1/6)[310] + (1/3)[010],$$

$$\text{and } [100] \rightarrow (1/6)[3\bar{1}0] + (1/6)[310].$$

Parallel dislocation arrays and dislocation networks have also been observed in *in-situ* TEM [6]. Cross slip and screw dislocations are very unlikely due to energy considerations associated with cross-slip of dislocations across tetrahedrally coordinated Si layers [6].

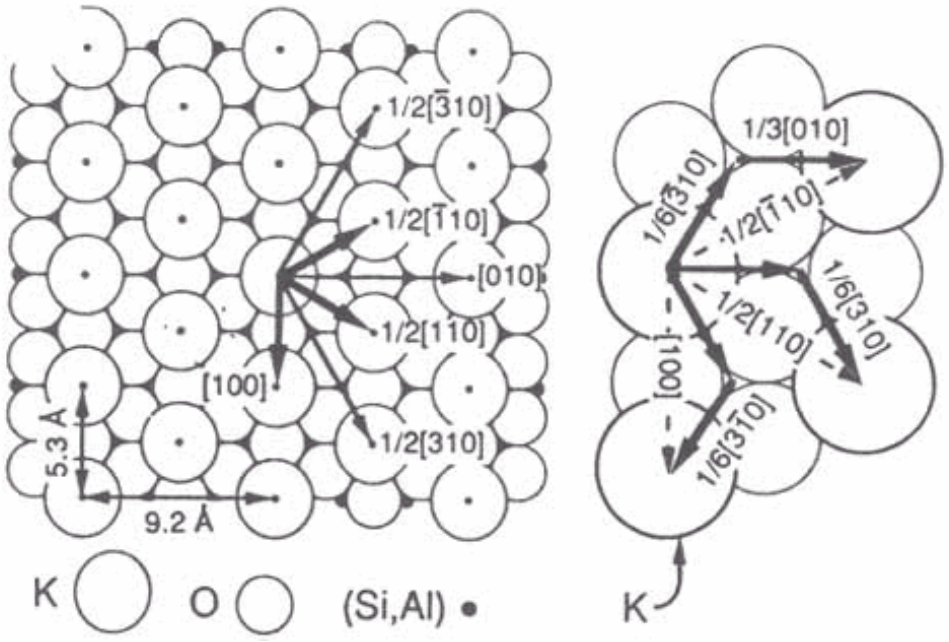

Figure 4: Possible dislocations and dislocation partials in mica

Kinking is the most favored mode of deformation mechanisms in rocks and micaceous solids [7]. Kink bands have been observed in micas, of the order of a few micrometers in the crystals. In geology, folding is the most prominent structural feature observed due to the natural deformation of layered or foliated rocks – these folds are thought to form due to shear slip along the basal planes on sets of surfaces parallel to the foliation. Such processes could occur under highly constrained stress conditions and/or high temperatures while such rocks are formed (as in the case of igneous rocks).

The hysteretic nature these materials have been studied (Fig. 5), though only with phenomenological models, namely the Preisach-Mayergoyz space (P-M space) model. These solids have been termed “nonlinear mesoscopic elastic solids” or NMES – a term used to describe their nonlinear hysteretic behavior and the fact that the size of the

attendant crystals responsible for such behavior is in the mesoscopic scale – i.e., of the order of 1 μm.

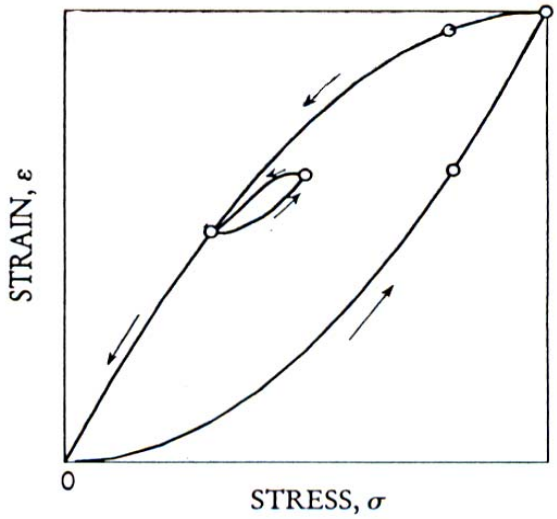

Figure 5: Schematic of stress strain response observed in rocks and mica in simple compression.

A brief description of the P-M space model is summarized below:

The rocks are assumed to consist of very hard particles or grains (of the order of 1 μm – hence mesoscopic) and a bond system between the grains. (A good example is sandstone where the aggregate of grains composed of a single or a group of minerals are fused together at high pressures and temperatures during their formation). This rock-bond system is represented as an assemblage of rudimentary hysteretic elastic elements or hysteretic mesoscopic units (HMU) [Fig. 6]. These elements can be in either one of two states – open or closed. As the applied stress is increased, the element, originally open with length L_o, closes to length L_c after a certain stress σ_c and remains closed as the stress is further increased.

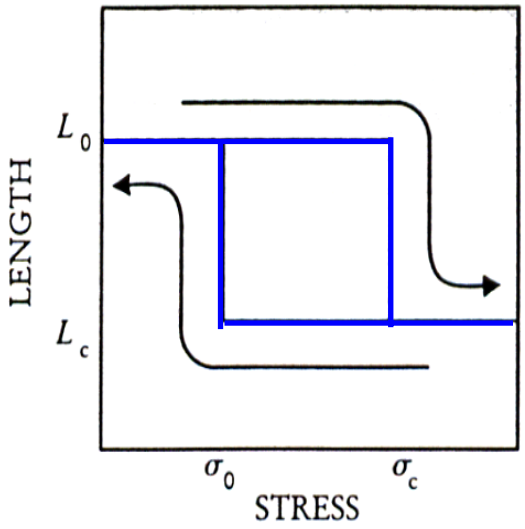

Figure 6: Rudimentary element of the hysteretic mesoscopic units (HMUs).

On the other hand, while the stress is decreased, the element remains closed even after the stress is decreased below $\sigma_{c;}$ in other words, the process is non-linear. On unloading, once the stress is below certain stress σ_o, the element comes back to its original length L_o and remains in this state as the stress is decreased further. A large number of such HMUs with different critical stresses σ_c and σ_o, and lengths L_c and L_o are used to model the rock's bond system. This model has some drawbacks in that it takes into account only the macroscopic bond system and ignores the deformation mechanism of the crystal itself (the implicit assumption is that the deformation of the crystal is elastic). Moreover, the actual physical mechanism of the HMUs are not understood. In this study we show that HMUs are nothing but IKBs.

1.1.3 Deformation in MAX phases

The carbide Ti_3SiC_2 is a hexagonal layered compound belonging to a family of over 50 ternary carbides and nitrides with the general formula $M_{n+1}AX_n$, where n = 1 to 3, M is an early transition metal, A is an A-group (mostly IIIA and IVA) element and X is C and/or N [8]. These phases are composed of $M_{n+1}X_n$ layers interleaved with layers of A-group elements. There are 3 distinct families of these materials, namely the M_2AX or 211s (about 50 such compounds), M_3AX_2 or 312s – Ti_3SiC_2, Ti_3GeC_2, and Ti_3AlC_2 and M_4AX_3 or 413s - Ti_3AlN_4. Recently a metastable Ti_3SiC_4 grown by thin film deposition was reported [9]. The unit cells of these compounds are shown in Fig. 7.

These compounds - best described as thermodynamically stable nanolaminates - possess an unusual combination of properties [8]. The most studied, and best understood, to date is Ti_3SiC_2. It has the same density as Ti, but is almost three times as stiff and yet readily machinable [8,10,11]. It is a better electrical and thermal conductor than Ti metal [11]; highly resistant to damage [12,13], thermal shock [11,12], fatigue [14] and creep [15]. It exhibits an increasing R-curve behavior [14], with fracture toughness values as high as $16MPa.\sqrt{m}$

Oriented coarse-grained (1–3 mm) polycrystalline samples of Ti_3SiC_2 loaded in compression at room temperature can be deformed plastically even at room temperature. Substantial (>20%) deformation is realized when the basal planes were oriented favorably to the applied stress. The deformation mechanism responsible for this behavior is attributed to the formation of shear bands along those planes, implying that the main deformation mechanism was basal slip.

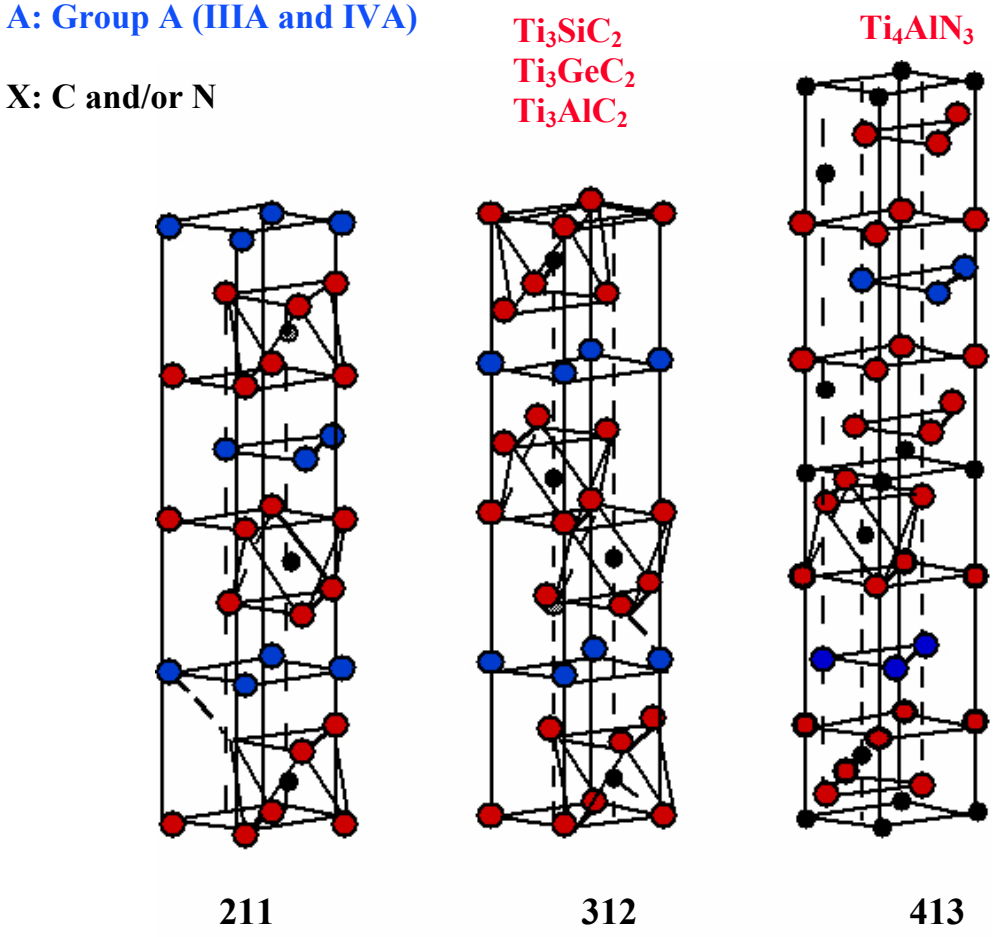

Figure 7: Crystal structure of the MAX phases

When the samples were oriented such that slip planes (the basal planes) were parallel to the applied load, plastic deformation was realized even though ordinary glide is not possible at this orientation. The deformation occurred by a combination of delamination of individual grains (buckling of the grains), and the formation of kink and shear bands.

It is now fairly well established that the Vickers microhardness values in Ti_3SiC_2 decrease with increasing loads down to a plateau value [10,11,13,16-18]. Furthermore, it is not possible to induce cracking from the corners of Vickers indentations even at loads

of 500 N [10,11,13]. Diffuse microcracking, delamination, crack deflection, grain push-out, grain pull-out and the buckling of individual grains have all been identified as energy absorbing mechanisms [13]. Of special interest to this work is the work of Low et al. [16], who showed that Hertzian indentation stress–strain response deviated strongly from linearity beyond a well-defined maximum, with pronounced strain–softening, indicating exceptional deformability in this otherwise stiff ceramic. Surface and subsurface ceramographic observations revealed extensive quasi-plastic microdamage zones at the contact sites. These damage zones were made up of multiple intragrain slip and intergrain shear failures, with attendant microfracture at high strains. No ring cracks or other macroscopic cracks are observed on, or below, the indented surfaces.

The unique characteristics of the mechanical response of Ti_3SiC_2 described above are directly attributable to the following facts:

i) Basal slip, and only basal slip, is operative [18-21], dislocations multiply and are mobile at room temperature.

ii) Because of their high c/a ratios, twinning is unlikely, and has never been reported. Instead, deformation occurs by a combination of glide and kink band formation within individual grains [18-21].

iii) Because they are confined to the basal planes, dislocations arrange themselves either in arrays (pileups) on the same slip plane, or in walls (tilt boundaries) normal to the arrays [19,20] The arrays are composed of perfect basal- dislocations with a Burgers vector of 1/3 <11-2 0>. A key characteristic of the Ti_3SiC_2 structure, which is important in understanding the atomistics of its mechanical properties, is that the basal interatomic vector is the shortest full translation vector in this structure. Thus, non-basal dislocations

are very unlikely, and none have been reported [19,20]. Dislocation interactions, other than orthogonal, are difficult and unlikely to occur, which allows the dislocations to move back and forth reversibly and extensively.

Most recently we have shown that macroscopic polycrystalline Ti_3SiC_2 cylinders can be compressed, at room temperature, to stresses of up to 1 GPa, and fully recover upon the removal of the load, while dissipating ≈ 25% of the mechanical energy [22]. The stress-strain curves at room temperature outline fully reversible, reproducible, rate-independent, closed hysteresis loops (Fig. 8) that are strongly influenced by grain size with the energy dissipated being significantly larger in the coarse-grained material. The loss factors for Ti_3SiC_2 are higher than most woods and comparable to polypropylene and nylon. Furthermore, the energy dissipated per cycle, W_d, was found to scale with the square of the applied stress, σ. In one case, a sample was cycled 100 times to 700 MPa, with no apparent changes in the shape or size of the loops.

This can have significant applications in vibration damping in MEMS. When taken together with the fact that the friction coefficients of the basal planes are extremely low [23], the possibility of having high wear resistant surfaces that are very low friction is a tantalizing prospect. Furthermore, the prospect of exploring the more than 50 $M_{n+1}AX_n$ phases known to exist [8], and innumerable combinations of solid solutions, is a wonderful one indeed, and one that should prove to be of technological and scientific importance and benefit.

As this work will show, the deformation mechanism for all the above layered solids, even under very high stresses, can be attributed to the formation and annihilation of fully reversible incipient kink bands, or IKBs.

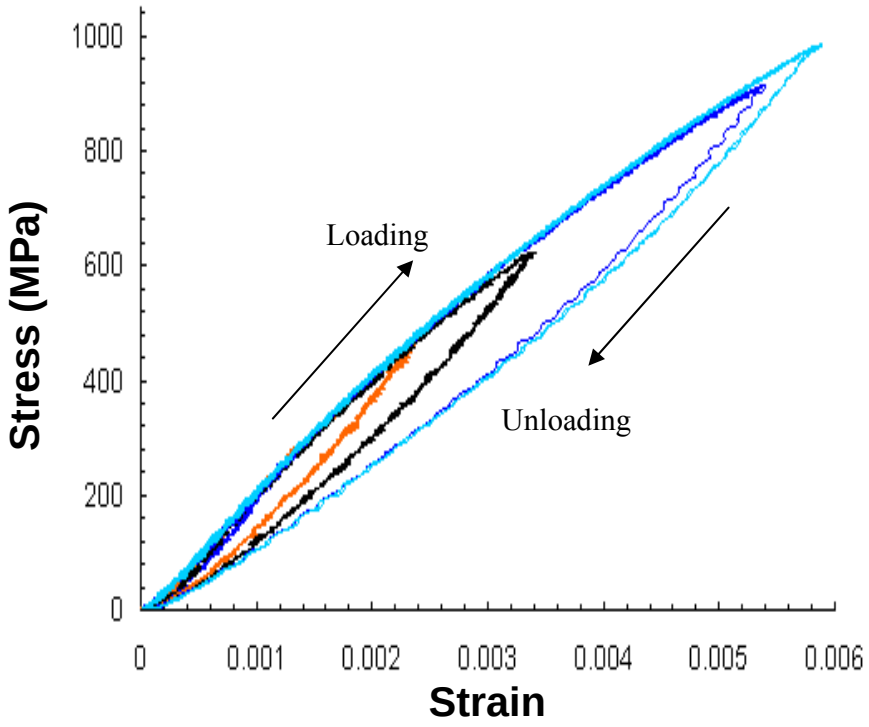

Figure 8: Hysteretic behavior observed in simple compression tests of Ti_3SiC_2 up to 1 GPa.

IKBs are comprised of near parallel dislocation walls of opposite polarity that remain attached, and are thus attracted to each other. Removal of the load allows the walls to collapse and the IKB to be totally eliminated. At high temperatures (higher than 1000 °C) or stresses, the stress-strain loops are open and the response becomes strain rate dependent. At high stresses or temperatures, the IKBs devolve to mobile walls and eventually to permanent kink bands.

1.2 Motivation

Though the mechanical properties of these materials – mica, rocks and related materials in geology, and graphite in particular, have been studied for over a century [1], the physical mechanisms behind such behavior is not well understood to date. This is surprising since the impact of these materials on our lives, though not well appreciated, are enormous – from understanding earth quakes, building quake proof structures, and in various engineering applications. In the case of the $M_{n+1}AX_n$ phases - with more than 50 known to exist, and innumerable combinations of solid solutions - the absorption of energy during loading-unloading cycles could also in principle render them excellent surfaces for applications where vibration damping is desired; an important consideration for many Micro-Electro-Mechanical Systems (MEMS) and other critical applications. The motivation for this work is to understand the physical underpinnings of the mechanical response of this group of solids so as to harness these materials to their fullest potential.

1.3 Research Goals and Objectives

The ultimate goal of this study is to explain the mechanism for the hysteresis behavior of the KNE solids at the crystal level. To this end, this work is divided to include studying these materials at very high stresses in contact loadings – using nanoindentations and studying the deformation and damage evolution, particularly in Ti_3SiC_2, at different orientations with the help of orientation imaging microscopy (OIM). For this purpose, new processing routes were evolved to synthesize very large grained samples of particular orientations (preferably single crystals). Another portion of this

project is to compare and relate their behavior with compression tests in order to determine if their properties can be extrapolated to high stresses (i.e., to predict their high stress response reliably), and to investigate if these layered solids have similar underlying mechanisms despite their differences in the nature of bonding, and thus to find the elusive mechanism responsible for their mechanical behavior of these solids that have been a mystery for over a century.

CHAPTER 2: NANOINDENTATION THEORY AND EXPERIMENTAL METHODS

2.1 Introduction

Nanoindentation also known as depth sensing indentation is a relatively recent technique that has been used to probe very small volumes to extract properties such as hardness, elastic moduli, yield points in some cases [24,25], in the study of phase transformations [26] and mechanical response of materials in general.

Nanoindentation involves depressing a sharp pointed or a spherical indenter on the sample surface, while monitoring the displacements and the forces accurately during loading and unloading. From the load displacement curves the aforementioned properties can be extracted with application of appropriate theories as discussed below. The modulus and hardness are usually extracted during the initial portions of the unloading curves, however, in the case of spherical indenters, modulus values can also be extracted from the initial portions of the loading curve (details are given below).

A brief description of some of the common types of indenters that are used in nanoindentation:

1. 3 sided pyramid – Berkovich indenter whose area-to-depth function is the same as that of a Vickers indenter
2. Cube corner – 3 sided like the corner of a cube. It is sharper than a Berkovich, and produces much higher stresses and strains in the vicinity of the indent than a Berkovich indenter.

3. Vikers – a 4 sided pyramid – one draw back is that it is very difficult to grind the indenter to a point – terminating in a chisel edge. This causes its small scale geometry to differ from that at larger scales.
4. Conical indenters – Like a Berkovich, has a self similar geometry. Its simple cylindrical symmetry makes it attractive from a modeling standpoint. It also does not have the stress concentrations associated with the sharp edges of the pyramid indenters.
5. Spherical indenters.

In this study, a spherical diamond indenter of 13.5 micron radius was used almost exclusively for the experiments. A 3 sided pyramid – Berkovich diamond indenter was also used for comparison. Other geometries of indenters were not used in this work.

An attractive feature of spherical tipped indenters is that the initial response to loading is elastic, unlike sharp pointed indenters such as the Berkovich and the cube corner indenters, which result in damage and/or plastic deformation even at low loads. The stress fields generated by a spherical indenter can also be calculated analytically and do not exhibit the stress singularities inherent in perfectly sharp pointed or flat (cylindrical) indenters. After a critical load or contact pressure, there is a transition from elasticity to plasticity/damage, where the interpretation of force displacement behavior becomes more complex. [25]

One important feature to this work with spherical indenters is that there is a changing contact strain with change in contact stress (unlike sharp indenters which are self similar – i.e., the rate of change of area with displacement is constant), thus the indentation stress

vs. strain curves can be plotted. This also enables characterization of strain hardening/softening of a material [25].

2.2 Nanoindentation Stress and Strain

The theory for extracting properties using spherical indenters, such as the hardness values and modulus date back originally to the analytical solutions proposed by Hertz, who assumed of paraboloids in elastic contact. However, later on it was shown by Mayer, Tabor [27] and Johnson [28] that similarities existed between pointed and spherical tipped indenters and thus the theory can be applied to sharp indenters as well [29].

In this study, the interest was to extract elastic modulus and the stress strain curves. There are two popular theories to extract the modulus and hardness values, one was given by Oliver and Pharr [30] and other by Field and Swain [24]. For our studies, the interest was in the stress strain curves and extracting the modulus from these curves, thus the complete theories by Oliver and Pharr and Field and Swain are not given here. Instead, the theory of extracting stress and strain is briefly given [3,4,27-29,31,32]. For an elastic contact, the load to the depth of contact h_e for a sphere of radius R on a flat surface was given by Hertz [28] as:

$$h_e = \left(\frac{3P}{4E^*}\right)^{2/3}\left(\frac{1}{R}\right)^{1/3} \qquad \text{----------(1)}$$

where h_e is the penetration depth of the indenter relative to the original surface. E* is the reduced modulus, which includes properties of both the indenter and the sample, given by:

$$\frac{1}{E^*} = \frac{1-\nu_s^2}{E_s} + \frac{1-\nu_i^2}{E_i} \qquad \text{----------(2)}$$

where ν is Poisson's ratio, and the subscripts *s* and *i* refer to the specimen and the indenter, respectively.

Geometrically, the actual contact diameter 2a is related to h_c (Fig. 1) by [29]:

$$a = \sqrt{2Rh_c - h_c^{\,2}} \approx \sqrt{2Rh_c}\,, \quad h_c << \mathrm{R} \qquad \text{----------(3)}$$

where h_c is the depth at which the indenter and surface are no longer conformal (Fig. 9).

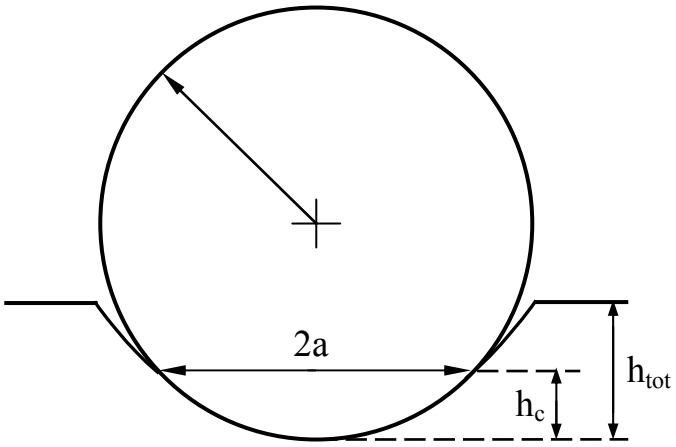

Figure 9: Schematic of indentation with a spherical indenter, showing the actual area of contact, at small indentation depths (hc << R).

Note that Eq. 6 in Ref. 3 and Eq. 4 in Ref. 4 are incorrect; a factor of 2 is missing.

Assuming that in the purely *elastic* regime [4,28,29]:

$$h_c \approx h_e/2 \qquad \text{----------(4)}$$

implies

$$h_e = a^2/R. \qquad \text{----------(5)}$$

Note this equation implies that in the elastic regime $(a/R) = h_e/a$.

Using Eq. 5 to eliminate h_e from Eq. 1 yields the sought after result:

$$\frac{P}{\pi a^2} = \frac{4}{3\pi} E * (\frac{a}{R}) \qquad \text{----------(6)}$$

The values of $\nu = 0.07$ and $E = 1170$ GPa were used for the diamond indenter. Control experiments carried out on silica (up to 200 mN) yielded stress-strain curves that were linear, fully reversible and exhibited <u>no</u> hysteresis. The modulus measurements from the control experiments were within 5 % of the accepted value for the modulus of fused SiO_2; viz. 70 GPa [30].

Beyond the "yield point", the deformation is elasto-plastic and h_c in this regime is usually assumed to be [4]:

$$h_c = h_{tot} - h_e/2 \qquad \text{----------(7)}$$

where h_{tot} is the measured total penetration (elasto-plastic) from experiment and h_e is computed from Eq. 1 assuming a purely elastic contact.

In the case of experiments with layered solids, fully reversible hysteretic response was observed at low loads. At higher loads the first indents usually resulted in permanent deformation as shown in the schematic (Fig. 10a), however, the subsequent indentations

were hysteretic and fully reversible. One such load displacement curve for Ti_3SiC_2 is plotted in Fig. 10b.

During each indent, the nanoindenter reinitializes the point of contact with surface as the zero reference point (zero displacement). If multiple indentations are done in the same location, there is a correction that has to be made if the first indent leaves a permanent residual strain. If the first indent makes a small crater, the zero displacement for the second is taken when the indenter touches the surface of the crater. In other words, the displacements recorded for all the curves start at the same zero.

The residual displacement of the first indent has to be taken into account on subsequent indents. This is done by adding the residual permanent strain of the first indent to the subsequent indents as shown in Fig. 10c. In other words, all the unloading curves on the second and subsequent loadings were forced to coincide. This recalibration not only accounts for the residual impressions left after the first indent but also eliminates much of the uncertainty as to the exact point at which the indenter touches the surface on reloading.

This procedure leads to more consistent results, and eliminates the problem of having the maximum calculated stresses upon re-loading being higher than the maximal stresses reached during the first loading (Fig. 10d). The corresponding corrected stress strain curves are shown in Fig. 10e. It is clear that if the correction is not made, the stress of subsequent indents are higher, which is not possible for the same load and same or possibly higher area of contact.

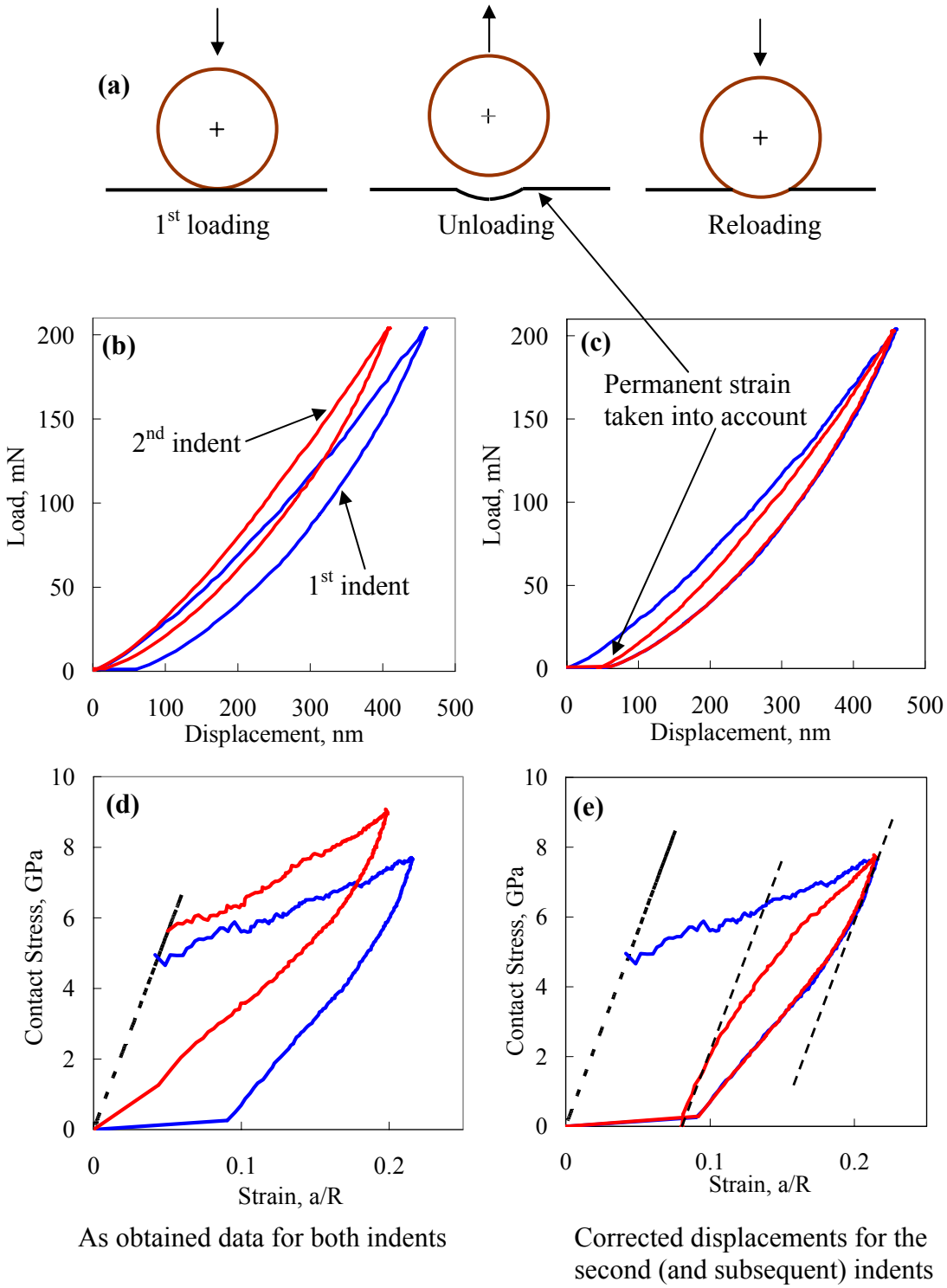

Figure 10: Load-displacement and stress strain curves for as obtained data and with correction. The inclined dashed lines in the stress strain curves correspond to a modulus of 320 GPa.

2.3 Work Done

In this work, the hysteretic energy loss per unit volume, W_d, was determined from the computed indentation stress-strain curves. The effective volume over which the hysteretic energy loss is dissipated under the indenter can be estimated by dividing hysteretic energy loss computed directly from the load-displacement curves by W_d. The energy may be assumed to be dissipated in a cylinder of radius a and depth h_{eff} under the indenter. For the data presented in this study, h_{eff} was found to be around $1.5a$. This value is quite reasonable and validates the computation of W_d from the stress-strain curves.

In this study, the W_d determined from the indentation stress-strain curves is compared with simple compression stress strain curves. The stress state is uniform in the sample in the case of simple compression, while in the case of nanoindentations the stress state is more complex. Thus to give a comparison between the two, an analysis of the areas under pure elastic stress strain curves (elastic energy) for both simple compression and nanoindentation are given below.

For compression tests, the area under the elastic curve is given by:

$$Area = \frac{1}{2}\sigma\varepsilon = \frac{1}{2}\sigma^2 E \qquad \text{----------(8)}$$

For a pure elastic case in nanoindentations, the area under the stress strain is derived as follows:

$$Area = \frac{1}{2}\sigma\varepsilon = \frac{1}{2}\left(\frac{P}{\pi a^2}\right)\left(\frac{a}{R}\right) = \frac{1}{2}\left(\frac{P}{\pi aR}\right)$$

$$= \frac{1}{2}\left(\frac{P}{\pi R\sqrt{2Rh_c}}\right) = \frac{1}{2}\left(\frac{P}{\pi R\sqrt{2Rh_e/2}}\right) = \frac{1}{2}\left(\frac{P}{\pi R\sqrt{Rh_e}}\right) \qquad \text{----------(9)}$$

where h_e is given by Eq. 1

Substitution for h_e in Eq. 9 and on simplifying:

$$Area = \frac{1}{2\pi}\left(\frac{4P^2E^*}{3R^4}\right)^{1/3} \qquad \text{----------(10)}$$

Expressing the load P in terms of σ

$$\sigma = \frac{P}{\pi a^2} = \frac{P}{\pi\left(2Rh_e/2\right)} = \frac{P}{\pi Rh_e}$$

Substituting for h_e,

$$\sigma = \frac{1}{\pi}P^{1/3}\left(\frac{4E^*}{3R}\right)^{2/3} \qquad \text{----------(11)}$$

Or

$$P = \left(\pi\sigma\right)^3\left(\frac{4E^*}{3R}\right)^{-2} \qquad \text{----------(12)}$$

Substituting in Eq. 10, we get:

$$Area = \frac{3\pi}{8}\left(\frac{\sigma^2}{E^*}\right) \qquad \text{----------(13)}$$

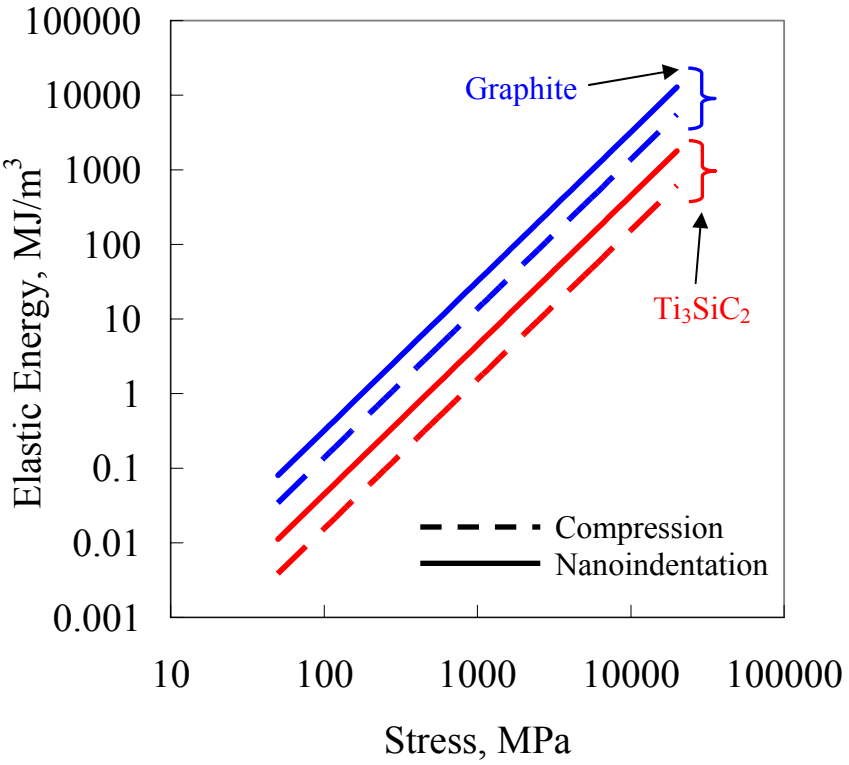

Figure 11: Comparison of area under elastic stress strain curves for simple compression and nanoindentations for Ti_3SiC_2 and graphite. A modulus value of 325 GPa was used for Ti_3SiC_2 and 36.5 GPa for graphite.

Consequently, the area is a function of the applied stress and the moduli, Poisson's ratios of both sample and the indenter. Sample areas under the curves are plotted for Ti_3SiC_2 and graphite for compression and nanoindentation in Fig. 11 for comparison. The area under the elastic stress strain curve for nanoindentation is higher than for case of simple compression.

2.4 Nanoindentation Testing Parameters

Load cycle indentations were carried out using a nanoindenter (Nanoindenter® XP, MTS Systems Corporation, Oak Ridge, TN). The experiments were carried out under

load control up to maximal loads of 10, 50, 100, 200 and 500 mN, held there for 15 s, and unloaded. To discount any experimental artifacts, similar tests were carried out in fused silica and sapphire at the above loads for comparison. To study the effect of cycling, typically multiple (mostly 5) indentations were carried out at the same location to any given load.

The samples were tested at loading rates varying anywhere between 0.3 mN/sec to 10 mN/sec depending upon the sample and the maximal loads. The loading rates are listed for the respective samples in each chapter. In most cases, the first indents usually resulted in permanent residual displacements. To account for this permanent displacement in the subsequent indents, all the unloading curves on the second and subsequent loadings were forced to coincide as explained earlier.

Furthermore, in most of the repeat cycles a small (≈ 10 nm) residual deformation was recorded. By careful calibration with silica - which behaves elastically – and with atomic force microscopy (AFM) on repeated indents, we confirmed that these residual values were an artifact of the measurement and were thus ignored when plotting the second and subsequent cycles. In other words, it was assumed that the second, and subsequent loops were fully reversible.

2.5 Sample Description, Processing and Preparation

Sample preparations for the nanoindentation tests are discussed below individually for Ti_3SiC_2, graphite, mica and YBCO. In the case of Ti_3SiC_2, new processing methods such as tape casting and sintering of Ti_3SiC_2 powders were tried in order to obtain very large single crystals. However, due to problems with high TiC content and/or numerous

processing steps involved, the samples made by these methods were not used for testing. Instead, samples with large oriented grains made by hot pressing (sinter forging) were used. The different processing routes in this work to obtain large single crystals of Ti_3SiC_2 are described in Appendix A.

2.5.1 Hot Pressing of Ti_3SiC_2

The samples were made using sinter forging technique [18]. In brief: Ti, SiC and graphite powders were mixed, milled, cold pressed and sintered in Ar at 1450°C for 8 hours. The sintered porous billets were hot pressed under plane strain conditions in a graphite die at 1600°C under an axial stress of 42 MPa for 24 hours. The resulting sample had large plate like grains with diameters of 1 to 2 mm and thicknesses of the order of 200 microns. The samples were cut with a diamond saw, mounted and polished with a 0.06 μm colloidal silica suspension, and lastly etched and polished one more time to relieve any surface mechanical damage accumulated during polishing.

The orientations of the grains were confirmed using OIM (orientation imaging microscopy). OIM is a relatively new technique using electron back scattered diffraction to determine the crystallographic structure of polycrystalline specimens, such as crystallographic texture and orientation of individual grains with respect to the sample surface [33-35]. Using OIM, various grains with orientations with c-axis close to 0° and 90° with respect to the indentation direction were selected. More details can be found in Ref. 35.

2.5.2 Graphite

Natural graphite single crystals of ~ 1 to 2 mm in size were cleaved to expose defect free, atomically flat (0001) planes. At 14 cm^{-1} the full width at half maximum of the Raman G-band from the basal planes was quite narrow which, together with absence of D-bands, was taken as evidence that the graphite single crystal was of high quality. Since the crystal was irregular in shape, care had to be taken to ensure that the sample surfaces were normal to the indenting direction. To do so, the crystals were mounted using a conductive epoxy on a steel ball that was attached to a specially made sample holder (Fig. 12). The surface of the sample was then adjusted to be horizontal by rotating the steel ball to the correct inclination; this was done under an optical microscope. Once the correct inclination was obtained, the steel ball was tightened to fix the sample in that orientation.

A graphite block (Grade ISO-63, Toyo Tanso USA, Troutdale, OR) with a particle size of 5 μm, a density of 1.83 Mg/m^3 and a compressive strength of 181 MPa was machined into cylinders 9.7 mm in diameter and 31 mm high. The cylinders were cyclically compressed in load control mode at a loading rate of 420 N/s which corresponds to a nominal strain rate of ~ $8.8x10^{-4}$ s^{-1}. The strain was measured by an MTS axial extensometer (25 mm gauge length) attached to the sample. In order to maintain sample alignment, the minimum stress in all tests was about 1–3 MPa [37]. A field emission scanning electron microscope, FESEM, (JOEL - XL30, FEI) was used for imaging the indented surfaces at magnifications up to 20,000 X.

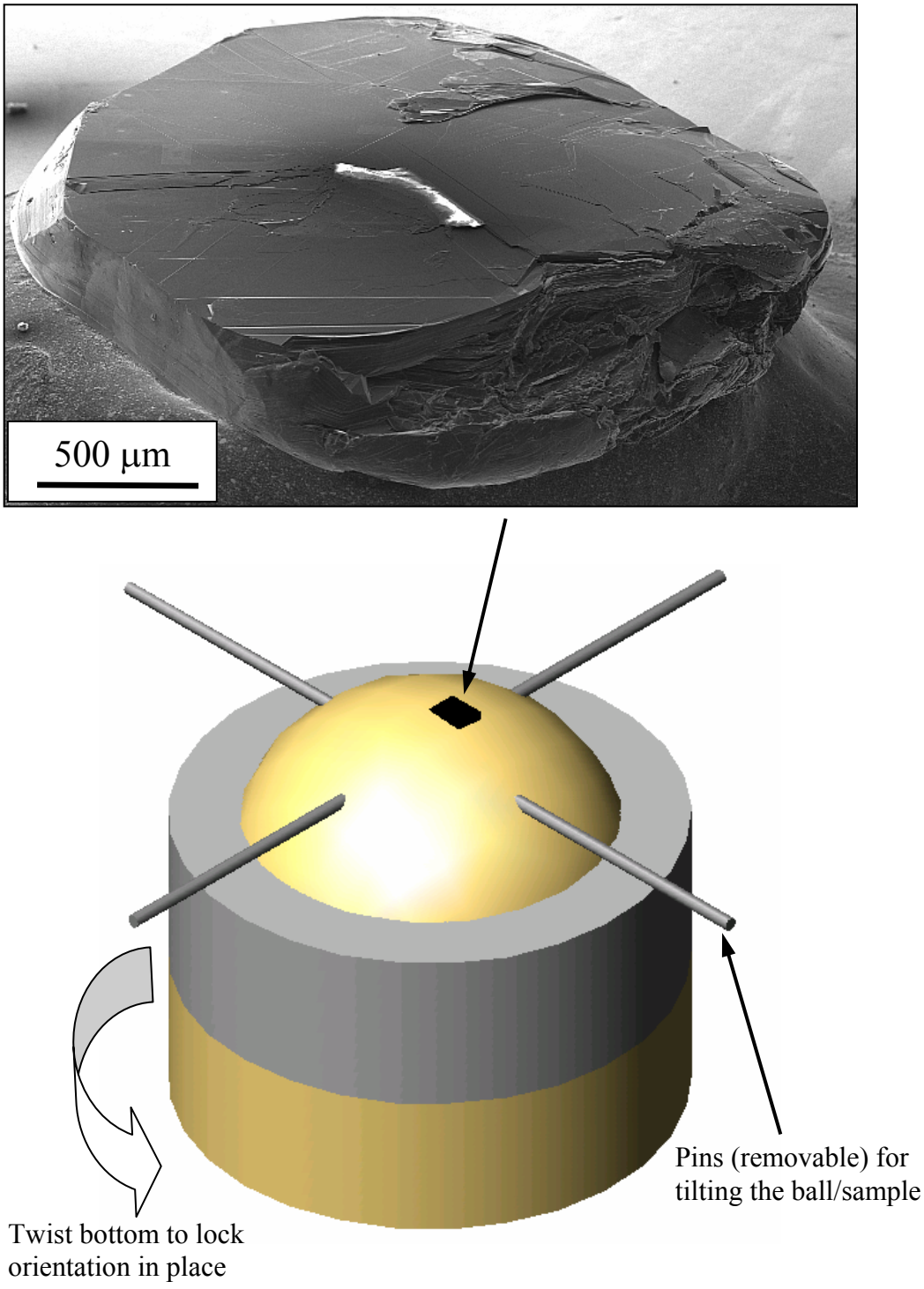

Figure 12: Custom built sample ball holder for mounting the graphite samples that fits in the nanoindenter, FESEM and Raman microspectrometer.

Nanoindents made on pristine surfaces of graphite at various loads, 20 mN, 50 mN, 100 mN and 200 mN were studied using dispersive Raman micro-spectroscopy, (Raman microspectrophotometer Renishaw 1000™) with excitations wavelengths 514.5 nm (Ar+ laser – green) and at 785 nm (diode laser – red), with an automatic XYZ motorized mapping stage for mapping the indented area. The indents were mapped with a 1000X objective, which gives a laser resolution of about 1-2 μm. The step size used for the scans was 0.6 μm along X and Y with 10 s collection time for the Ar+ laser, and 30 s for the diode laser. Based on the absorption coefficients of graphite and the laser wavelengths the depths of penetration of he light into the sample is estimated to be on the order of dozens of nanometers [38].

2.5.3 Mica

Three different natural muscovite single crystals commercially available were studied, the major differences being in their purity and quality of the samples. The grades are classified here as Grade A, B and C (Fig, 13). Grade A is the highest purity grade available and grade B is a slightly lower grade, both A and B grades were obtained from Ted Pella Inc., Redding, CA (commercially available as grades V1 and V2 respectively), with thicknesses of ~ 150 to 200 microns. Grade C mica (Geosource, Ft. Collins, CO) had a higher defect population, evident from their lack of transparency, which is attributed to defects such as air pockets and delaminations in their basal planes. The samples were thick (a few millimeters) and were cleaved to the desired thickness (500 μm to 1 mm), exposing atomically flat surfaces.

Grade A Grade B Grade C

Figure 13: Typical microstructures of different grades of mica used: grades A, B and C

2.5.4 $YBa_2Cu_3O_{6.5}$

The sample used in this study was grown using a Bridgman melt textured technique [39]. This process results in materials comprised of multiple parallel domains having the same orientation with respect to the c axis. The sample also contained ≈ 20 vol. % of Y_2BaCuO_5 phase. The sample was not oxygenated and thus maintained the high temperature tetragonal phase of YBCO. In this phase, twinning has never been observed. The sample was cleaved to expose the basal (001) planes.

The samples were mounted and polished with a 0.06 μm colloidal silica suspension, and lastly etched and polished one more time to relieve any surface mechanical damage accumulated during polishing

CHAPTER 3: SPHERICAL NANOINDENTATIONS AND KINK BANDS IN Ti_3SiC_2

3.1. Introduction

Recently we have shown that macroscopic polycrystalline Ti_3SiC_2 cylinders can be compressed, at room temperature, to stresses of up to 1 GPa, and fully recover upon the removal of the load, while dissipating ≈ 25% of the mechanical energy [22]. The stress-strain curves at room temperature outline fully reversible, reproducible, rate-independent, closed hysteresis loops that are strongly influenced by grain size with the energy dissipated being significantly larger in the coarse-grained material. The loss factors for Ti_3SiC_2 are higher than most woods and comparable to polypropylene and nylon. Furthermore, W_d was found to scale with the square of the applied stress, σ. In one case, a sample was cycled 100 times to 700 MPa, with no apparent changes in the shape or size of the loops. These observations were attributed to the formation and annihilation of fully reversible incipient kink bands, or IKBs. IKBs are comprised of near parallel dislocation walls of opposite polarity that remain attached, and are thus attracted to each other. Removal of the load allows the walls to collapse and the IKB to be totally eliminated. At temperatures higher than 1000 °C, the stress-strain loops are open and the response becomes strain rate dependent. However, cyclic hardening was observed at 1200 °C, for both fine and coarse-grained samples. At higher temperatures the IKBs dissociate into mobile walls that in turn coalesce to form regular kink bands (KBs) that are no longer reversible [22].

The purpose of this work is two fold. First to study the response of Ti_3SiC_2 at high stresses (significantly above the 1 GPa stress imposed in the simple compression tests

[22]) to explore if W_d continues to increase with increasing stresses. For this purpose, we decided to conduct nanoindentation experiments using a spherical nanoindenter, where the stress levels under the indenter of the order of 5-10 GPa. Second, we examined the influence of crystal lattice orientation on the mechanical response and deformation behavior under the indenter.

3.2. Experimental Details

Load cycle indentations were carried out - under load control at loading rates between 0.5 mN/sec and 8 mN/sec – to peak loads of 5, 10, 20, 100, 200 and 500 mN, in two orthogonal orientations: 0° and 90° to the c-axis respectively (i.e. parallel and normal to the c-axis). Two types of tests were carried out: first, regular indentation tests under load control, loaded to the terminal load, held there for 15 s, and unloaded. In the second type, repeated indentations were carried out up to 5 times on the same location to study the effects of cycling. The load-displacement curves were converted into stress-strain as described in chapter 2.

3.3. Results

The response of Ti_3SiC_2 to indentation loadings can be characterized by three regimes: (i) linear elastic, (ii) hysteretic, reversible but without microscopic damage, followed by, at higher stresses, (iii) plastic with damage i.e. microcracking/delaminations. As noted above Ti_3SiC_2 is strongly anisotropic in its plastic properties and therefore in the

following we describe separately the behavior when the grains are indented parallel and normal to the c-axis.

(Note: Where appropriate a schematic of the relationship between the loading direction and the basal planes is shown in the figures for each test as a schematic inset.)

For reasons that are not entirely clear, the stress-strain curves at strains less than ≈ 0.03 were noisy and irreproducible and were omitted. Instead, in that range a straight line was drawn through the origin assuming a modulus [10,11] of 320 GPa. All other dashed lines shown in all figures, whether on reloading or unloading, were drawn parallel to this original dashed line.

3.3.1 Loading Normal to the c-axis[‡]

When the load was applied normal to the c-axis, i.e. edge-on to the basal planes, at the highest peak loads (≈ 500 mN) delamination and/or cracks resulted in distinct pop-ins in the load displacement curves (Fig. 14a). The load at which the pop-ins occurred was somewhat stochastic, but most pop-ins occurred at loads over ≈ 300 mN. Whenever, a pop-in were recorded, the indents were clearly visible (see SEM micrograph in Fig. 14a). A good correlation was found between the extent (in nm) of the pop-ins and the size of the cracks measured in the SEM, confirming their relationship. Interestingly, in two cases, no pop-ins were observed even at 500 mN (Fig. 14a).

[‡] Where appropriate a schematic of the relationship between the loading direction and the basal planes is shown in the figures for each test as a schematic inset.

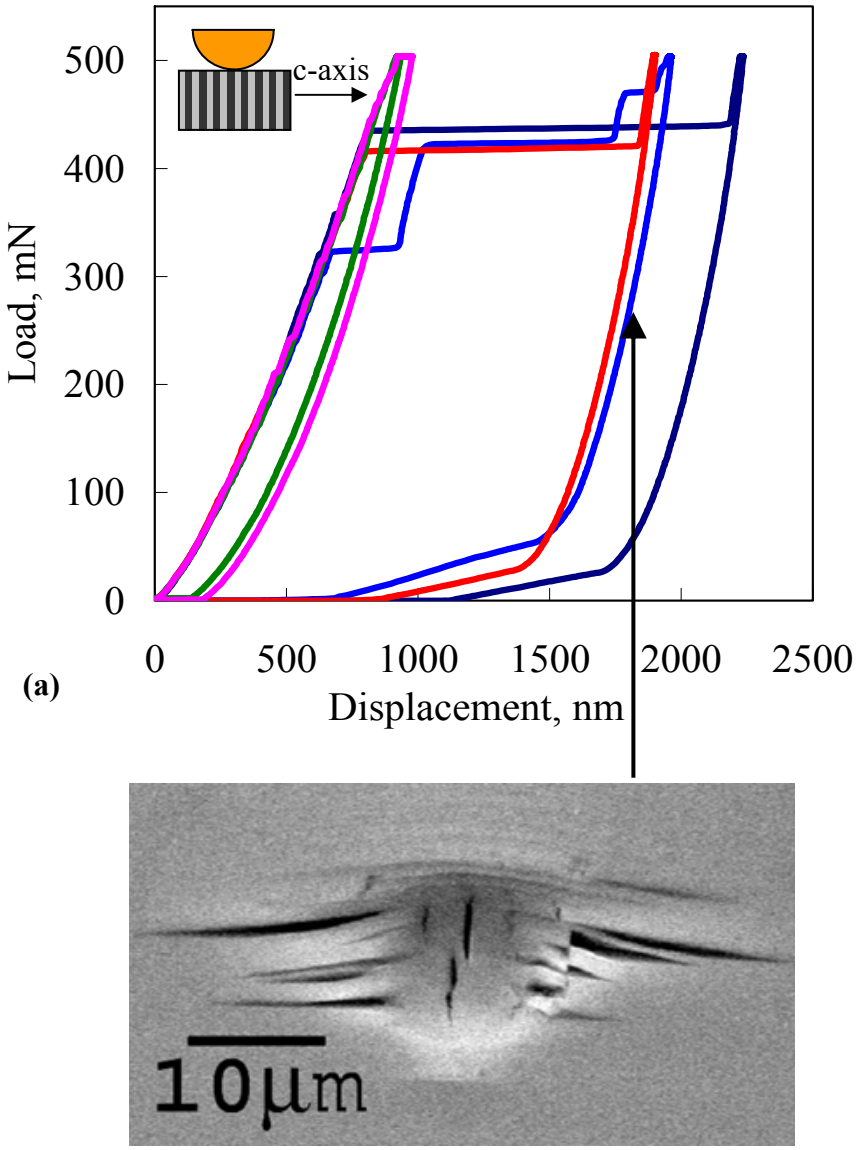

Figure 14: a) Typical load vs. depth-of-indentation response of Ti_3SiC_2 for which the loading direction is normal to the c-axis. (Sketch on left in this and most other figures shows the indenter/c-axis arrangement). Five curves are shown; three show extensive pop-ins that resulted in delamination cracks shown in the accompanying SEM micrograph; the other two did not delaminate and no trace of the indentation was found in the SEM. Note stochastic nature of load at which the pop-ins occur.

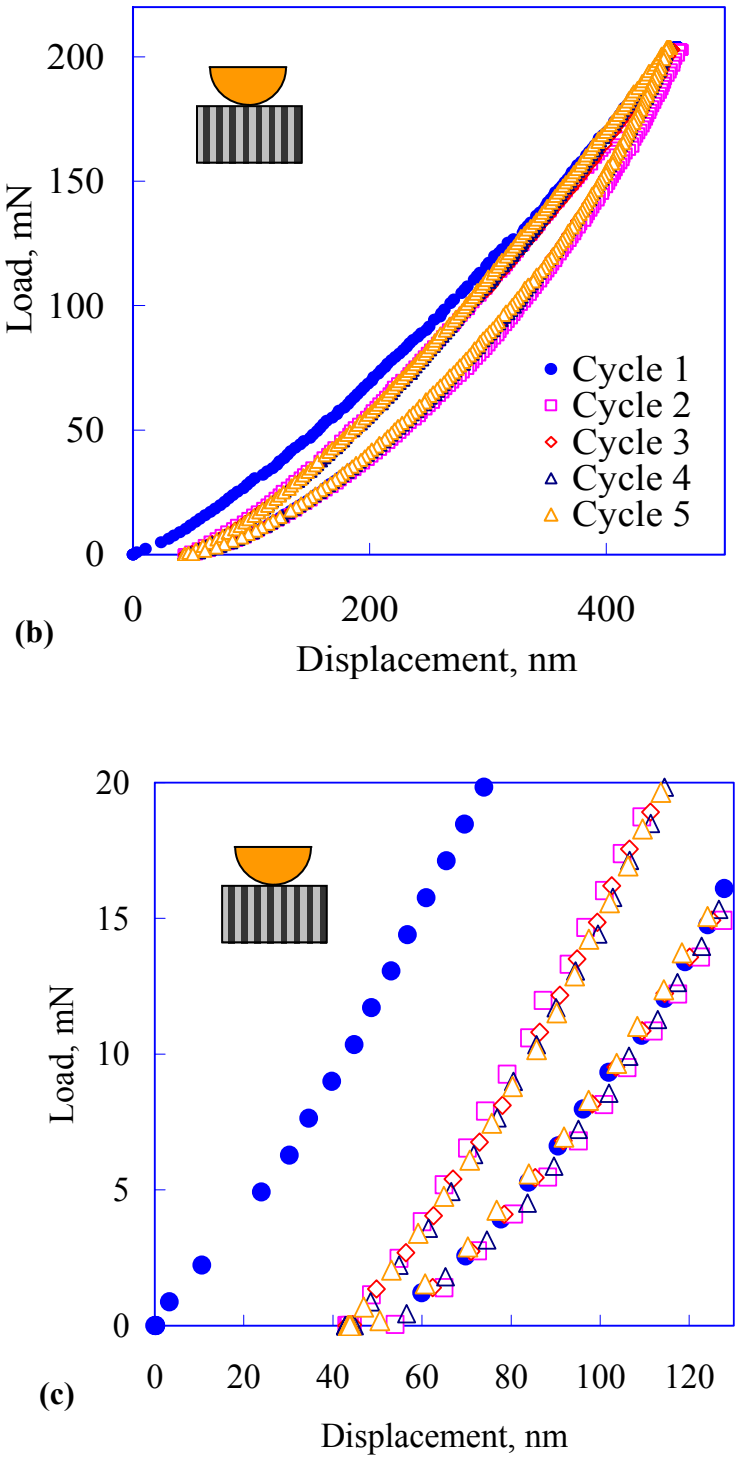

Figure 14: b) Same as a, but for repeat indentations, in the same location, to a maximum load of 200 mN. Note first loop is open, but following 4 are closed. c) Expands the low load region. Major hardening occurs between the first and second cycles.

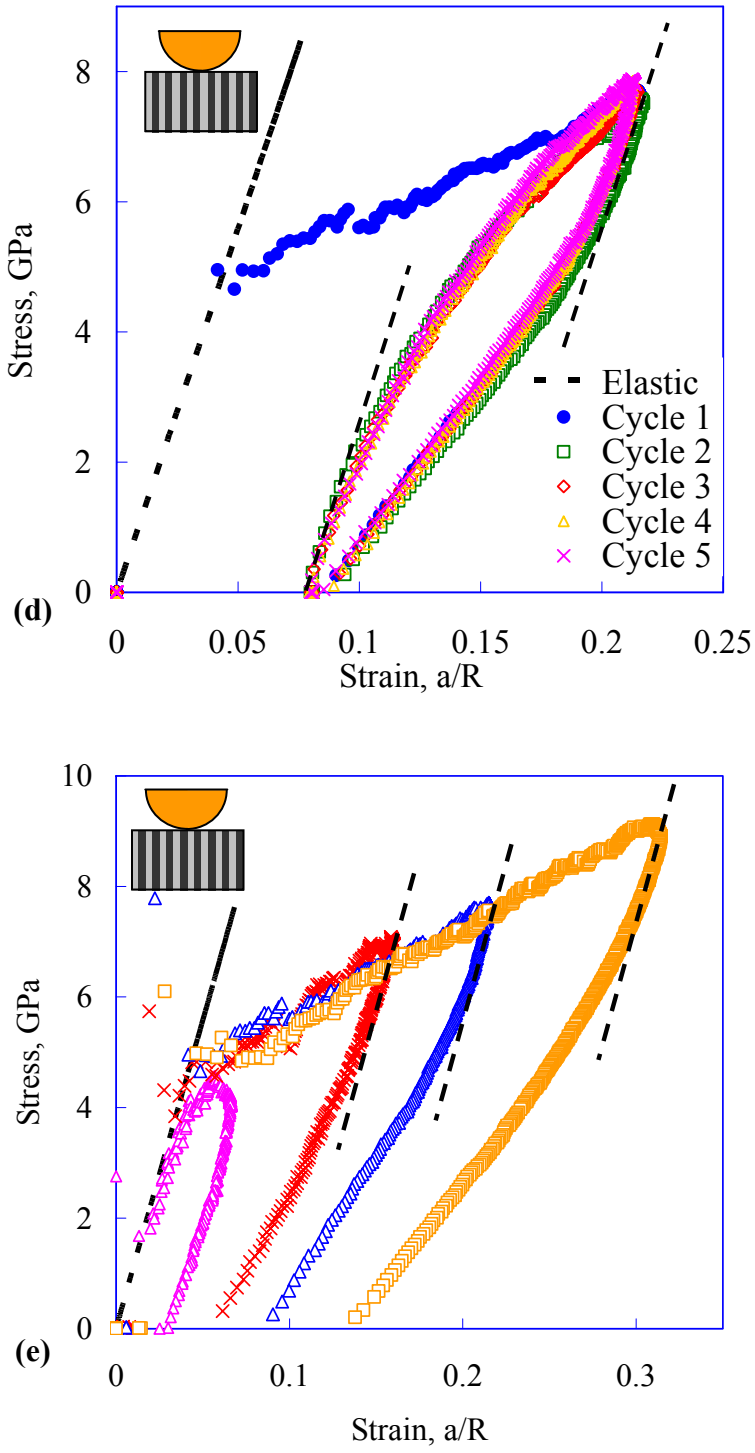

Figure 14: d) Contact stress vs. strain for results shown in b. Note full reversibility of repeat loops. e) Contact stress vs. strain for 4 different loads on four different locations. The inclined dashed lines corresponds to modulus of 320 GPa.

Generally at loads less than ≈ 300 mN, no pop-ins were observed and typical results obtained from multiple repeat indentations on the same location at 200 mN, are shown in Fig. 14b and c. In this regime, the first loop is slightly open indicating a small (50 to 100 nm) residual permanent deformation. However, the next four indentations, on the same location, result in fully reversible, almost indistinguishable, hysteresis loops (Fig. 14b). The areas encompassed by the repeat loops are always smaller than the first loop (Fig. 14b), clearly indicating hardening. The corresponding stress-strain curves for the loops shown in Fig. 14b are shown in Fig. 14d. Not surprising, the first loop is open, but the next four loops are indistinguishable from each other and, most important, are fully reversible. Fig. 14e shows the stress-strain curves for 4 indentations (1^{st} cycles) on different locations at 10, 100, 200 and 500 mN. The reproducibility of the loading curves at the higher loads and that of the indentation yield points is noteworthy.

To study the response at low load levels in more detail, repeated nanoindentation measurements at 10mN were performed. The load displacement and corresponding stress-strain curves are shown in Fig. 15a and b. It is gratifying that the loading and unloading curves, for the five cycles, are parallel to each other and consistent with the assumed modulus of 320 GPa. Another interesting aspect of these results is that, in contradistinction to the results obtained at higher loads (Fig. 14d), there is no hardening observed at these loads. Despite stresses at the tip of the indenter of the order of ≈ 8 GPa, and the repeat nature of the indentations with no pop-ins, typically *no trace* of the indentations was found in a FESEM. In a few sporadic cases, a subtle patch was noted in the FESEM.

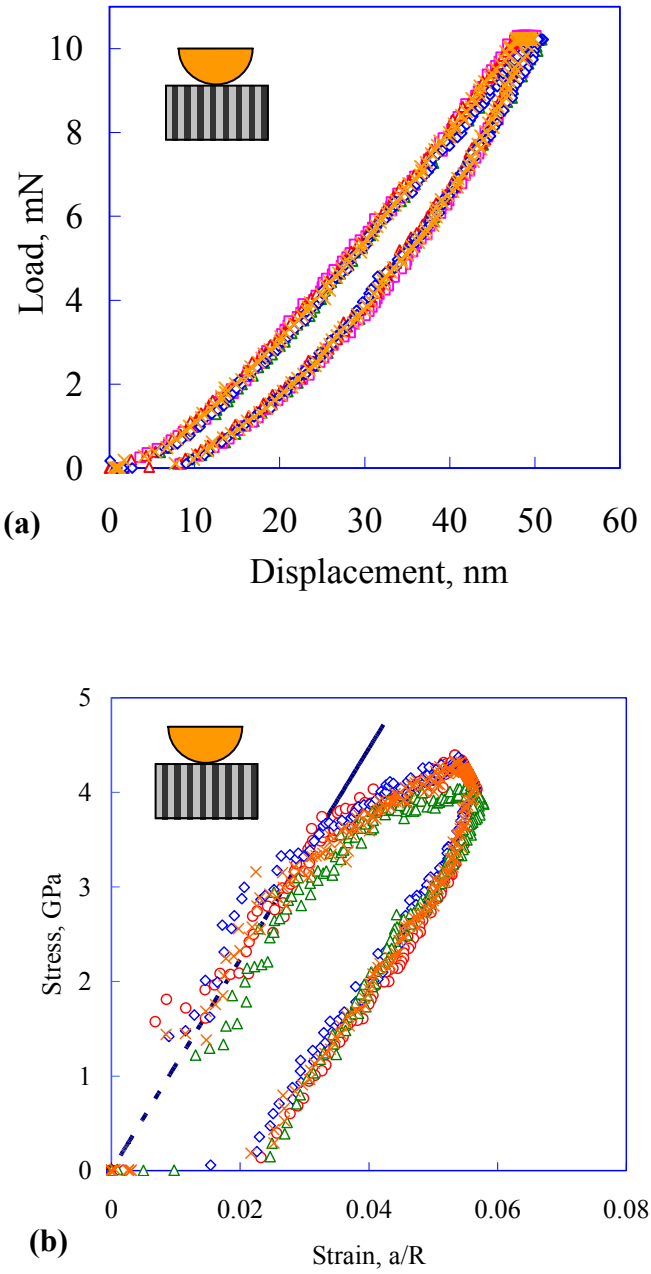

Figure 15: a) Load displacement for indentation normal to the c-axis up to 10 mN. b) Corresponding contact stress vs. strain – note repeatability and reversibility even from the first indents

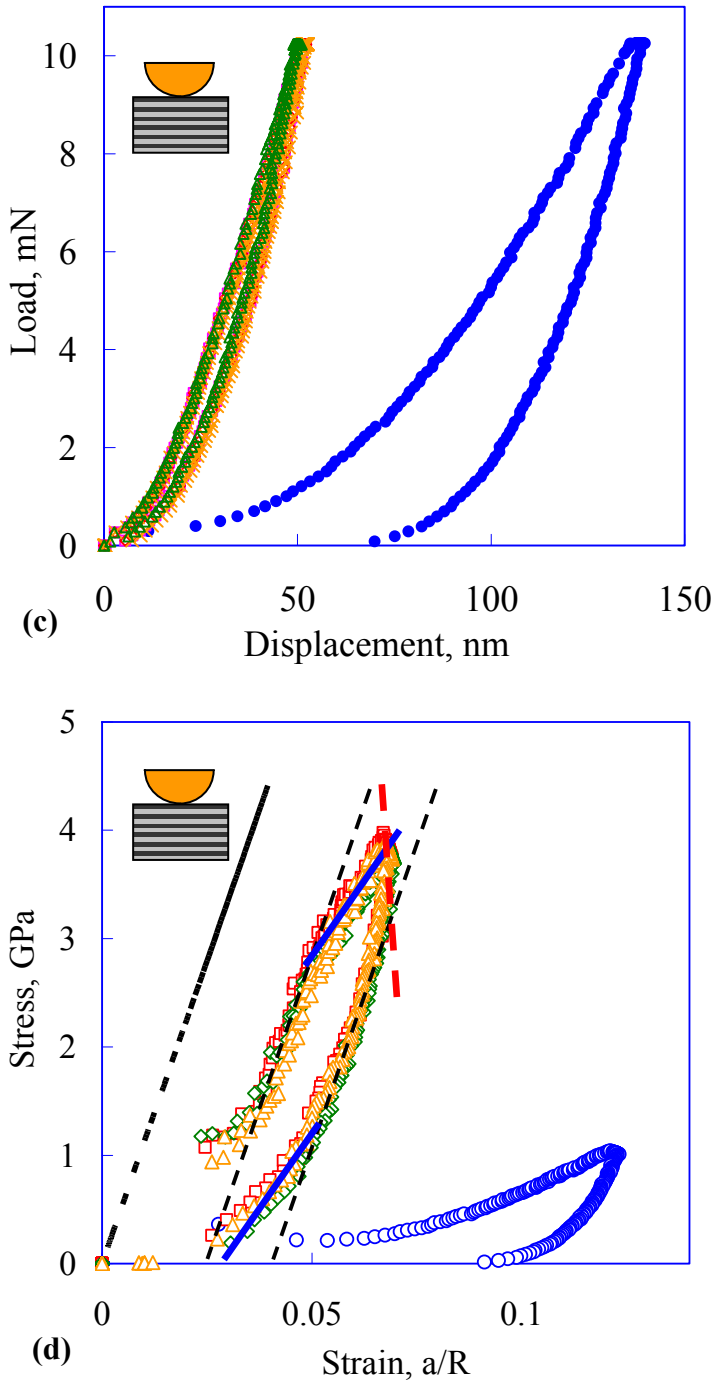

Figure 15: c) Load displacement parallel to the c-axis at 10 mN. First cycle is characterized by large deformations and low stresses. Second and subsequent cycles are almost identical in shape and size. d) Corresponding contact stress vs. strain; the short inclined colored lines are guides to the eye showing the feeble dependence, if any, of yield points on total strain. However, the subsequent indents have much higher stresses, though loaded to the same maximum load of 10 mN. Such a situation is not possible.

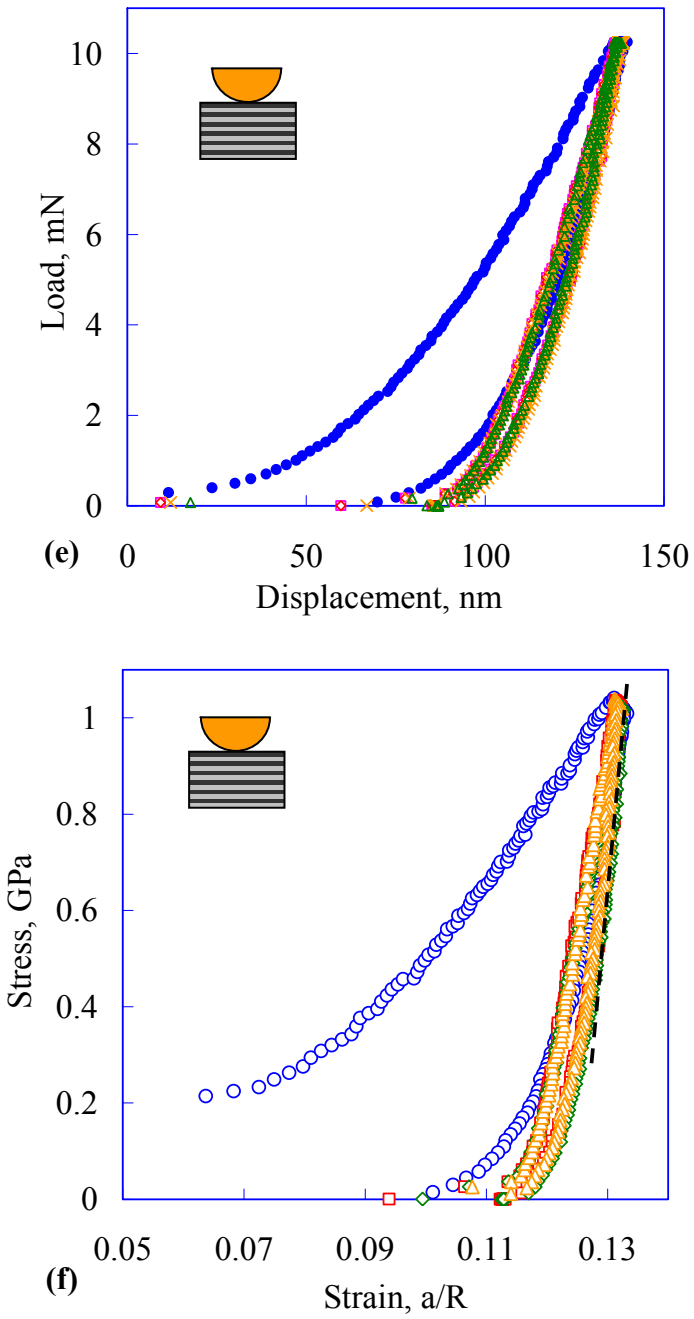

Figure 15: e and f) Load displacement and stress strain with corrections for apparent permanent displacement of the first indent – the unloading curves in the stress strain match very well for a modulus of 325 GPa (black dotted line).

3.3.2 Loading Parallel to the c-axis

When the maximum load (500 mN) was applied parallel to the c-axis, the propensity and especially the extent of pop-ins were greatly reduced (Fig. 16a) compared to when the load was applied parallel to the c-axis (compare Figs. 14a and 16a). In some cases there was a clear indication of selective slip of surface layers relative to bulk (see micrograph in Fig. 16a) that are not unlike the bunching up of a rug.

In general, the results obtained in this direction were less reproducible than the ones loaded in the orthogonal direction. The indentations in this direction sometimes had an extended penetration at low loads (e.g. Fig. 15c) and the results were thus quite stochastic. The differences between the repeat cycles, however, were much smaller. Possible reasons for this state of affairs are discussed below.

Typical load-displacement curves (Fig. 16b) obtained when loading to intermediate loads – 100 mN – were similar to those loaded to higher loads. A few small pop-ins were observed, but the repeat cycles were superimposable. Fig. 16c expands the low load area and indicates that the major hardening occurred between the first and second cycles. The corresponding stress strain curves are shown in Fig. 16d, and are reminiscent of those shown in Fig. 15d. The presence of a linear elastic region followed by a plastic region with a back-extrapolated indentation yield point (denoted by a horizontal arrow) of ≈ 4 GPa is apparent. Here again the majority of the hardening occurred between the first and second cycles, after which a saturation of sorts sets in.

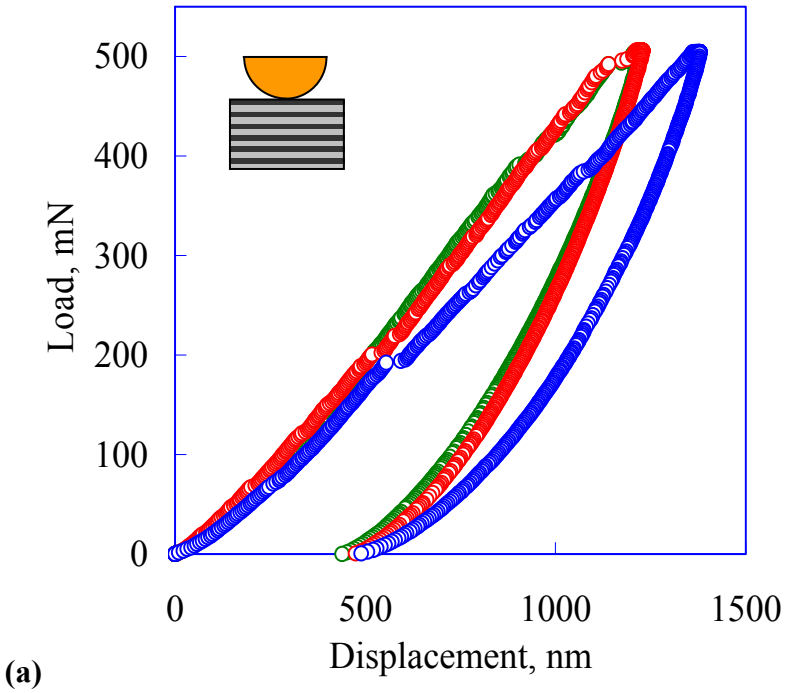

(a)

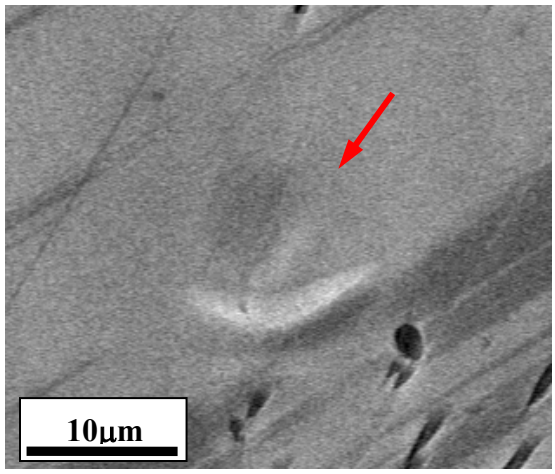

Figure 16: a) Typical load vs. depth-of-indentation response of a Ti_3SiC_2 surface for which the c-axis is normal to the surface. Three curves are shown for 3 different indent locations. In this direction, large pop-ins were not observed; instead features that resembled kinks in carpets shown in SEM micrograph were observed.

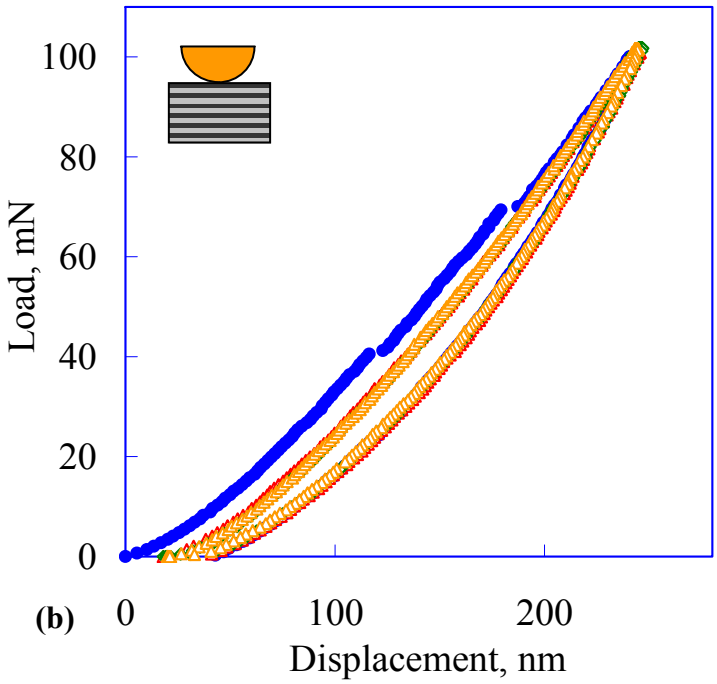

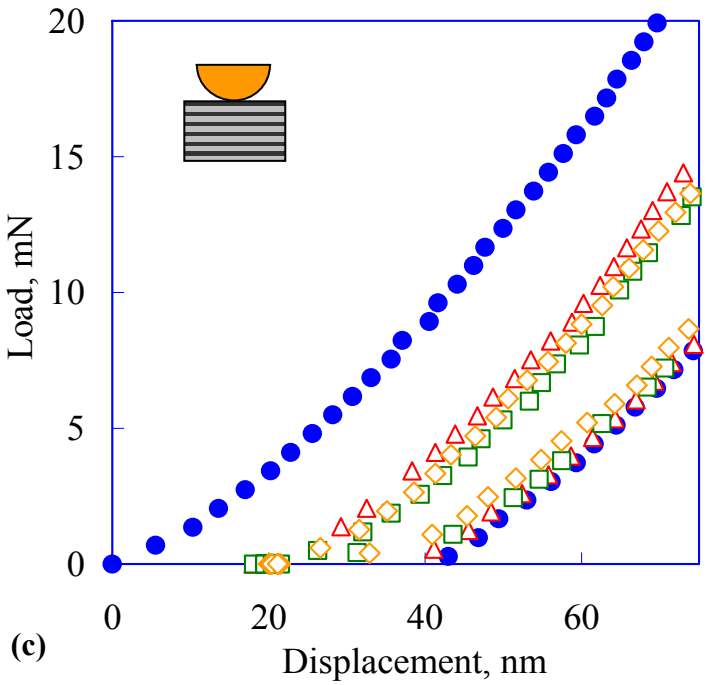

Figure 16: b) Same as a, but for repeat indentations, in the same location, to a maximum load of 100 mN. c) Expands the low load region. Major hardening occurs between the first and second loops. Note first loop is open, but following 4 appear closed.

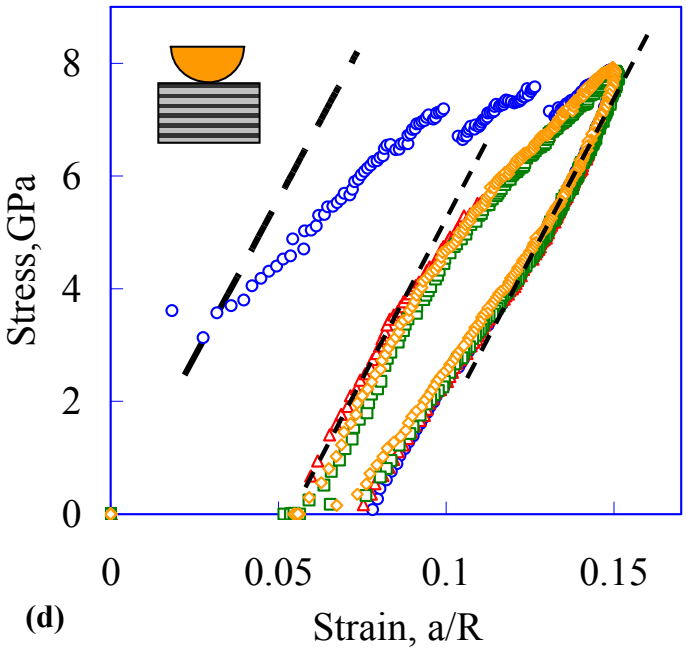

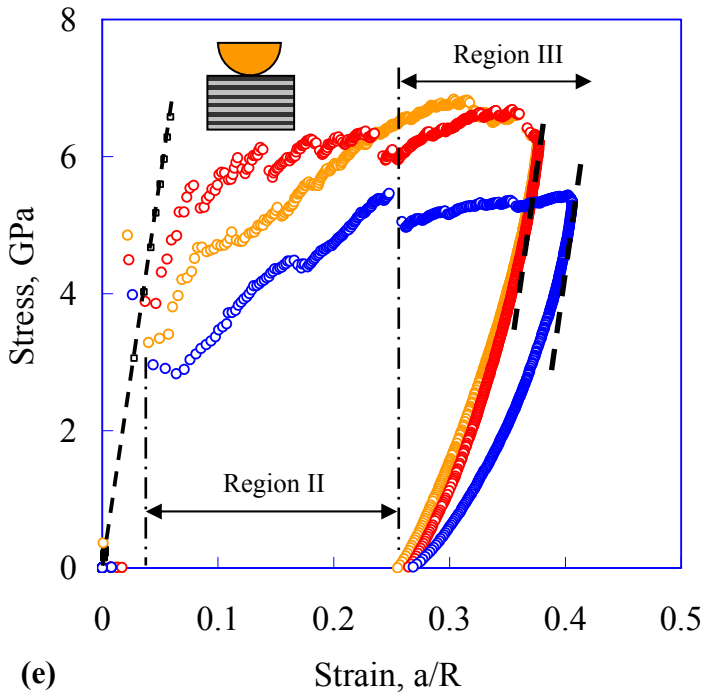

Figure 16: d) Contact stress vs. strain curves for results shown in b. e) Contact stress vs. strain at 500mN on 3 different locations. Note stochastic nature of the yield points. Also note 3 regions; a linear elastic region; a region II where the hardening is rapid; and region III, where the hardening rate is lower. In both d and e, the parallel inclined dashed lines were drawn assuming a modulus of 320 GPa.

The stress-strain curves for single indentations loaded to the maximum load (Fig. 16a) are shown in Fig. 16e and are characterized by 3 regimes: Linear elastic, followed by a region where the hardening rate is relatively high (region II in Fig. 16e), followed, at the highest stresses by a region in which the hardening rate is much reduced (region III, Fig. 16e). Note the variations in the yield points in this direction are significantly more scattered than the ones shown in Fig. 14e.

As before, to study the response at low load levels in more detail, we carried out repeated indentations at 10 mN in this orientation as well. The resulting indentation stress-strain curves are shown in Fig. 15d and - if one ignores the first cycle, which is characterized by a large deformation at low stresses - the remaining curves are quite similar. However, the subsequent indents have much higher stresses, though loaded to the same maximum load of 10 mN. Such a situation is not possible. Also the initial unloading has a negative slope (dotted red line), which is not likely. Fig. 15 e and f plot the same data as in Fig. 15 b and c, but with the corrections for the residual permanent deformation of the first indent taken into account. In this case the unloading curves in the stress strain match very well for a modulus of 325 GPa (black dotted line). Thus corrections for the first indent have to be taken into account despite the very low stresses as a result of this procedure (1 GPa compared to 4 GPa).

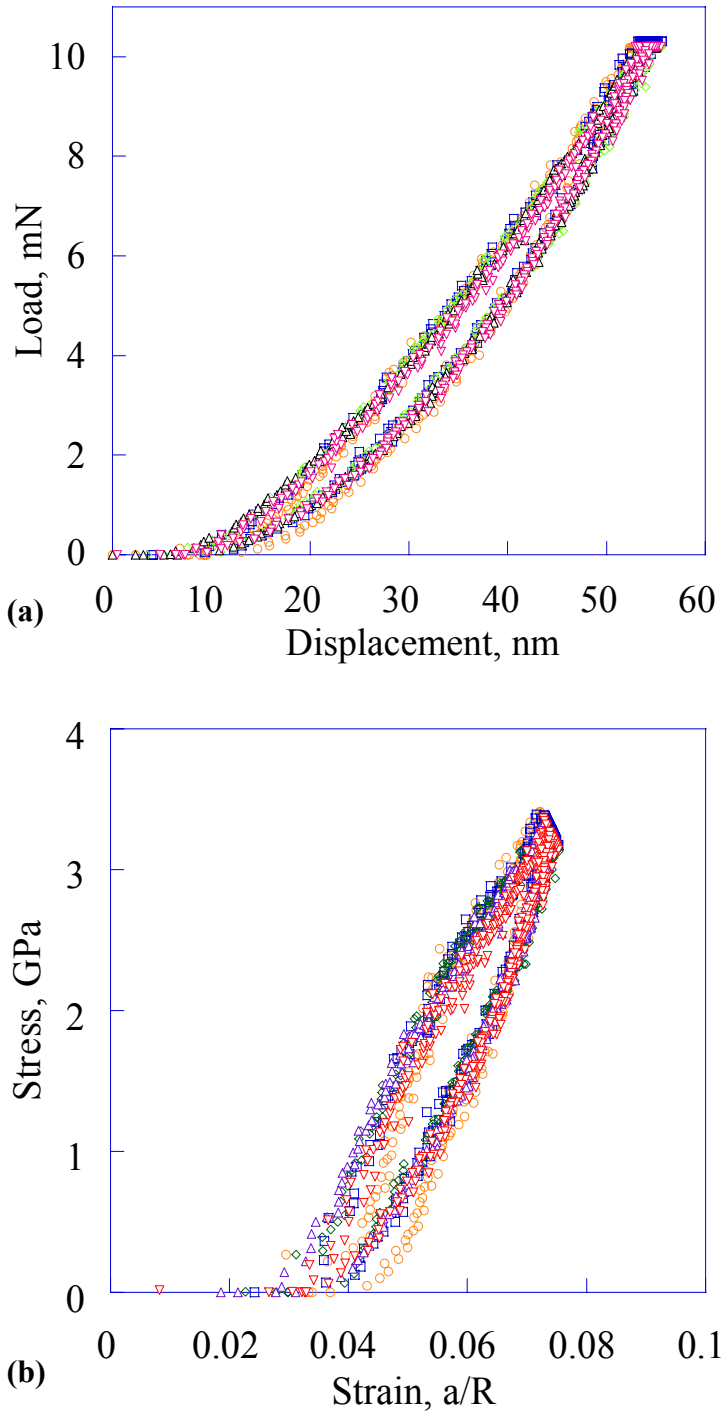

Figure 17: a and b) Typical Load displacements and stress strain on fine grained Ti_3SiC_2 (Random orientation of grains) at 10mN.

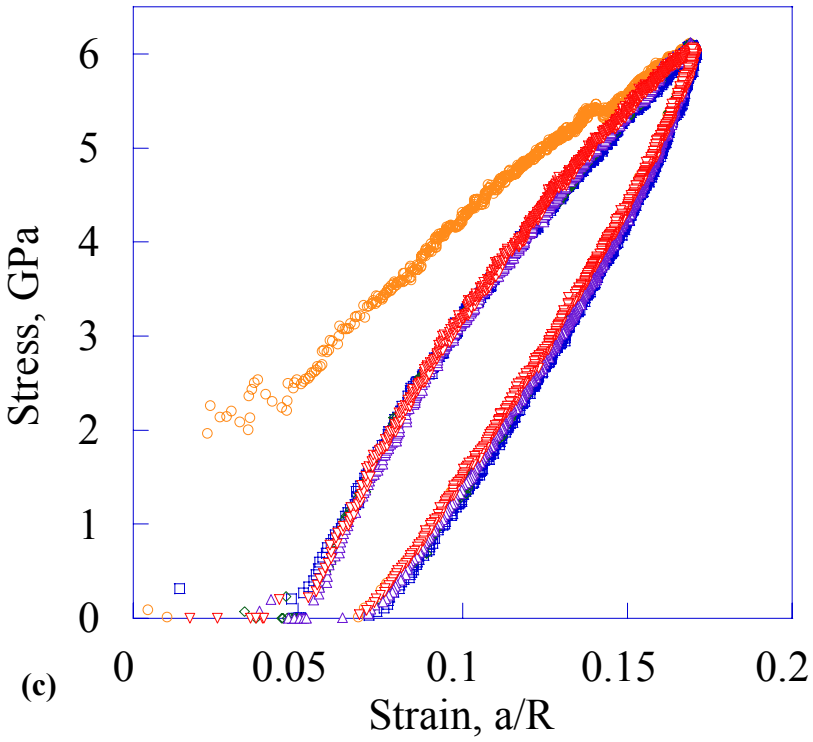

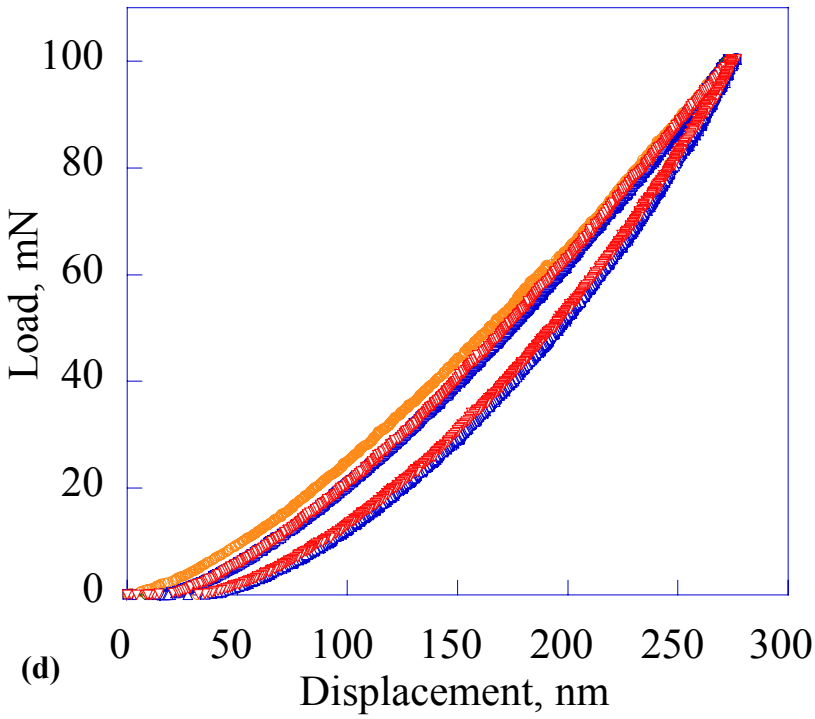

Figure 17: c and d) Typical Load displacements and stress strain on fine grained Ti_3SiC_2 (Random orientation of grains) at 100mN.

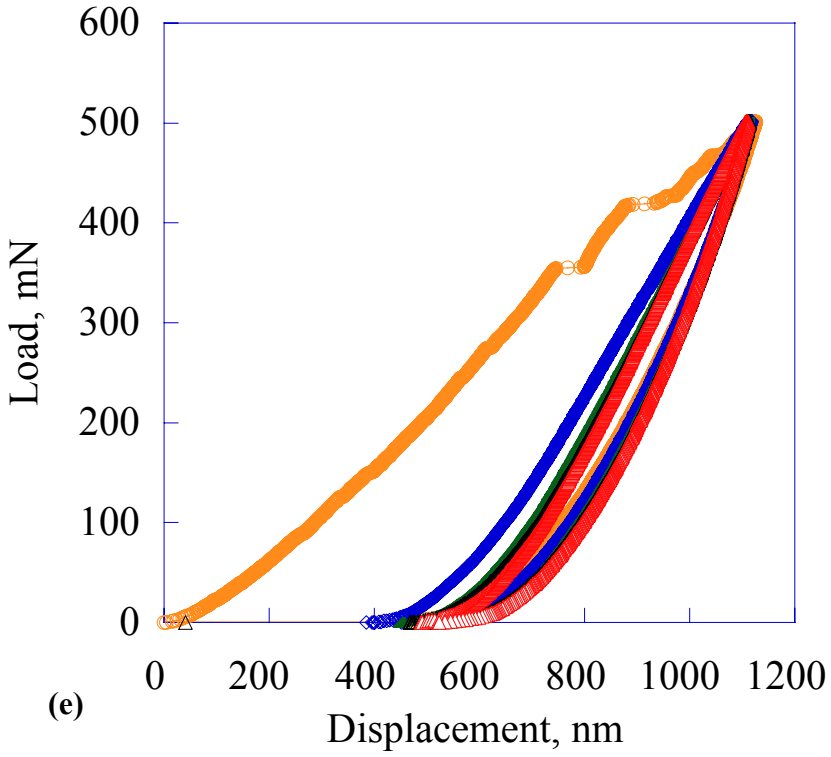

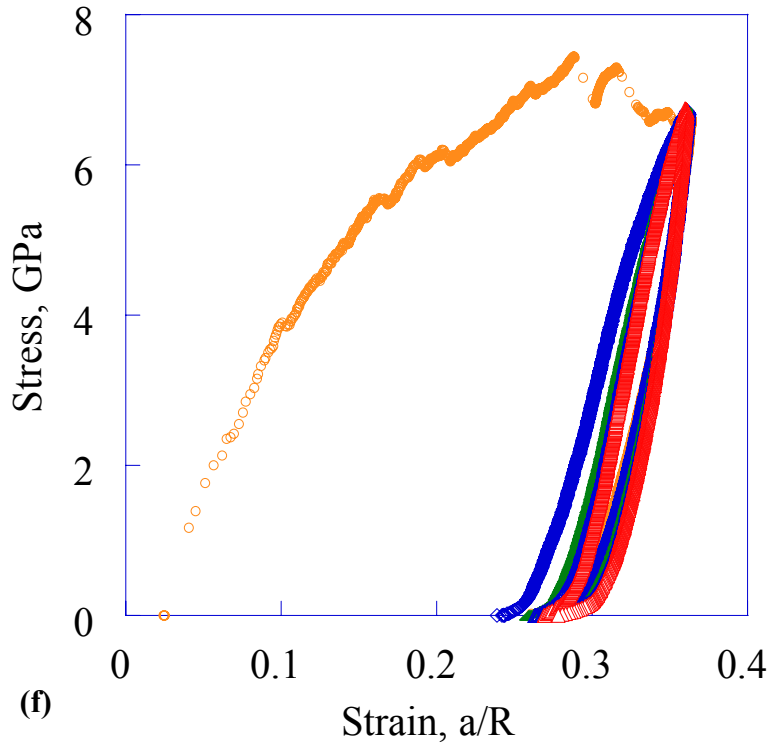

Figure 17: e and f) Typical Load displacements and stress strain on fine grained Ti_3SiC_2 (Random orientation of grains) at 500mN.

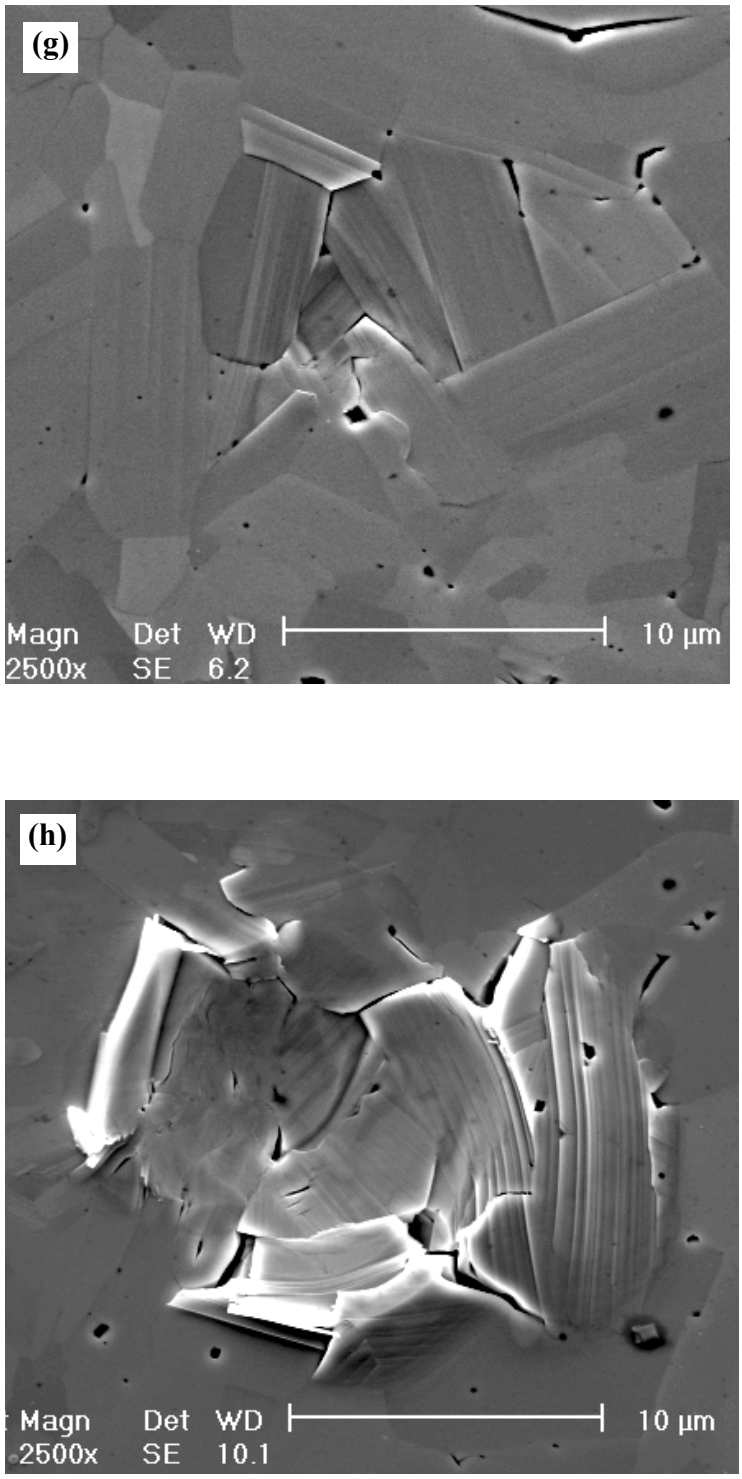

Figure 17: e and g) SEM micrograph of indents at 200mN (g) and 500mN (h).

Load cycle indentations similar to those done on single grains were carried out on polycrystalline fine grained Ti_3SiC_2 (grain size approx. 5 to 10 μm). The results obtained were qualitatively very similar to those obtained from single crystals, except the loops were more open at higher loads (due to grain boundaries). The load displacement, stress strain results are shown in Fig. 17 a to f for 10mN, 100mN and 500mN. FESEM micrographs of the indents at 200mN and 500 mN are shown in Fig. 17 g and h. The micrographs show deformation in multiple grains under the indenter.

3.3.3 Dissipated Work

Fig. 18 plots a log-log plot of W_d vs. σ as determined from the indentation stress-strain curves reported herein. Also included are the results obtained in our earlier work [22]. The agreement between the two sets of results is quite good considering the over 6 orders of magnitude range in W_d covered by the data and the difference in the definition and extraction of stress and strain, between the uniaxial case [22] and this work. The most compelling evidence, however, that the *same* mechanisms are operative at the different stresses in both Ti_3SiC_2 and graphite is shown in Fig. 18b. In this plot, both axes are normalized by the appropriate elastic stiffness along the indentation axis; (i.e. 325 GPa for Ti_3SiC_2 and 36.5 GPa for graphite). Based on the resulting *universal* curve it is fair to conclude that the same kinking-based mechanisms are operative in these materials.

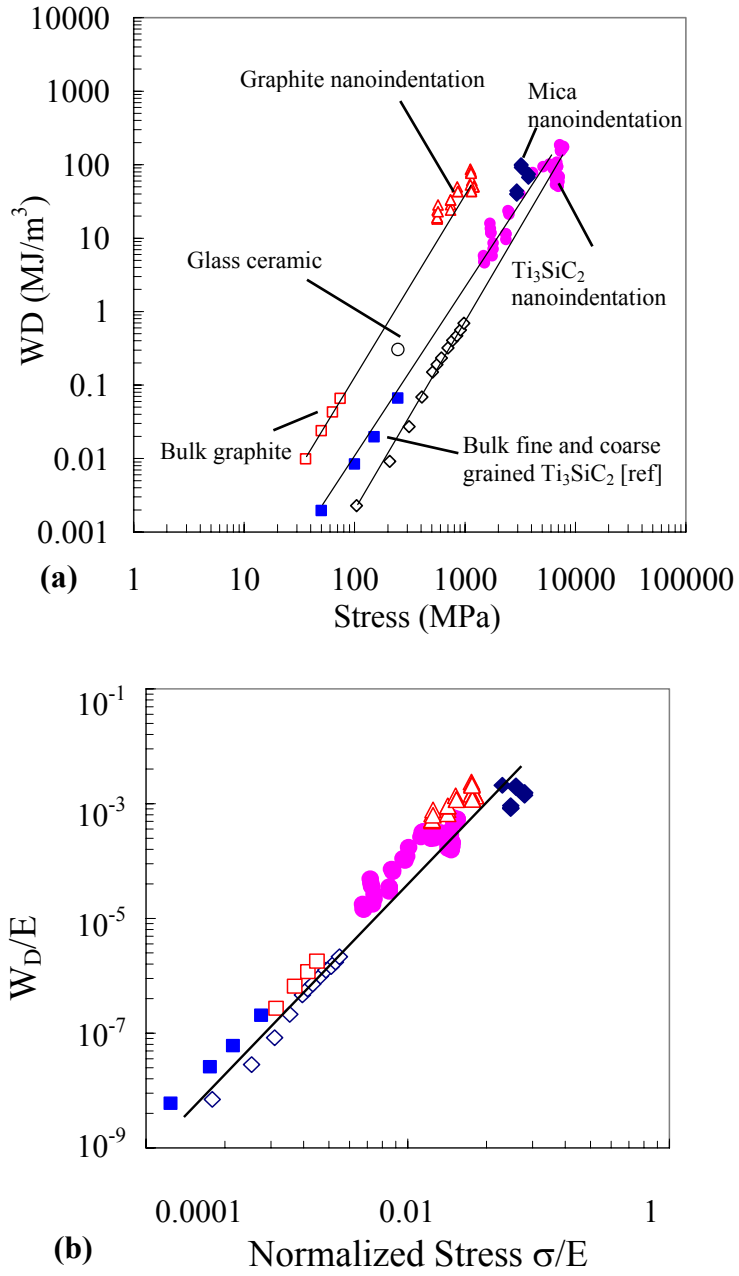

Figure 18: a) Log-log plot of energy dissipated per cycle, W_d, versus maximum stress applied, σ for Ti_3SiC_2. The results in the lower left hand corner were obtained from simple compression results of bulk samples[22]. The ones in the upper right were obtained from the stress-strain curves generated in this work. The agreement is good despite the over 6 orders of magnitude range in W_d. The corresponding results for graphite are also shown [51]. b) Same plot but with both axes normalized by either the Young's moduli (bulk) or c_{33}. For Ti_3SiC_2, 325 GPa was used, for graphite 36.5 GPa [1] and for mica 61 GPa [77].

3.4. Discussion

As far as we are aware, the formation of near-fully reversible hysteresis loops, followed by hardening and fully reversible loops (e.g. Figs. 14b and c) has never been reported in any other *dense*, crystalline solid. Field and Swain [3,25], Iwashita et al. [4] and Sakai et al. [2] reported similar results but in glassy carbons.

For the most part, the dashed lines (e.g. Fig. 14d and e), based on a modulus of 320 GPa, fit very well for the initial portions of the loading and unloading curves for both the orientations, confirming that the moduli along the *a* and *c*-directions in Ti_3SiC_2 are not too different; a conclusion consistent with recent *ab initio* calculations [40]. It is also in agreement with the mild anisotropy in thermal expansions along the *a* and *c*-directions [41]. In that respect Ti_3SiC_2 is quite different from other layered materials such as graphite or mica that are both elastically and plastically anisotropic.

In order to understand and explain the majority of the results reported herein it is essential to invoke the presence of three interrelated dislocation-based elements that appear in the solid as the stress is progressively increased:

i) Incipient Kink Bands, IKBs

ii) Mobile Walls, MWs, that form when the walls comprising the IKBs detach from each other.

iii) Immobile Kink Boundaries, KBs, that are thin areas in which the MWs have collapsed. The KBs are indistinguishable from high angle grain boundaries.

The strongest, and almost irrefutable, evidence for the presence of IKBs are the repeat cycles shown in Figs. 14b, c and d. That the response is fully reversible is evident and

that hardening has occurred between the first and second cycles is also indisputable. These two facts alone rule out phase transformations and/or microcracking. Furthermore, the fact that the energy dissipated is very large – of the order of > 1 GJ/m^3! (Fig. 18) – and reproducible is consistent with an interpretation in which not only are there numerous dislocations, but the latter can apparently glide *reversibly* over relatively large distances.

The hardening observed between the first and second cycles can be explained in the context of the KB model. During the first cycle, at low loads, an IKB is nucleated; at intermediate loads it splits forming pairs of MWs that eventually collapse into KBs.

The concept of IKBs was first proposed by Frank and Stroh [42], for deformation of high c/a ratio materials such as zinc where twinning was not observed. An IKB is formed, under an applied stress, by the generation of two almost parallel dislocation walls of opposite polarity that are attached at the ends as shown in Fig. 19. The applied stress σ keeps the strongly attractive dislocation walls of opposite polarity separated. Thus the IKB remains stable as long as the applied stress is present, thus the walls would collapse as soon as the applied stress is removed. Such a mechanism would be operative when there are no dislocation entanglements such as in the case of cross slip and when twinning is energetically not favorable due to high c/a ratios (typically > 1.7 for metals). At higher stresses, the IKBs form mobile walls where the ends of the IKB are no longer attached and thus can radiate outwards, a number of which eventually can collapse to form a permanent KBs. Please note that the mobile walls need not collapse thus not forming typical kinks, observed in many materials including rocks and geological minerals. A high angle kink boundary is similar to a twin in that it is a mirror image plane, however, the angle between the atomic planes on either side of the kink boundary

are not fixed as in the case of twins, but are a function of the severity of the kink boundary; vis. the number of MBWs incorporated in the kink boundary.

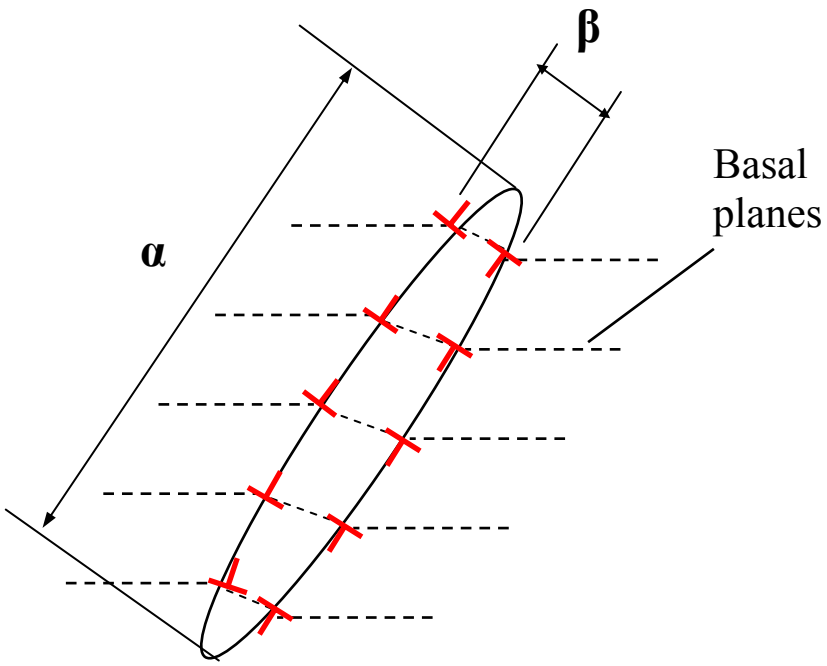

Figure 19: Schematic of an incipient kink band (IKB), with dimensions α and β. The applied stress keeps the dislocation walls apart that are attached at the ends. The IKB will collapse once the applied stress is removed due to the strong attractive nature of the dislocations.

According to Frank and Stroh, the remote shear stress, τ, needed to trigger an IKB – i.e. render a subcritical kink band, critical - is given by [42]:

$$\tau \geq \sqrt{\frac{2bG^2\gamma\ln(1/\gamma)}{\alpha\,\pi^2(1-\nu)^2}} \qquad (1)$$

where G, ν and b are, respectively, the shear modulus, Poisson's ratio and the Burgers vector. α is the domain size available for the creation of the IKB. γ is the critical kinking angle above which the growth of a subcritical kink band becomes critical and is given by:

$$\gamma_c \approx 3\sqrt{3}\frac{\tau_c}{2G(1-\nu)} \tag{2}$$

where τ_c is the local critical shear stress needed to create a dislocation pair in a perfect crystal. For metals this value is typically taken to be $\approx G/30$. Using this value for τ_c and a ν of 0.3 in Eq. 2, yields a critical angle of $\approx 3.5°$. Thus above which, the subcritical kink band forms an IKB, which would collapse once the applied stress is removed.

The stress τ_c depends on the domain size α – smaller the α, larger the stress required to nucleate an IKB. Forming and annihilation of these IKBs results in energy losses; this is due to the back and forth motion of the dislocations comprising the IKBs that are subjected to lattice friction or lattice resistance. As in other layered solids, dislocations are mobile along the basal planes and do not cross slip and thus they do not entangle and work harden. These dislocations can move reversibly relatively over large distances and thus can dissipate substantial amounts of energy during each cycle. At sufficiently high stresses, the IKBs devolve into MDWs, a number which can collapse together forming a KB. Formation of a KB would reduce the domain size available for the formation of a IKB and thus leading to hardening, a characteristic of these layered solids.

The most important ramification of Eq. 1, is that as α shrinks, the remote stresses required to initiate new IKBs increase accordingly. Once a KB is formed, and as long as the stress is not increased above the initial stress, the only element that can nucleate is a

fully reversible IKB. This is evident from the multiple indentations shown in Figs 14d and 15d, where the first load displacement loops have a larger area and the subsequent indents have smaller area (thus implying hardening).

In one test, the sample was indented to a load of 5 mN and in the same location repeated indents of 10mN load was superimposed. The results are shown for both the orientations in Fig. 20 a and b. As evident from Fig. 20a and b, loading to 5mN multiple times shows no difference between the first and the subsequent indents. In this regime, there are no KBs formed – only IKBs are active, thus hysteretic response is observed but there is no hardening. However, when the sample (parallel to the c-axis – Fig. 20a) was subsequently loaded to 10mN multiple times, the second 10 mN indent showed distinct hardening after about 6 mN. Thus during the first indent, after about 6mN – IKBs to mobile walls transformation takes place.

Multiple indents at 10mN afterwards was repeatable similar to the second indent. However, there is not much difference in the loading behavior when the sample was loaded normal to the c-axis (Fig. 20b). This implies that in this orientation, the stresses needed to bring about IKB to mobile walls transformation are higher compared to loading parallel to the c-axis.

The idea of microstructure that ultimately reaches an equilibrium configuration – defined as one in which mobile dislocation walls are absent - for a given stress must clearly be invoked to explain the behavior of the material when loaded parallel to the c-axis (Fig. 16d) and at low loads normal to the c-axis (Fig. 15). In both cases, the loading and unloading curves are parallel (particularly in Fig. 15b) and a permanent strain is recorded during each cycle.

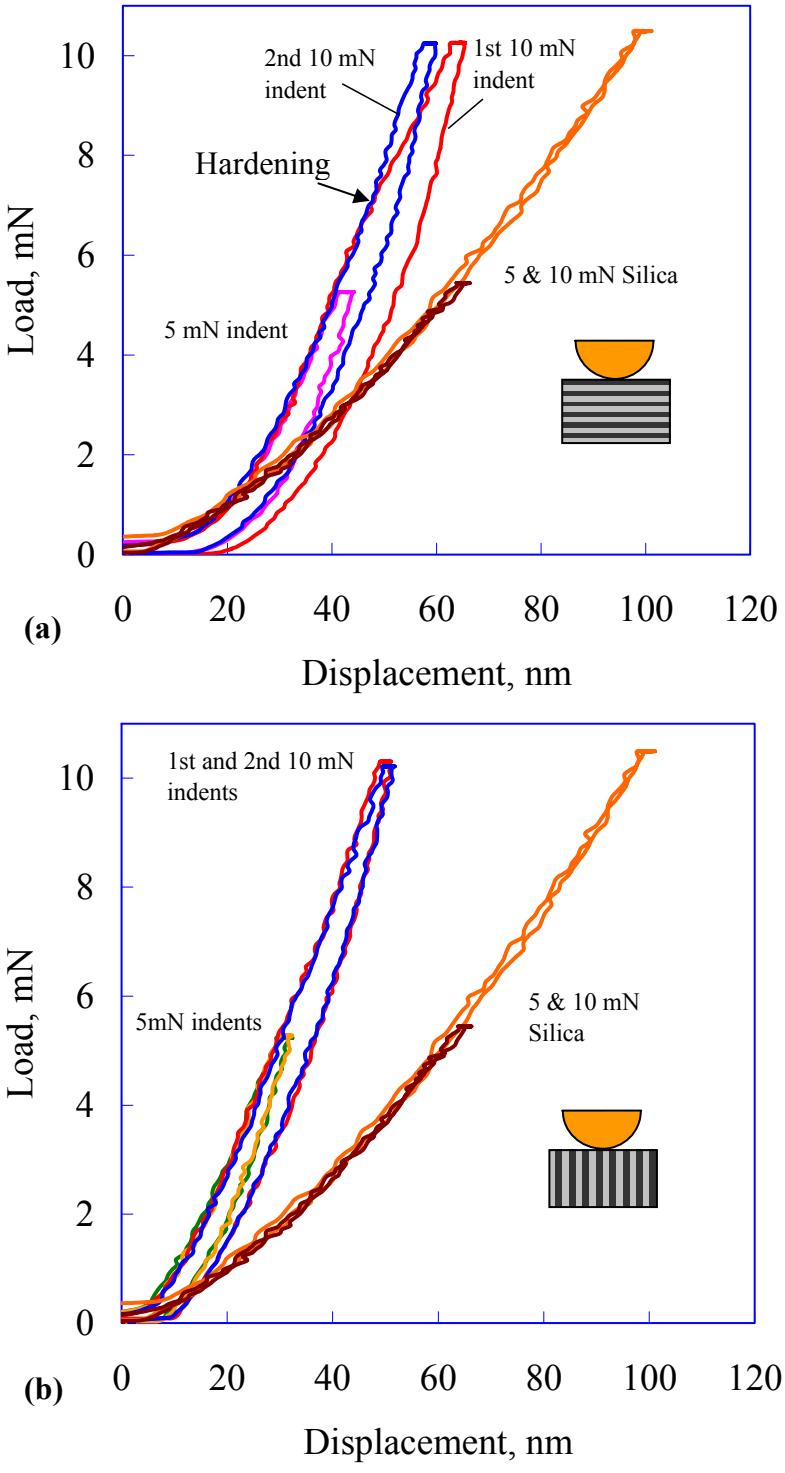

Figure 20: Typical low load vs. depth-of-indentation response of Ti_3SiC_2 for which: a) Indentations are parallel to the c-axis. The indentations at 5 mN are reproducible Reloading to the same area to 10 mN results in the loop labeled 1st 10 mN indent. On further loadings (2nd 10 mN indent), hardening beyond ≈ 5 mN is observed. b) Indentations are normal to the c-axis. Note lack of hardening. Also included in both figures in way of reference are the indentation results for fused silica.

In context of our model, the simplest explanation is one in which a series of MWs radiate away from central IKB sources. Because the walls are parallel, they repel each other, but remain mobile, explaining both the source of the strain and the lack of hardening. Needless to add, at some point, the MWs collapse and form KBs, at which time the microstructure evolves towards equilibrium, ultimately leading to full reversibility. That an equilibrium microstructure does develop is best evidenced by the changes in shape of the stress-strain loops as the load in increased from 10 mN (Fig. 15a) to 500 mN (Fig. 14d). At higher loads the repeat loops are fully reversible.

The results presented here are in complete agreement with our recent work [22] in which it was concluded that the formation of IKBs at room temperature - that gave way to KBs at higher temperatures - were responsible for the fully reversible hysteresis loops obtained in compression [22]. At room temperature, the failure stresses (≈ 1 GPa for fine-grained samples) were insufficient to separate the IKB walls, and the response was fully reversible even for the first cycle. It is only at elevated temperatures that the walls of the IKBs separate and interact, resulting in smaller domains, which in turn account for the cyclic hardening observed at 1200 °C and after cooling. In this work, the large stresses under the indenter and the confined nature of the deformation are sufficient to result in multiple KBs during the first cycle. In other words, the high stresses herein play the role of temperature in our previous work.

Based on the results shown in Fig. 18a, it is reasonable to conclude that the processes occurring at room temperature during the compression of bulk Ti_3SiC_2 samples are the same as the ones occurring under the indenter. Such agreement is consistent with our KB-

based model. Note that the same good agreement between bulk and nanoindentation results is valid for graphite as well (Fig. 18a).

The variability in response for samples loaded parallel to the c-axis is not fully understood at this time. The presence of defects that can act as IKB nucleation sites and thus greatly lower the yield point can also not be discounted. Finally, the grains along the c-direction are much thinner than in the orthogonal direction [18] and there is no easy way to determine the thickness of a given grain before indenting it. This could also have added to the experimental scatter observed.

Direct evidence for micromechanical damage and KB formation under a large spherical indenter was published earlier [16]. Unfortunately the results shown here and those reported in Ref. 16 cannot be compared, because in retrospect, it is now apparent that the deformation in the latter was not truly confined, which explains the strain-softening observed. In Ref. 16, the samples were split in two and re-glued together before loading.

In this work, and despite some attempts, no direct evidence for the formation of KBs under the indentations is presented. Nevertheless, the key role KBs play in the deformation of Ti_3SiC_2 – at all scales - is incontrovertible [9,18-20,35].

Recently, direct TEM evidence for the existence of KBs were observed when epitaxially grown thin films of Ti_3SiC_2 were nanoindented parallel to the c-direction using a Berkovich indenter [35]. Direct TEM evidence for the presence of parallel dislocation walls and associated lattice rotations has also been reported [20,35]. Direct evidence for KBs was very recently been obtained in single crystals of graphite (chapter 4) [43] and mica (chapter 5) [44], where SEM micrographs of areas under the indenter

unambiguously show a transformation of the single crystal into a multitude of much smaller crystals. Based on our recent work, there is thus little doubt that IKBs, MWs and KBs play an important role in the deformation of both graphite and mica – and thus much of geology (chapter 5) [44].

It is also worth noting that reversible load-displacement curves have been reported in the literature in the indentation response of glassy carbons - comprised of nanometer grains and 25-30% volume porosity [3,4,25,45]. The current interpretations for this behavior is attributed to reversible slip of carbon hexagonal network plane layers [2,3] or the reversible slip of dislocation networks, such as pileups at grain boundaries [2]. The data presented here raise the possibility that KBs might play a significant role in those materials as well. This merits further investigation and is described in the next chapter.

CHAPTER 4: KINK BANDS, NONLINEAR ELASTICITY AND NANOINDENTATIONS IN GRAPHITE

4.1 Introduction

Despite extensive work as described in chapter 1, many aspects of the mechanical behavior of graphite are not clearly understood. In the latter part of the discussion section we briefly review the salient features of its deformation and show them to be totally consistent with the kinking-based model discussed herein. As this work makes clear, there are many similarities between the deformation of Ti_3SiC_2 and graphite. To understand the response of the latter it is vital to understand of the deformation of the former, the details of which are given in chapter 2 and explained using the Frank and Stroh model. Frank and Stroh's model as described in chapter 3 is two-dimensional and as such assumed that once a subcritical KB became critical, it would immediately extend to the free surface resulting in two parallel, mobile non-interacting dislocations walls (Fig. 21b). It is the repetition of this process that results in the generation of new dislocation walls whose coalescence form the KB's. The idea that a kink band can reach a grain boundary and not dissociate was not considered, but as discussed here, it is crucial. As defined in this, and previous work [22,44,46] (chapters 3, 5), an incipient kink band or IKB is one in which the near parallel walls of opposite sign dislocations are undissociated, i.e. still attracted to each other, which insures that when the load is removed the IKB's would be annihilated. Thus by definition IKB's are not only fully reversible but are also a key microstructural hysteretic element as explained in chapter 1.

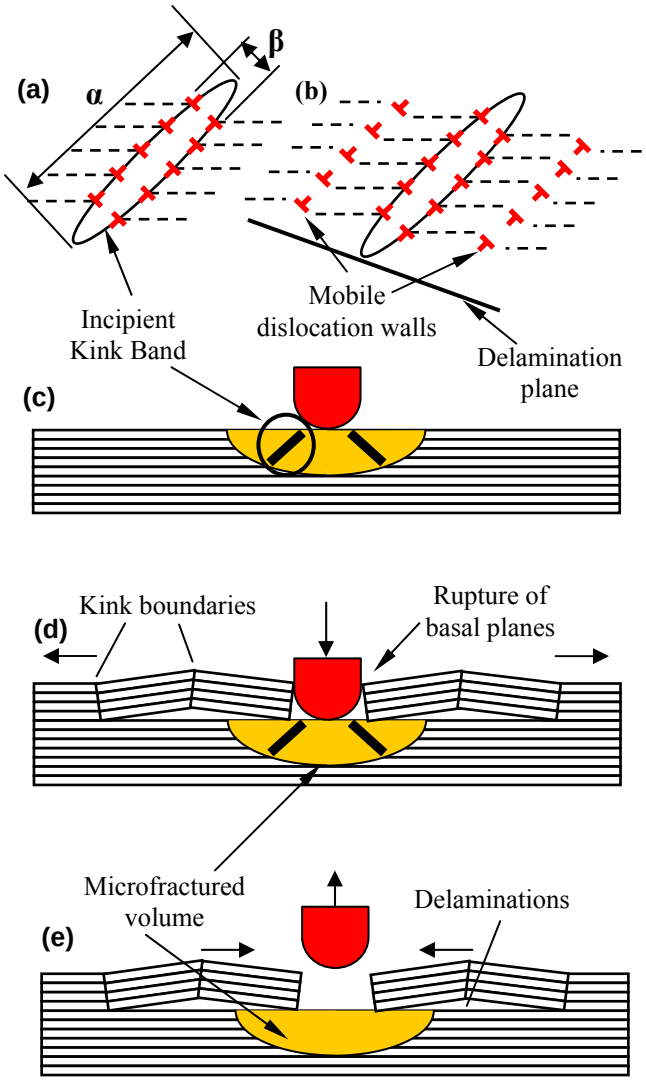

Figure 21: Schematic of, a) Incipient kink band comprised of two walls of dislocations of opposite polarity. As long as the walls remain attached, a strong restoring force exists. b) Same as a, but after the formation of a pair of glissile walls. Note the latter could not have formed without delamination. c) Formation of two IKBs under the indenter. d) same as c, but after massive delaminations and transfer of material from under the indenter to the edges of the indent. Note the crucial role the KBs play in that process. e) Same as c, but after retraction of the indenter, showing possible relaxation.

While numerous papers report on the hardness of graphite, and a few on depth-sensing indentations studies on graphitic materials [2-4,45,47-50], as far as we are aware, none used single crystals, and only rarely have different indenter shapes been compared [47].

Nanoindentation studies have been primarily used for studies of the mechanical properties of thin carbon - diamond and carbide derived carbon, CDC - films. Only recently has it been shown that nanoindentations coupled with Raman spectroscopy and electron microscopy techniques can be used for fundamental studies of the deformation mechanisms in materials especially when single crystals of known orientations are used [48].

The purpose of this work is to report on nanoindentation results of graphite single crystals loaded along the c-axis, viz. normal to their basal planes. We also carried out simple cyclic compression experiments on polycrystalline samples and show that these results – and much of the mechanical response of graphite known in the literature – can be explained by a kinking-based model.

4.2 Experimental Details

Nanoindentations were carried out under load control using both a 13.5 μm radius spherical diamond tip and a Berkovich tip as explained in chapter 2 up to maximal loads of 2, 5, 10, 20, 50, 100, 200 and 400 mN. The loading rate was between 0.6 and 3 mN/s.

To study the effect of cycling, typically multiple (mostly 5) indentations were carried out at the same location to any given load. For the spherical indenter, the load/displacement curves were converted to stress/strain curves as explained in chapter 2.

4.3 Results

In this work, this initial part of the stress-strain curve is ignored, and instead a straight line was drawn through the origin, assuming a modulus along the c-axis of 36.5 GPa [1]. The stress values at strains < 0.05 are unrealistically high and were thus omitted. In the nanoindentations experiments the response of graphite at the lowest loads is linear elastic. Clearly, the purely elastic regime exists *below* the lowest load used in this work, viz. 2 mN, i.e. below a contact stress of < 0.5 GPa (Fig. 22b).

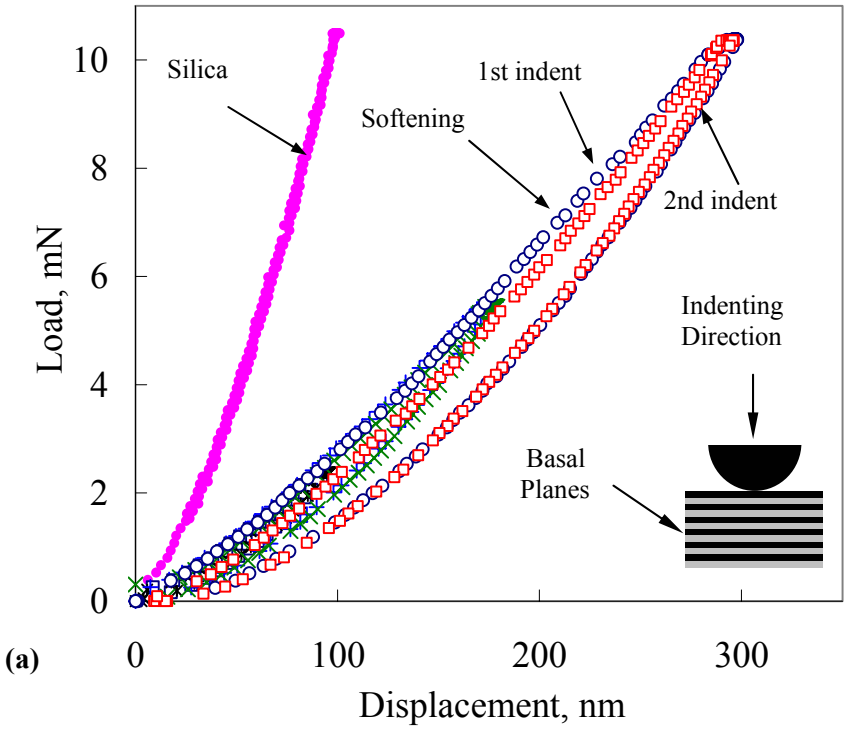

Figure 22: Spherical indents along the 0001 direction in graphite single crystals, a) Multiple indents at 2, 5 and 10 mN. Only the first two successive indents at each loading are shown for clarity. Note softening in the first loading at 10mN load cycle between 5 and 10 mN. Second and subsequent indents to 10 mN are harder than the first.

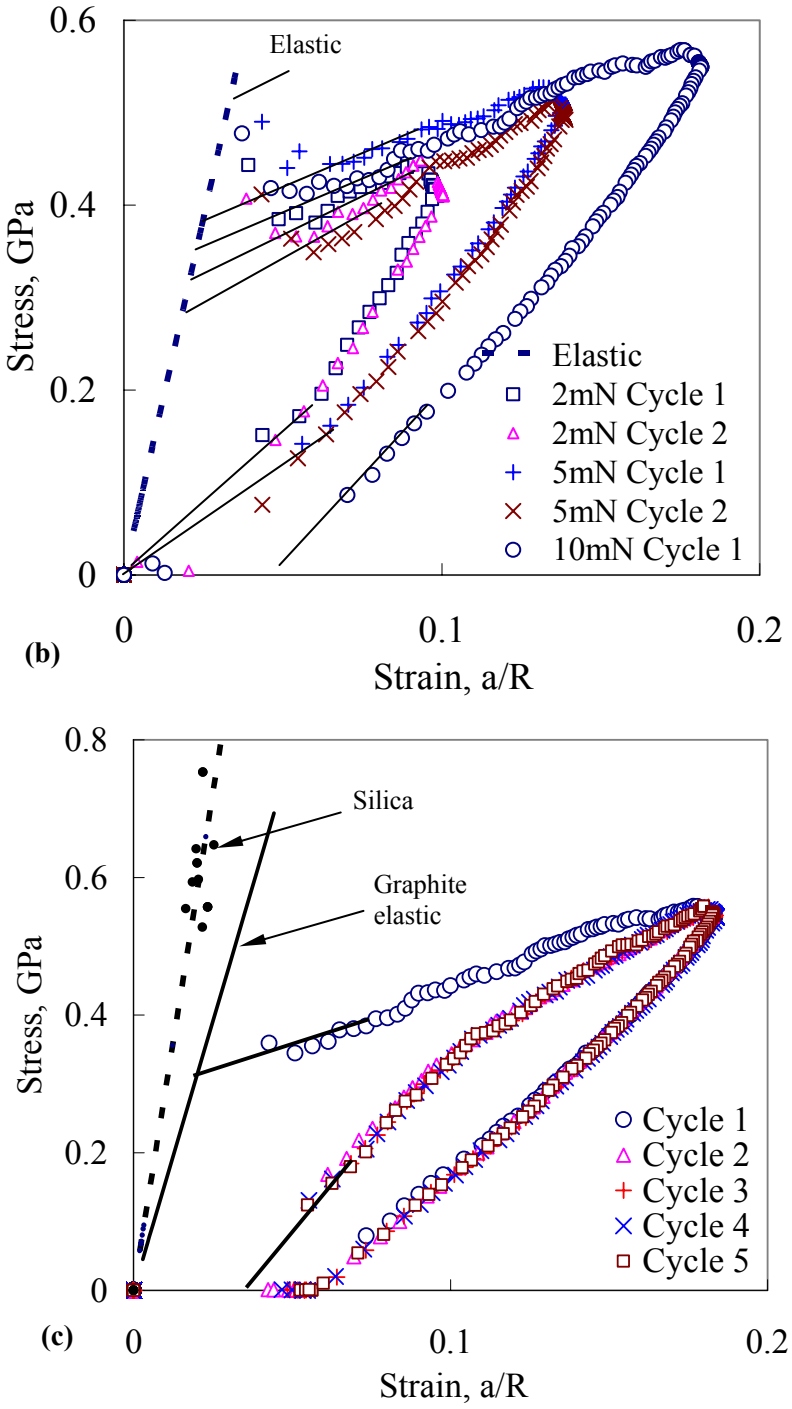

Figure 22: b) Stress vs. strain curves obtained from results shown in a. Low load indentations show full reversibility, but at 10 mN, the first loop is open. c) Stress vs. strain curves for cyclic loading at 10 mN. First cycle in open; subsequent indents are fully reversible and repeatable with a reproducibility that is noteworthy.

In contrast, a linear elastic regime was observed in most of the indentations in Ti_3SiC_2 as discussed in chapter 3 [46], where the stresses were roughly an order of magnitude higher.

Typical load-displacement curves generated with the spherical indenter applied along the 0001 direction (i.e. normal to the basal planes as shown in sketch in bottom right in Fig. 22a) are shown in Figs. 22a and 23a. The data at 2 mN, 5 mN and 10 mN shown in Fig. 22 were obtained from different locations; the results at 10 mN shown in Figs. 22b and 22c were obtained from the same location. At 5 mN or lower, the load-displacement plots resulted in what appeared to be fully reversible closed hysteresis loops - in a clockwise direction (Fig. 22a). Note that under the same conditions the response of SiO_2 is linear elastic with no hysteresis (Fig. 22a). Repeated loadings on the same location at loads < 5 mN resulted in excellent cycle-to-cycle reproducibility, with *no* hardening observed (see below). As the load is increased from 5 to 10 mN, a softening is observed at about 6 mN (Fig. 22a). Subsequent loadings to 10 mN, however, result in loops that are not only fully reversible, but always show a *higher* hardness than the first cycle. Subsequent loading to the same maximal load, however, did *not* result in further hardening (Figs. 22a and c).

All these observations are further confirmed when the same data are converted to stress/strain curves (Figs. 22b and c). Figure 22c plots the stress/strain curves obtained from another location that was loaded five times to 10 mN. An examination of Figs. 22b and c clearly establish that:

i) Initially the response is presumed to be linear elastic with a modulus assumed to be 36.5 GPa (Fig. 4c). As noted above, the stress-strain curves could not be extracted

reliably at low strain levels. When the loads were high the modulus could be extracted reliably from the initial portions of the unloading stress-strain curves (e.g. Fig. 23b).

ii) Yielding occurs at a stress level between 0.30 and 0.4 GPa (Fig. 23c). Beyond the yield point hardening occurs with a rate that is linear with strain.

iii) Repeated loadings at 2 and 5 mN, result in fully *reversible* and *reproducible* hysteresis loops with *no* hardening (Fig. 22b and c).

iv) At ~ 0.55 GPa, softening is noted and the resulting loop - labeled 10 mN cycle 1 in Figs. 22b and c - is open and results in a permanent strain of ~ 0.05. Further indentations to the same load at the same location results in f*ully reversible and reproducible* loops (Fig. 22c). As important the areas enclosed by he second and subsequent loops are less than the first signifying hardening. The majority of the hardening occurs between the first and second loadings, however (Fig.22c and 23b).

Typical load-depth of penetration curves for multiple loadings on the same location to loads of 200 mN are shown in Fig. 23a. Here again, the first cycle is open but the second and subsequent ones are harder and reproducible. The corresponding stress-strain curves (Fig. 23b) confirm that while the first loop is the largest in area, and thus the softest, subsequent loadings result in loops that are almost fully reversible.

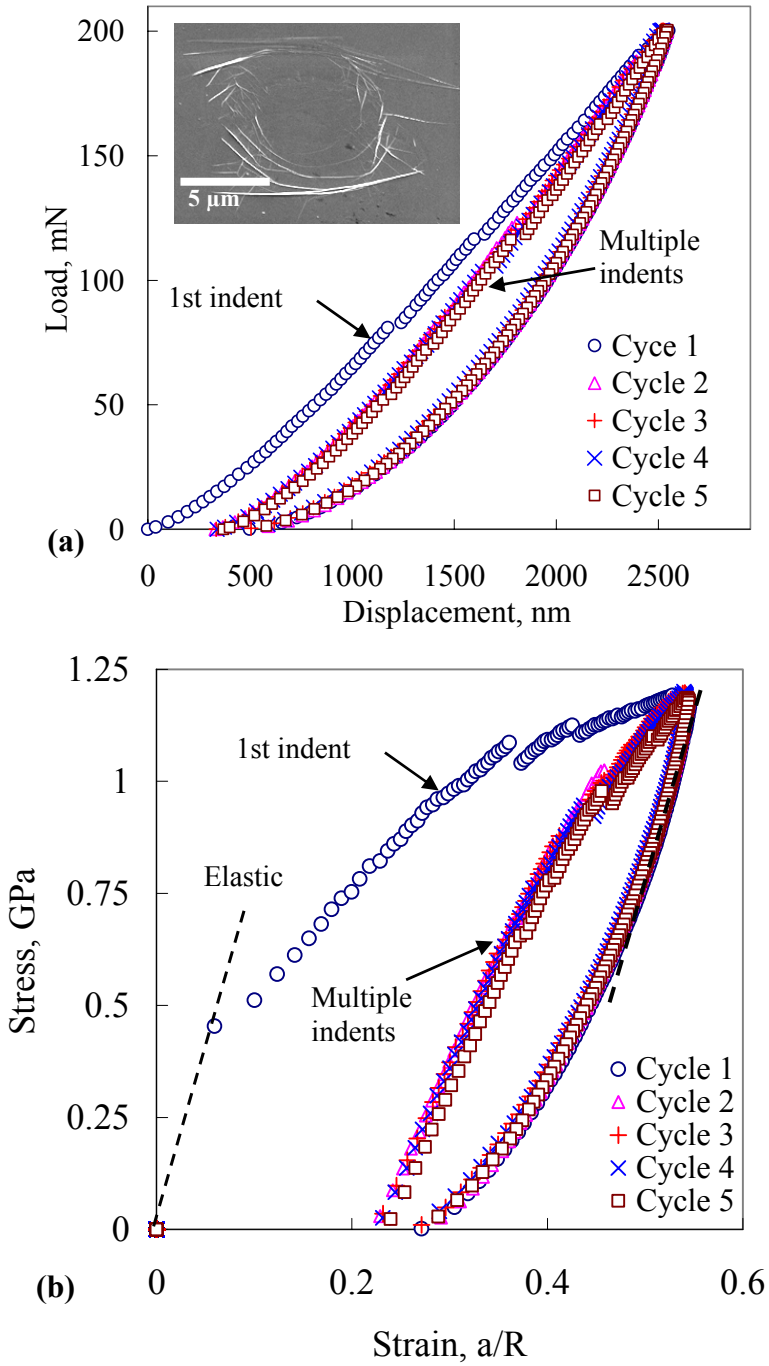

Figure 23: a) Load vs. depth-of- indentation response of graphite single crystals loaded along the 0001 direction to 200 mN. The first indent results in an open loop but subsequent indents are harder and their loops encompass a smaller area. Inset shows SEM micrograph of indented area. b) Stress/strain curves for results shown in a. The first loop is open, but subsequent loops are almost fully reversible. A dotted straight line drawn during initial unloading corresponds very well to the elastic loading slope.

The response of surfaces loaded to 400 mN is shown in Fig. 24a. The first cycle did not result in damage; the second resulted in a pop-in of the order of 60 μm. The third loading on the same location resulted in a two-regime response separated from each other by a prominent bend labeled B in Fig. 24a. Initially, the indenter easily penetrates the surface; at ~ 55 μm, the surface hardens dramatically. It is important to note that with the exception of the first cycle shown in Fig. 24a, all other indentations made at 400 mN resulted in massive pop-ins. Many of the ones at 200 mN also resulted in small pop-ins (Fig 23). Under a Berkovich indenter pop-ins were observed at loads as low as 5 mN (Fig. 24b). Only at the lowest loads (~ 2 mN) were closed hysteresis loops observed (inset in Fig. 24b).

Typical stress-strain curves obtained on macroscopic polycrystalline specimens are shown in Fig. 24 [Adapted from ref. 37 – Tiejun Zhen, Dissertation, Drexel University, Philadelphia, 2004]. Figure 24a shows four successive loops, each to a higher stress level. As in Ti_3SiC_2 [22], there is one loading curve and the hysteresis loops appear to be fully reversible. When loaded to a stress of 80 MPa, however, the first loop is open, but subsequent cycles to the same stress level are fully reversible, with a reproducibility that is noteworthy (Fig. 24b). The areas encompassed by the hysteresis loops in the stress-strain curves are a measure of the energy dissipated during each cycle, W_d. A log-log plot of W_d versus stress, s, is shown in Fig. 16. The excellent agreement between the values of W_d measured on bulk samples and those from nanoindentation experiments is gratifying.

Note that a simple energy analysis predicts a theoretical slope of ~ 2 [46]. A least squares fit of the graphite data in Fig. 16 yields a slope of 1.96 with an R^2 value of > 0.99.

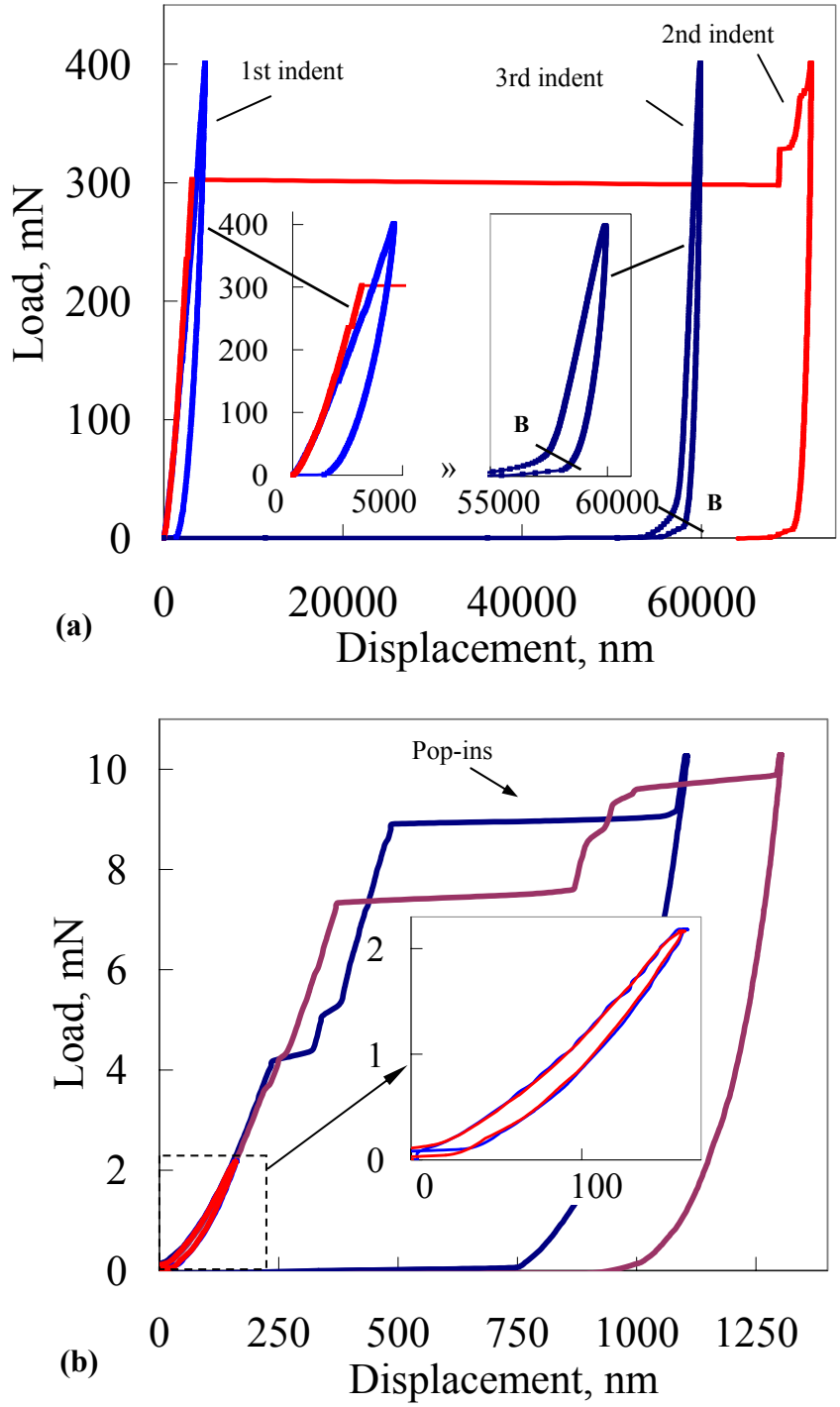

Figure 24: Cyclic loading to 400 mN three times. Massive pop- in observed during second loading. Note hardening subsequent to the pop-in. Third loading is characterized by a bend at ˜ 55 µm. Inset shows details of first and third indentations. b) Nanoindentation with Berkovich indenter: Extensive “pop-ins” or discontinuities resulted in damage even at small loads. Inset magnifies the indentations up to 2 mN. Note fully reversible nature of the loops.

Typical secondary FESEM micrographs of indentations made at 400 mN are shown in Fig. 25. The indentation locations appear as deep craters surrounded by defoliated graphene sheets (Fig. 25a and b). The center of the craters is comprised of a multitude of micron and submicron grains of random orientations (Fig. 25c). The number of cracks per unit volume is quite high and the porosity considerable (Fig. 25a and c). Evidence for kink boundaries (Fig. 25d) and the massive rotation of the lattice planes is unambiguous and ubiquitous. Interestingly, the symmetry of the indentations made with spherical indenters is 6-fold (see white dotted hexagon in Fig. 25a). This behavior is typical for spherical indentions of single crystals and has been also observed for Si, GaAs and other materials [26].

4.4 Discussion

Qualitatively the results obtained herein are very similar to those obtained on Ti_3SiC_2 (chapter 3) [22] and can be explained by our kinking-based model. As noted above, in this model there are three interrelated features that appear sequentially as the stress is increased: incipient kink bands, IKB's; mobile dislocation walls, MDW, that, in turn, coalesce to form irreversible or regular KB's.

Based on the results shown in Figs. 22b, c and 23b it is reasonable to conclude that the first IKB's are formed at a stress of ~ 0.3–0.35 GPa. Assuming the maximum shear stress under the indenter is ~ 1/2 the normal contact stress, it follows that the shear stress needed to create a dislocation pair in graphite is ~ 0.17 GPa; a value that is ~ G/30 of the true value of c_{44} [1]. This result confirms an important assumption of the Frank and Stroh model [42].

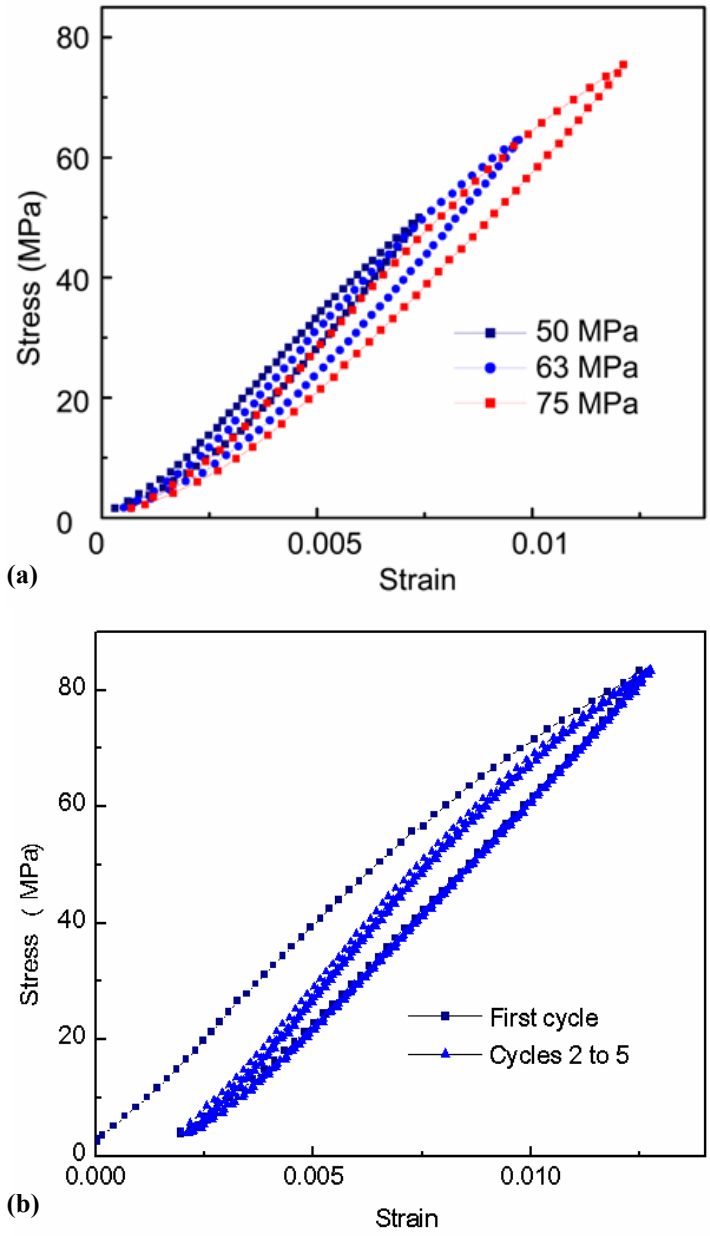

Figure 25: Compressive cyclic loading-unloading stress-strain curves of polycrystalline graphite at room temperature. a) Successively higher stresses from 36MPa up to 75MPa. b) Cyclic test at 83Mpa. In order to maintain sample alignment, the minimum stress in all tests was about 1–3 MPa.

The loops labeled 2 and 5 mN in Fig. 22b are fully reversible and do *not* result in hardening; two facts consistent with the formation of IKBs. The softening observed at ~ 0.55 GPa, must be related to the formation of MDWs. The permanent strain observed during the first loadings (e.g. Fig. 22c) is direct evidence for their formation. Since the IKB to MDW transformation cannot occur without delamination (see below) the stress at which the delamination of graphene sheets under highly constrained conditions occurs must be ~ 0.55 GPa. It is crucial to note that the delamination mechanism is inherent to KB's. Stroh [51] has shown that the tensile stresses at the tip of low angle grain boundaries or dislocation walls can result in delaminations. In this case, it is clear that as the IKB's get longer and penetrate deeper into the bulk, at some point the tensile stresses at their tip is sufficient to cause delamination ahead of them. Once delaminated, the IKB's become MDW's and result in irreversible deformations. It is interesting to note that hardening occurs despite the delaminations.

Once KB's are created, they reduce the effective volume (α in Eq. 1 in chapter 3), which in turn increases the stress needed for the formation of new IKB's, resulting in a hardening of the localized zone around the indent (Figs. 22a and b). Hardening is therefore the signature of the separation of the dislocation walls comprising the IKB's and their movement away from the areas of maximum shear and the formation of KB's (chapter 3) [22,46]. Repeated loadings to the same stress can now only initiate IKB's within the newly formed KB's. In other words, as long as the loads upon reloading are not higher than the initial load, a dynamic equilibrium microstructure develops.

In our previous work (chapter 3) we invoked the idea of an equilibrium microstructure, defined as one in which all dislocation motion was fully reversible, viz.

one in which all dislocations are associated with IKB's [44]. Experimentally such a microstructure is manifested by fully reversible hysteresis loops. Based on this definition, the 2 mN and 5 mN cycles in Fig. 22b, the second and higher cycles in Figs. 22c, all cycles shown in Fig. 25a and cycles 2 and higher in Fig. 25b represent equilibrium microstructures. In the bulk samples the evidence is unambiguous; by the second loading to 80 MPa, an equilibrium microstructure is established (Fig. 25b). Subsequent loadings only trigger IKB's.

Note that after an equilibrium microstructure is established and the stress level is increased anew, new MDWs that result in softening (e.g. decrease in slope in load displacement curve in Fig. 22a, above ~ 6-7 mN) and plastic strains will form. At loads between 50 and ~ 200 mN (Fig. 23a), small but multiple discontinuities or pop-ins are observed during loading resulting from damage or cracks around the indented locations. At 200 mN, most of the indents are visible and are characterized by Hertzian cone cracks typical of brittle materials (inset in Fig. 23a). This behavior is in agreement with other HOPG results reported in the literature [49].

The response of surfaces loaded to 400 mN (Fig. 24a) can also be interpreted by the formation of KB's. Based on the similarity in the response above the bend (region marked B in Fig. 24a) and most other load displacement curves shown in this paper, it is fair to conclude that the former is due to the formation of IKB's in the smaller volumes or subgrains (see below) formed during the first loading. To understand the origin of the response below the bend, refer to the schematic shown in Fig. 21, which is adapted from Refs. [9] and [35]. Figures 26a and b clearly show there is massive material transfer from below the indented zone to the sides of the indent. A simplified kink-band mechanism by

which such a transfer could occur is shown schematically in Fig. 21c. For the indenter to penetrate suddenly into the basal planes they must rupture (Figs. 26a and b). Since the rupture is associated with the pop-ins observed in Fig. 24a, it follows that the relatively large displacements at low stresses below the bend, B, are most probably related to the back and forth motion of delaminated and/or ruptured layers (Fig. 21c to e). Note that the sudden and massive - up to 60 μm - pop-ins could not have occurred without a rupturing of basal plane bonds. It thus appears that one consequence of the massive rupture of basal plane bonds is the bend or knee labeled B in the load-deflection curves (Fig. 24a). These pop-ins should not be confused with the much smaller pop-ins that have been related to the homogeneous nucleation of dislocations [52].

The micrograph shown in Fig. 26c presents *unambiguous* evidence for the formation of subgrains under the indenter. The presence of these subgrains was invoked to explain the hardening observed in Ti_3SiC_2, but direct evidence remained elusive [46]. Here the fragility of graphite relative to Ti_3SiC_2, results in clear and unambiguous evidence for the breakup of the single crystal into microdomains; a key feature of our model. The same microdomains have been observed in mica single crystals (chapter 5) [44]. It is important to emphasize that in all samples tested at loads of < 100 mN, no trace of the indents was found in the FESEM. Why the indents are not visible despite displacements of the order of 100 nm is an intriguing question for which the answer is not entirely clear. Two possible explanations are: i) the shallow dimples formed are hard to see in the FESEM and/or, ii) in the time between when the indents are introduced into the surfaces to the time they are examined in the FESEM, they fully or partially recover. It is also worth noting that no evidence for KB's was found by Raman spectroscopy (see below) either.

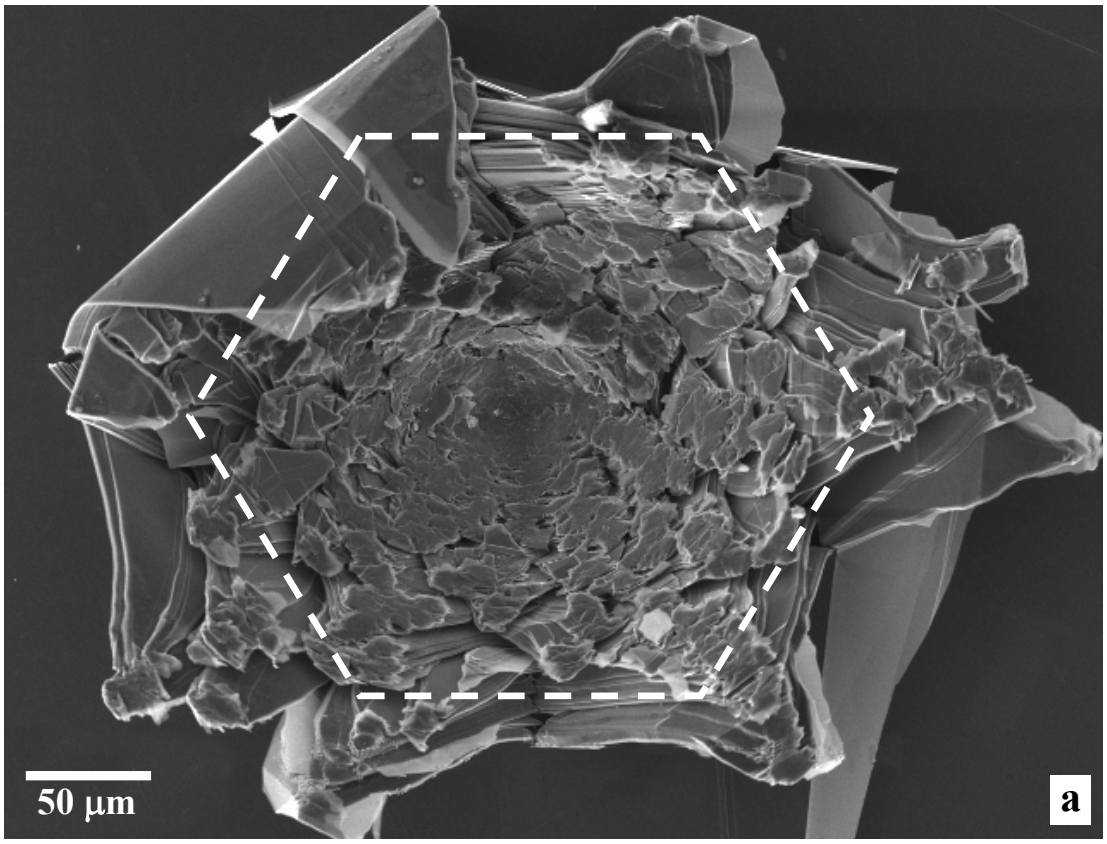

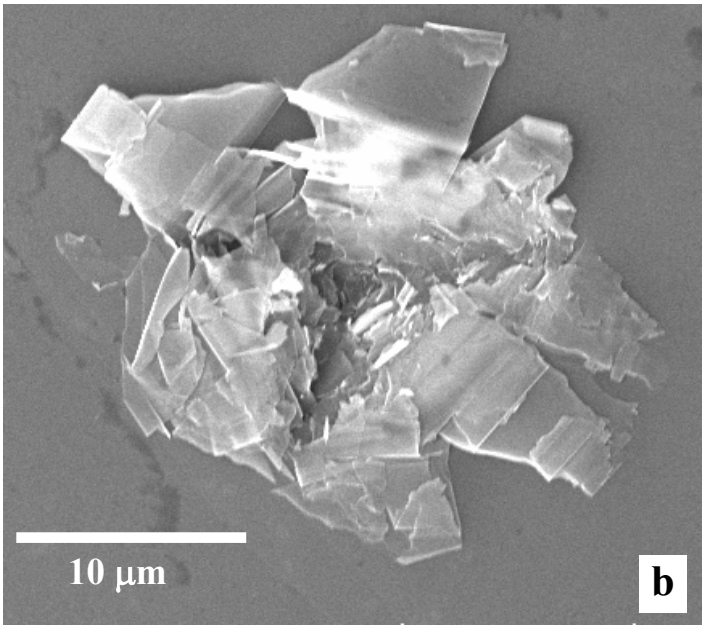

Figure 26: a and b) FESEM secondary micrographs of, a) spherical nanoindentation at 400 mN, the damage crater has a 6 fold symmetry (denoted by a dotted hexagon). b) Berkovich indentation at 10 mN.

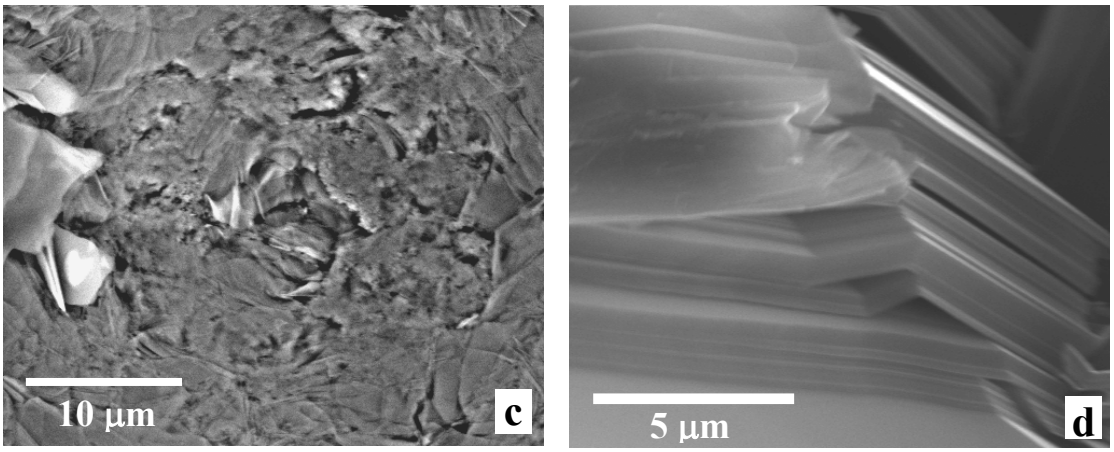

Figure 26: c and d) FESEM secondary micrographs at c) Higher magnification of a, focusing on core of the indentation. Note scale of subgrains; d) Higher magnification of a focusing on edge of the indentation crater clearly showing the formation of kink bands and delaminations. Note such features cannot be formed by any other process.

The extent of the damage under the indenter also appears to be larger than the size of the indentation. This was discovered from the following series of experiments. In an attempt to map out the effect of the indentations on the Raman spectra of graphite large 200 mN indentations spaced ~ 50 μm apart were introduced into the surface. These resulted in noticeable surface damage such as shown in inset of Fig. 23a. However, when 50 mN indents were introduced midpoint between the 200 mN indents the surface was completely damaged, forming a large crater, implying that the extent of damage sustained must extend farther than the cracks or craters would seem to indicate. In other words, the zone of influence or subsurface damage (dislocations, kinking or delamination) that results from a 200 mN indentation must extend at least one radius away from the center of that indentation.

4.4.1 Raman Spectroscopy

Raman spectroscopy is widely used to characterize not only carbon structures, but also the type of defects present [38,53]. Raman spectrum of graphite is characterized by a single peak at 1580 cm^{-1}, which is ascribed to in-plane vibrations (E_{2g2} modes) of the carbon atoms with respect to each other against a strong in-plane restoring force [54]. Lattice disorder, such as grain boundaries give rise to a disorder induced peak (D) around 1360 cm^{-1} and result in the broadening of the 1580 cm^{-1} peak. The broadening of the 1580 cm^{-1} peaks can also be caused by residual or local stresses. Furthermore, residual or local stresses can, and do, shift the 1580 cm^{-1} peaks, with higher wavenumbers indicating compressive stresses and lower values indicating tensile ones.

Given that the KB's are nothing but – depending on the magnitude of the shear stress acting on the IKB's –low or high angle grain boundaries, we attempted to prove their existence by Raman spectroscopy of indented areas. Figure 27 shows a typical spectrum obtained from a clean, unaffected surface of graphite basal planes (red line in Fig. 27) and from a damaged region under the indenter (blue line) such as the one shown in inset in Fig. 23a

Raman mapping was performed on a set of spherical indents with maximum loads at 50 mN and 200 mN as shown in Fig. 28. The 200 mN indent was visible in the FESEM (inset Fig. 23a), but the 50mN indent was not detectable. The location of the 50 mN is marked with a red circle and cross hairs. The area of the Raman map is marked as a dashed rectangle in Fig. 28a. Mapping of full width at half maximum (FWHM) at 1580 cm^{-1} is shown in Fig. 27b. The map shows significant peak broadening at the 200 mN

indent location, suggesting disorder. The Raman spectra of locations under the 50 mN indent, however, were indistinguishable from those of the defect-free graphitic surface. Note there is also some peak broadening observed at the left corner of the mapped region, where there were some preexisting defects visible in the SEM such as bent and exposed edges of basal planes (Fig. 10a). Evidence for D-bands was observed for higher loads such as 200 mN (see Figs. 27 and 28c), but not at 50 mN.

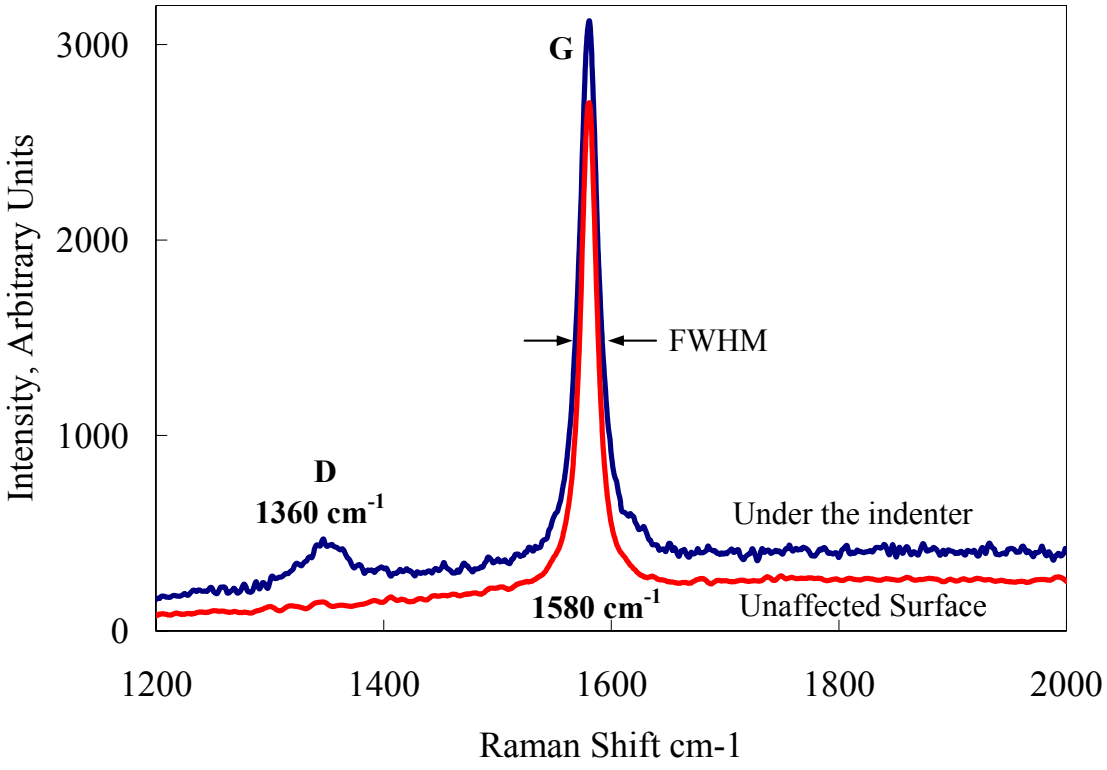

Figure 27: Comparison of the Raman spectra obtained from a pristine area (red), and one subjected to a 200 mN spherical indentation (blue). The D-bands at 1360 cm^{-1} are only observed at loads 200 mN or higher.

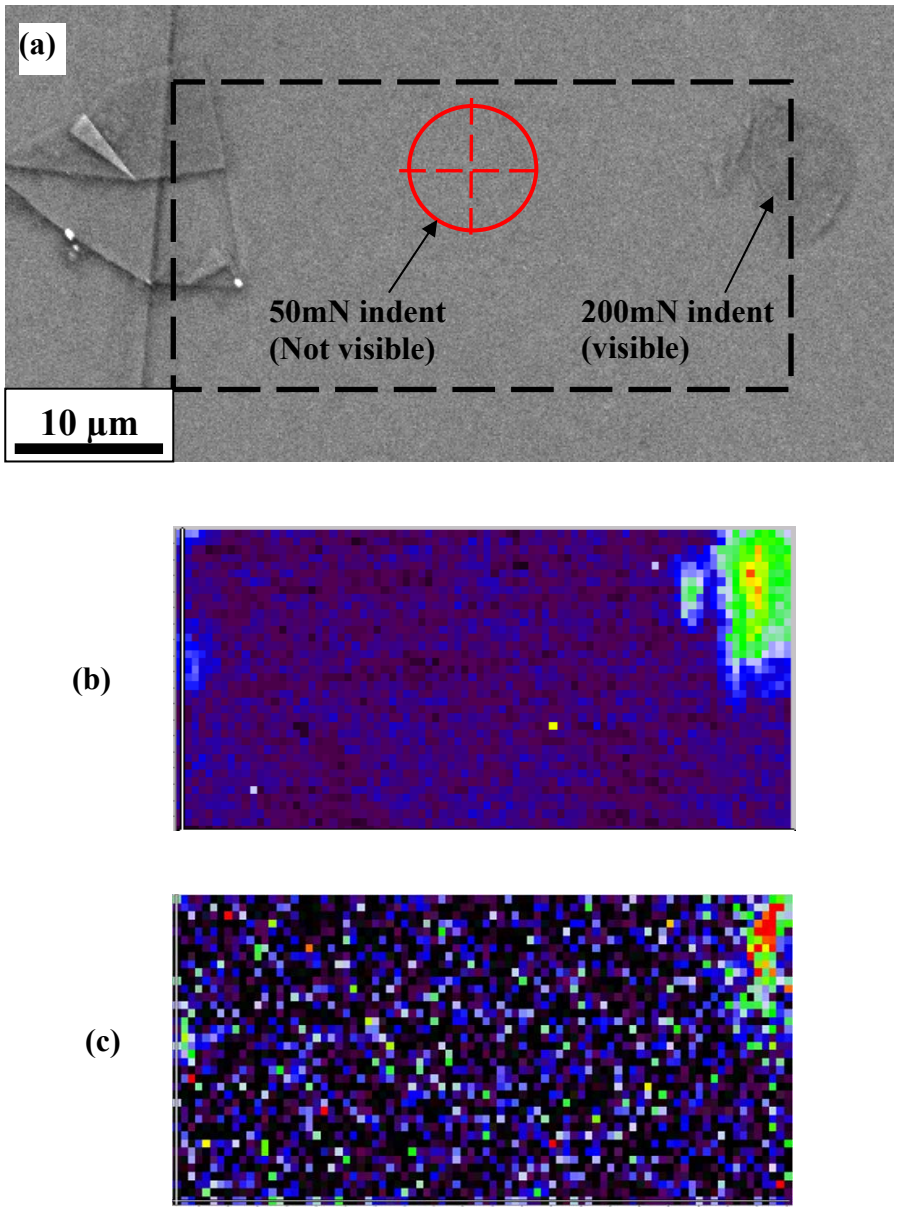

Figure 28: Raman mapping (dotted rectangle) of spherical nanoindents at 50 mN and 200 mN. a) FESEM micrograph of indented region. Region under the 200 mN indent is visible on the right; the 50 mN indent is invisible. The location of the latter is marked by red circle. b) Full widths at half max of G-band, and c) Intensity of D-band. Note absence of broadening of G-band at the 50 mN indent location and the absence of the D-band in the 50 mN location but their presence under the location of the 200 mN indentation.

The reasons no changes in the Raman spectra at the locations of the 50 mN indentations were observed are not clear at this time and more work is needed to better understand the relationship between KBs and Raman spectra. These comments notwithstanding, there is little doubt that KB's form beneath the indentations (Fig. 27d). Direct TEM evidence for dislocation-based kink bands in Ti_3SiC_2 under Berkovich indentations has recently been published [9,35], and there is no reason to believe the situation in graphite is any different.

4.4.2 Relationship to Previous Work on Graphite and Ti_3SiC_2

Fully reversible nanoindentation hysteretic loops have been observed in glassy carbons with nanometer sized grains [4] and CDCs [48]. In the case of glassy carbons, such a response is also observed with sharp indenters such as cube corner indenters. The reversible nature of the indents was explained in terms of the *reversible* slip of graphene planes in the nanometer grains [2] and the hysteresis was attributed to sliding friction between the layers due to compressive stresses [3,4]. More recently, it has been suggested that dislocation pileups may be responsible [2]. Interestingly enough, pileups were our initial explanation for the results obtained on Ti_3SiC_2 [22]. That explanation was rejected, however, because it failed to account for the reversible nature of the deformation. The results of this work suggest the origin of the loops obtained in the porous carbons is the formation of IKB's and KB's. As noted in the introduction many aspects of the mechanical response of single and polycrystalline graphite that to date have resisted explanation, can be explained by invoking our model. It is important to note that while KB's have been reported in graphite [1], they have rarely been invoked to explain its

response to stress. For example, neither Kelly [1] nor, more recently, Rand [55] refer to KB's when discussing the mechanical properties of graphite. The following list considers a number of observations that are well established in the graphite literature and that can be readily explained by invoking the formation of IKB's and KB's.

a. Typical cyclic compressive stress/strain curves for graphite [1] are identical to those shown in Fig. 25, wherein at low stresses, fully reversible loops are traced. At higher stresses, the first cycle is open, but subsequent cycles to the same stress are closed and encompass a smaller area [Fig. 25b]. These observations have been related to the presence of glissile dislocations [1]. Needless to say, the presence of glissile dislocations alone cannot explain the full reversibility of the process; IKB's can [22,46].

b. Transmission electron microscopy, TEM, of heavily deformed single crystals of graphite [1] have numerous tilt boundaries in which individuals dislocations cannot be resolved. Like in Ti_3SiC_2 [9,19,20,35,56], these boundaries result in severe lattice rotation. In this work the lattice rotations are evident in the SEM micrographs shown in Figs. 26.

c. The loss factors or damping in graphite are large compared to metals. This has been explained by invoking the dominance of shear processes and the presence of very high densities of glissile dislocations [1]. Here again, the presence of dislocations *per se* does not lead to large damping, if for e.g. these dislocations *entangle* as in the case for metals. A more plausible explanation is the one we propose, viz. the relatively large distances over which the basal plane dislocations can travel unhindered.

d. When the results shown in Fig. 18 are normalized by the appropriate elastic constants (36.5 GPa for graphite and 325 GPa for $Ti_3SiC_{2)}$ they fall on a universal curve (Fig. 18b). The results for mica also fall on the same curve, providing compelling evidence hat the underlying atomic mechanisms for all three solids are identical. The excellent agreement – over ~ 5 orders of magnitude in W_d - between the extrapolation of results obtained on bulk samples and those obtained from the nanoindentation stress/strain curves is noteworthy and gratifying. The agreement is even more remarkable when the differences in the definitions of stress and strain between the uniaxial case and those extracted from the nanoindentations experiments are considered.

e. In sharp contradistinction to metals, the energy dissipated or damping capacity *increases* as σ^2 (Fig. 18). This observation alone is impossible to reconcile with the mere presence of dislocations, if the latter are allowed to entangle.

f. Like graphite, the compressive strength of Ti_3SiC_2 is generally 3-4 times greater than its tensile strength. In both cases, in tension, the fractured surfaces are rough, but the average direction is perpendicular to the stress. In compression the fracture occurs at ~ 35-45° to the stress direction [1,8]. The same has been observed in all layered ternary carbide and nitride phases tested in compression and tension to date [8].

g. Like Ti_3SiC_2 [14], the fracture toughness values of fine-grained graphite are smaller than coarse-grained samples. In Ti_3SiC_2 the enhanced fracture toughness is a result of kinking and delaminations of grains that are large enough to bridge

the fracture plane. The former are stronger, however, than the latter as observed in graphite.

h. A long-standing mystery in the deformation of graphite has been the fact that when the sample dimensions are of the order of the microstructural features the compressive strengths decrease with decreasing sample size. Several explanations have been proposed [see references in Ref. 1]. The formation IKB and KB can easily explain these observations. The "yield" or deformation stresses in Ti_3SiC_2 are a strong function of constraining stresses; increasing the latter greatly enhance the former [46]. It is thus not unreasonable to conclude that the same occurs in graphite. This rationale is consistent with the observation that radial confining pressures increase the compressive strengths of some graphites [57]. The results of this work, however, are probably the most compelling demonstration of this fact; the stresses sustained under the indenter are, in some cases, of the order of 1 GPa; a value that is about an order of magnitude higher than typical compressive strengths of polycrystalline graphites that range from 30 to 100 MPa.

Since the nanoindentation experiments were carried out on a single crystal, the volumes probed were, more likely than not, perfect; a conclusion consistent with the fact that the yield point is ~ G/30. In the bulk samples, on the other hand, a multitude of grains are probed and the nucleation of the kink bands – a process that is currently not understood – occurs stochastically and over a distribution of stresses. Note that in all cases the local shear stresses needed to from a dislocation pair must be of the order of G/30.

i. Pure elastic deformation in polycrystalline Ti_3SiC_2 samples is only observed at very early stages of deformation when the applied stress is not sufficient to induce the formation of IKB's or when the domain size is sufficiently reduced. This leads to a strong dependence of the slopes and shapes of the stress-strain curves on grain size and applied stress and loading history [22]; the same is true for graphite [1,58].

   Similarly for graphite, c_{44} measured from stress-strain curves are always lower than those deduced from thermal measurements or theoretical calculations [1]. As noted above, to measure the 'true'– as determined from bonding considerations - values of c_{44} in graphite, the crystals have to be irradiated to the point that preclude dislocation motion [1].

j. A major distinction between graphite and Ti_3SiC_2, however, is in the magnitude of the effect; along the c-direction, graphite is about an order of magnitude less stiff. Furthermore, for any given stress, the areas within the load-displacement loops are greater than those for Ti_3SiC_2. For example, at all stresses, W_d is ~ 10 times greater for graphite than it is Ti_3SiC_2 (Fig. 25). As noted above, loads higher than 300 mN typically resulted in significant damage of the surface layers in the form of large 'craters' (Fig. 26a). Such cratering has never been observed in Ti_3SiC_2. The bonding in Ti_3SiC_2 is a combination of ionic, covalent and metallic [40,59] and as such the damage sustained, even when loaded *normal* to the basal planes is limited; delamination cracks propagate stably from the center of the

indent and are arrested after distances of the order of the indentation size, reflecting the higher fracture toughness of Ti_3SiC_2 in that direction [46].

This list is far from comprehensive and we are confident that more exhaustive analysis will show even more similarities. These similarities notwithstanding there are differences, some of them important. For example, porosity and microcracking probably play a bigger role in the deformation of polycrystalline graphites than in Ti_3SiC_2. We believe the insight gained herein will be useful in better understanding or reinterpreting the large body of literature dealing with the mechanical properties of graphite. Furthermore, the fact that graphite is a member of a much larger class of solids, kinking nonlinear elastic, KNE, solids - that includes the MAX phases, layered silicates, such as mica, and most probably ice and high Tc superconductors - also bodes well for rapid understanding of the mechanical properties of all of these materials, many of which have been studied extensively over the years. It now appears that solids with high c/a ratios - a sufficient but not necessary condition (chapter 5) [44] - will deform by kinking. Finally, the results of this work demonstrate the power of instrumented nanoindentation in general, and spherical indentations in particular, in furthering our understanding of the deformation mechanisms of KNE solids.

CHAPTER 5: KINKING NONLINEAR ELASTIC SOLIDS, NANOINDENTATIONS AND GEOLOGY

5.1 Introduction

In our previous work [44], we have shown that the mechanical response of mica, similar to the MAX phases (chapter 4) [46] and graphite (chapter 5) [43], are described by the formation of incipient kink bands (IKBs), mobile walls and kink bands (KBs), thus conclusively showing that the hysteretic mesoscopic units (HMUs) [60-62] are IKBs. The role of kink bands in micaceous solids and in geology [63-66] and the concept of the HMUs in the Preisach-Mayergoyz space (P-M space) model were elucidated earlier in chapter 1.

The domain-size dependence of the HMUs (L_o and L_c) of the P-M space model is inherent in the Frank and Stroh model (Eq. 1 in chapter 3), given by the domain size α. As shown in chapter 3, an IKB can only be triggered when $\tau > \tau_k$. The stress τ_k depends on the domain size α – the smaller α, the larger the stress required to nucleate an IKB. During unloading, due to lattice resistance to dislocation motion, the IKB is annihilated only below a stress $\tau < \tau_o$. The energy loss during each cycle is the back and forth motion of the dislocations – lattice friction to dislocation motion - comprising the IKBs. As in other layered solids, dislocations are mobile along the basal planes and do not cross slip and thus they do not entangle and/or work harden in the classic sense. These dislocations can move reversibly over relatively large distances and thus can dissipate substantial amounts of energy during each cycle. At sufficiently high stresses, the IKBs devolve into MDWs, a number of which can collapse together forming a KB. Formation of a KB

reduces the domain size available for the formation of an IKB, thus leading to hardening, a characteristic of these layered solids.

That KBs play a important role in the deformation of plastically anisotropic solids, such as Ti_3SiC_2 (chapter 3) [22,46] and graphite (chapter 4) [43] is now established. In graphite the bonds between the planes are van der Waals; in Ti_3SiC_2 they are a combination of metallic, covalent. This begged the question of whether KBs also play a role in ionically bonded solids such as mica. Herein we present nanoindentation evidence for the formation of IKBs and KBs in mica, and by extension other layered minerals. We also briefly discuss the far-reaching implications of these results for geology.

5.2 Experimental Details

Load cycle indentations were carried out on freshly cleaved mica surfaces to reveal atomically flat basal planes with a 13.5 μm radius spherical diamond tip as explained in chapter 2. The tests were carried out - under load control at loading rates between 0.5 mN/sec and 8 mN/sec – to peak loads of 10, 100, 200 and 500 mN parallel to the c-axis. To study the effect of cycling, typically multiple (mostly 5) indentations were carried out at the same location to any given load. The corrected or shifted load/displacement curves were then converted to stress/strain curves as explained in chapter 2.

5.3 Results

Fig. 29 shows typical load/depth-of-penetration curves obtained when a diamond spherical indenter of 13.5 μm radius is loaded to 100 mN parallel to the c-axis (normal to the basal planes) for the 3 grades of mica crystals. The load displacement curves clearly

show the difference between the quality of the micas: the higher the defect population, the softer the material and the larger the areas enclosed inside the loops. The responses of the 3 different grades of mica are discussed separately below, beginning with grade C:

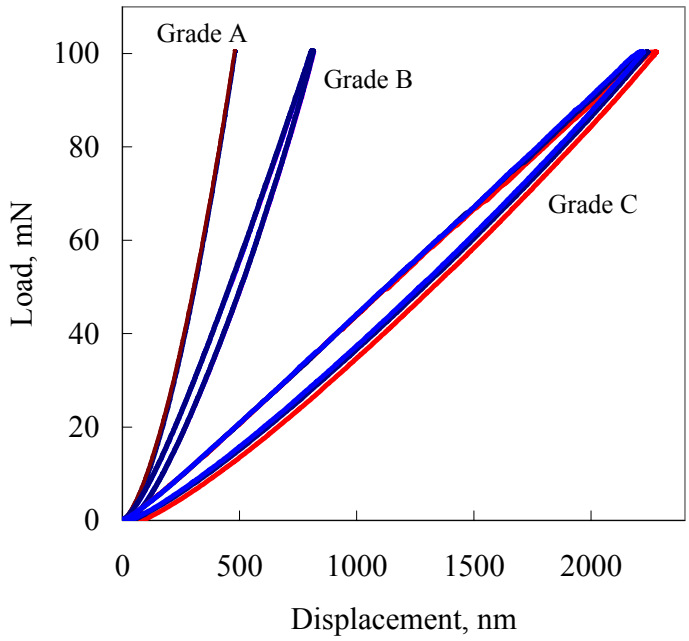

Figure 29: Load vs. depth of penetration for the 3 micas studied: Grade A, B and C, the difference between the qualities of the micas are evident from their load displacement. Higher population of defects results in larger hysteresis.

5.3.1 Grade C mica

When grade C mica was loaded, the hysteresis loops were significantly larger than the other grades and the response was much more stochastic (Fig. 30), with the load displacement response strongly dependent on the location of the indentation presumably due to defects in the form of either entrapped air bubbles and/or delaminations. Apart from cases where the load displacements resulted in significant pop-ins at higher loads or

in some cases such as the ones marked as "Y" in Fig 30 the load displacement showed typical hysteresis loops observed in other layered solids such as in Ti_3SiC_2 and graphite with good reproducibility between the first and subsequent cycles.

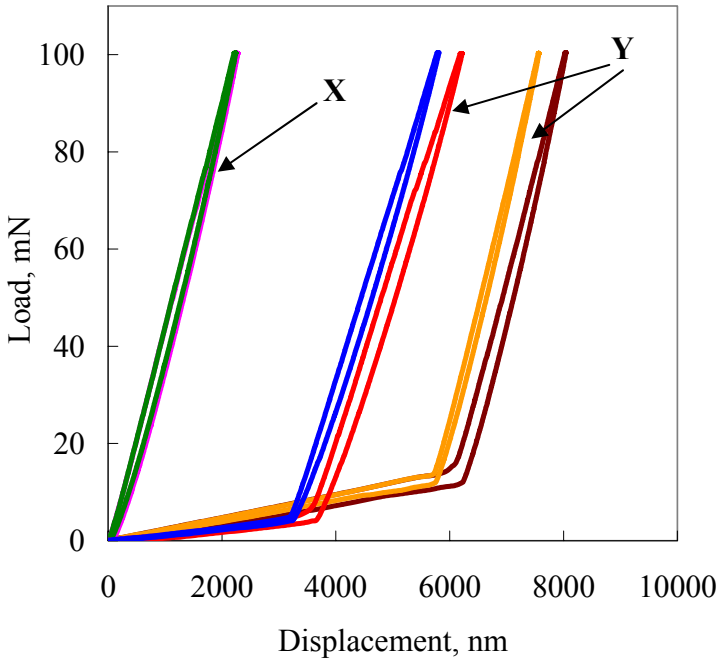

Figure 30: Variability and scatter in grade C mica. The load displacement response was strongly dependent on the location of the indentation. In case of no pop-ins at higher loads or in cases such as the ones marked as X above, the load displacement showed typical hysteresis loops and good reproducibility between the first and subsequent cycles. The loops marked as Y above are the same as shown in Fig. 1 for grade C mica.

The loops marked as X in Fig. 30 are the same as shown in Fig. 29 for grade C mica. The load displacement response and corresponding stress strain of this sample is shown in Fig. 31. There is very good cycle to cycle reproducibility with very little difference between the first and the subsequent loops, indicating lack of hardening. However, the nanoindentation stress-strain values for grade C mica could not be meaningfully

computed in contrast to the other grades. The equation for contact stresses and strains are based on Hertzian assumption of dense elastic bodies. Due to defects such as air pockets, delaminations etc…the sample cannot be thought of as fully dense elastic material and thus the stress and strain obtained for grade C seem to be inconsistent with what would be expected; this is evident from the stress and strain (Fig. 31b). The initial elastic slope is low compared to the theoretical modulus of 61GPa; the calculated modulus here is only about 20 GPa. From the curves, it is evident that grade C mica does not undergo strain hardening (as the slope after the apparent yield point is close to horizontal) at around 0.8 GPa. Typically the initial portions of the unloading slopes for most materials studied to date - including solids that show reversible hysteresis such as Ti_3SiC_2 and graphite, matched very well with the initial loading slopes [eg., Figs. 14b and 23a]. However, in this case the elastic slope during loading is 20GPa, but only 7 GPa during unloading, this implies that the mechanisms responsible for deformation during initial loading and initial unloading are different. It can be argued that during loading, the indenter presses against the layers that are not fully dense and the defects such as pores and delaminations affect the measured modulus (20 GPa vs. 61 GPa for fully dense mica [67]). While during initial unloading, the modulus values measured are even lower, thus more compliant than during loading. The exact mechanism responsible for such a response is not understood at this time.

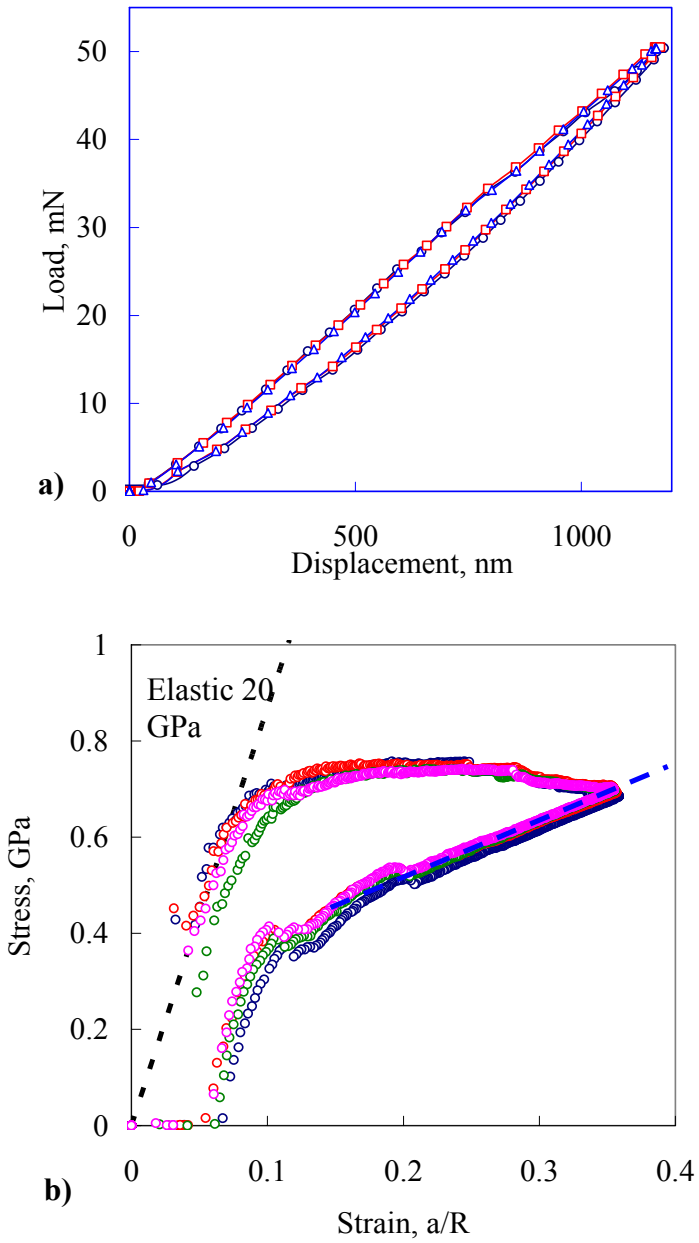

Figure 31: Load displacement response in grade C mica at 50mN. No hardening observed even after the first cycle in this case. b) Stress strain response of a). The initial loading modulus is only 20GPa as compared to 61 GPa for higher quality micas. Back extrapolated indentation yield point is around 0.7 to 0.8 GPa, after which the sample does *not* undergo strain hardening. Also the first and the subsequent loops are identical – no evidence for hardening observed

5.3.2 Grade B mica

In the case of grade B micas, the response was more reproducible. Fig. 32a plots successive indentations at 100mN in the *same* location. The load displacement was characterized by a series of hysteresis loops in which the first loop was slightly open, but subsequent loops became nearly closed - i.e. fully reversible - with cycling (Fig. 32b).

Furthermore, the areas encompassed by the loops decreased after the first indent, which is clear evidence for cyclic hardening. In Fig. 32a and b only the first, second and fifth, or last, cycles are plotted for the sake of clarity. The stress strain values are plotted in Fig. 33. Plotted on the same figure - as a dotted straight line - is the response of mica loaded normal to the basal planes assuming an elastic modulus along the c-axis of 61 GPa, obtained from *ab-initio* calculations [67].

Examination of Fig. 33 makes it is obvious that:

i) While the first loop is open, the second and subsequent loops are marginally so.

ii) Back extrapolating the data points of the first cycle until they intersect the line labeled elastic response in Fig. 33, indicates the material yields around 1.8 GPa. Note that the yield point is a strong function of the type and grade of mica used. Grade C micas with presumably larger numbers of defects - such as entrapped air, impurities, inclusions, etc., - tended to have significantly lower yield points and larger hysteresis loops

iii) Increasing the number of cycles results in loops that are near fully reversible, as evidenced by the shift of the unloading curves towards the origin (2^{nd} to the 5^{th} indents in Fig. 32 and 33).

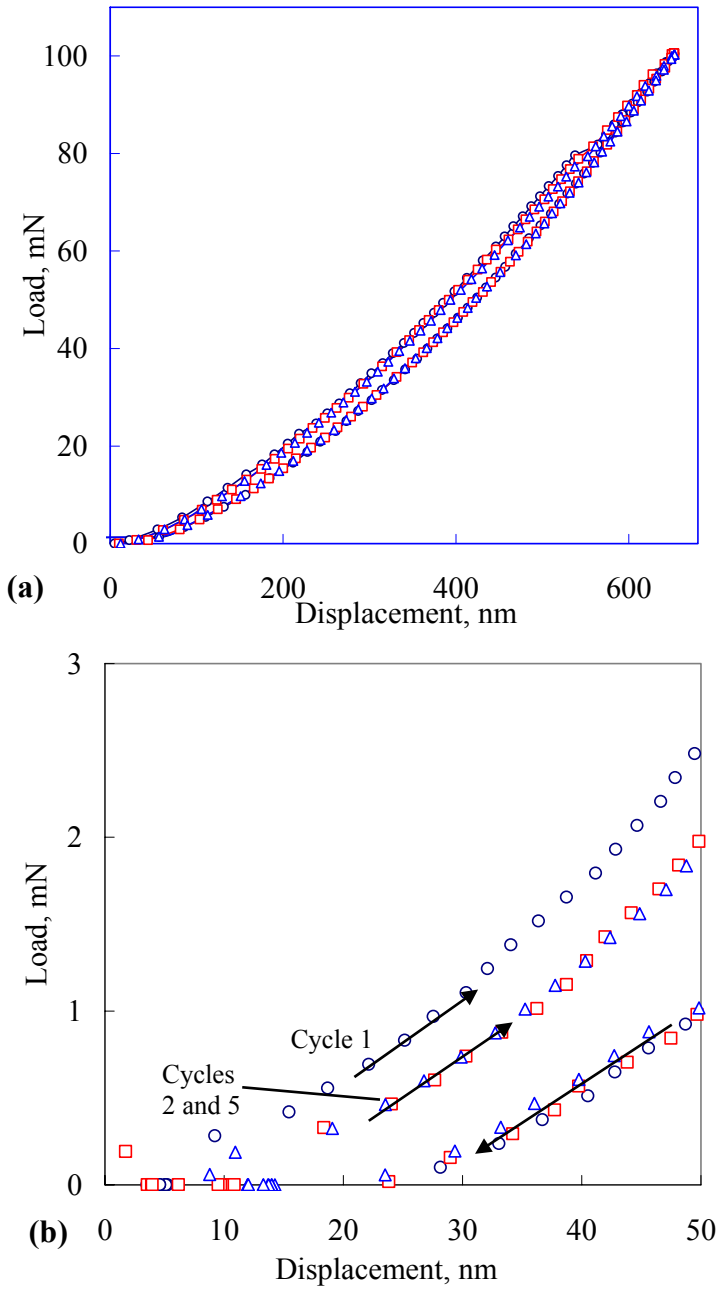

Figure 32: a) Typical load vs. depth-of-indentation curves obtained with a spherical diamond indenter, loaded several times in the same location. b) Magnified at low loads, showing repeatability of multiple indents.

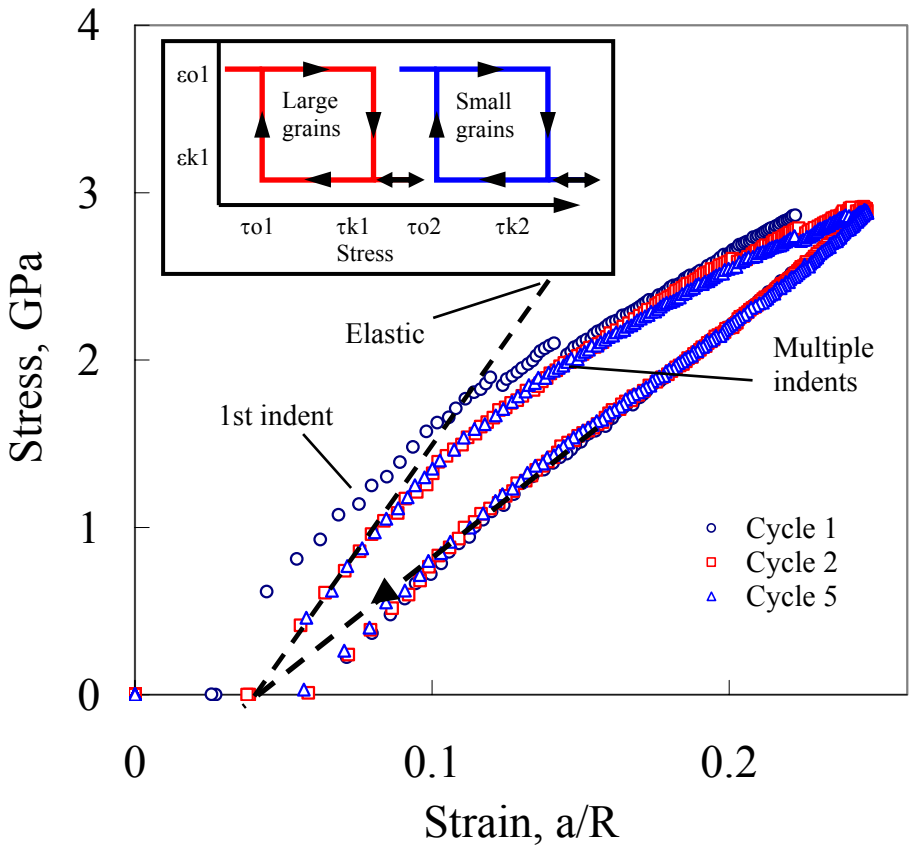

Figure 33: Corresponding stress/strain curves for data shown in a. In both cases only cycles 1, 2 and 5 are shown. During unloading, the dotted line represents extrapolation from the initial unloading slope that intersects the loading slope at the origin - indicating full reversibility. The deviation of the data points from the dotted line is most probably due to experimental artifact and noise. Inset is a schematic of how a microstructurally dependent, IKB-based, hysteretic element would behave on loading and unloading

Another dotted line is drawn in Fig. 33 during unloading extrapolating from the initial unloading slope that intersects the loading slope at the origin of the second and subsequent cycles - indicating full reversibility. As discussed in chapter 2, the deviation of stress at the end of the unloading cycles from the dotted straight line drawn in Fig. 33 is an artifact of the experiment; if such a deviation in each cycle is real then many such cycles would result in a large crater due to the accruement of these strains. In one case,

the tests were repeated 100 times and the indented region was studied under a FESEM and atomic force microscope (AFM). There was no trace of the indents indicating full reversibility and complete recovery, implying such a deviation is an experimental artifact.

Indentations to loads higher than 400 mN resulted in massive, very sudden and irreversible penetrations of the order of 2 μm (Fig 34). Subsequent indentations in the same location, once again resulted in loops that became harder and closed with cycling. In the absence of such massive pop-ins, and despite the fact that the Hertzian stresses at the tip of the indenter were of the order of 4 GPa for the higher loads, typically *no trace* of the indentations was found in the FESEM.

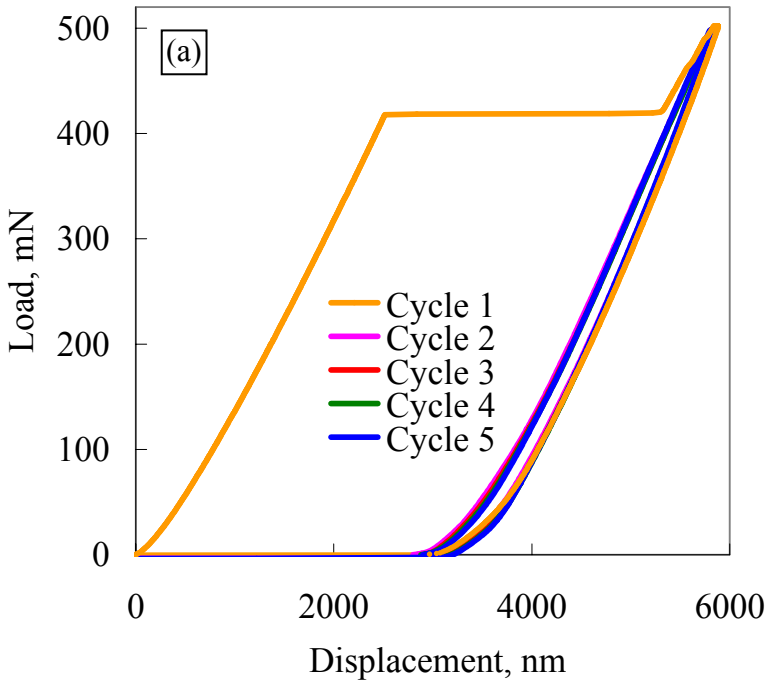

Figure 34: Loading to higher loads in many cases resulted in pop-ins. b) Load displacement curves showing pop-in during the first indent. Subsequent indents, however, were reproducible.

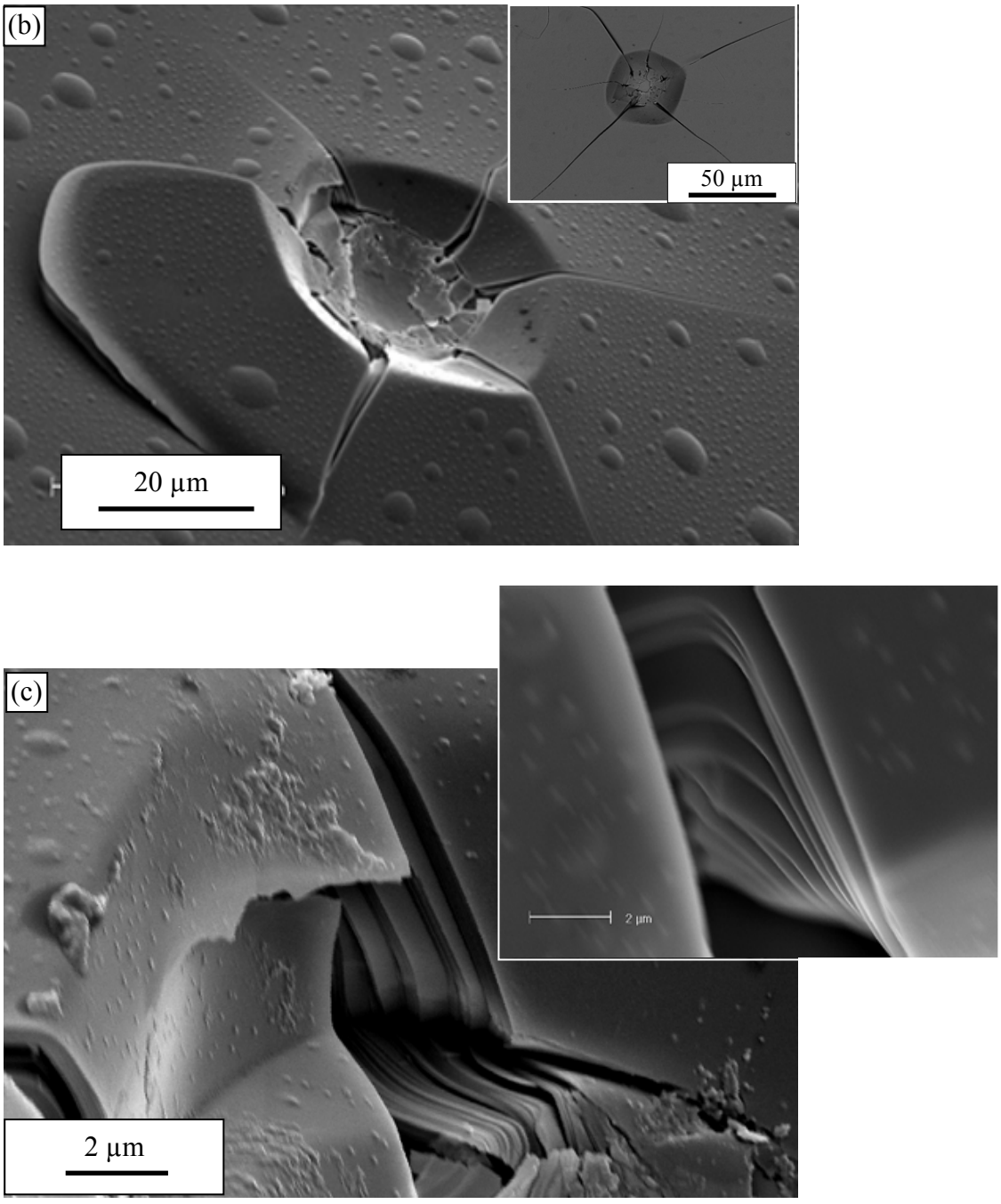

Figure 34: b) Field emission SEM micrographs of indents in mica after massive penetration of the indenter at low magnification showing indent and characteristic pileup around indentation, inset shows the breakup of the pristine sheets of mica into a multitude of smaller domains. c) Higher magnification showing kinks denoted by red arrows. Inset shows typical delaminations.

5.3.3 Grade A mica

Grade A micas, for the most part exhibited elastic response, though fully reversible hysteretic responses were also observed as discussed in depth below. At least four different load-displacement responses were observed in grade A mica:

1. Most of the indentations in grade A were linear elastic (Fig. 35a). When the results were converted to stress-strain (Fig. 35b), a distinct change in modulus at higher loads was observed (> 100mN, above around 4 GPa), the modulus value changes from 61 GPa to a higher value of about 67 GPa as the sample is subjected to higher stresses. This could possibly be due to collapse of any defects present in the sample under the indenter or could be due the response from the higher stiffness of the atomic bonds in the silicate layers of mica as compared to the response from the interlayer ionic bonding (i.e., of the potassium atoms between the layers). The response observed is repeatable and consistent in grade A micas.

2. In some cases the response was hysteretic and fully reversible at higher loads (100 to 200mN), with very small pop-ins during loading (Fig. 36c). The first, second and the fifth indents for load-displacement and stress-strain are shown in Fig 36b. In one case, the tests were repeated 30 times in one location, with no apparent difference in response between the first to the thirtieth indents.

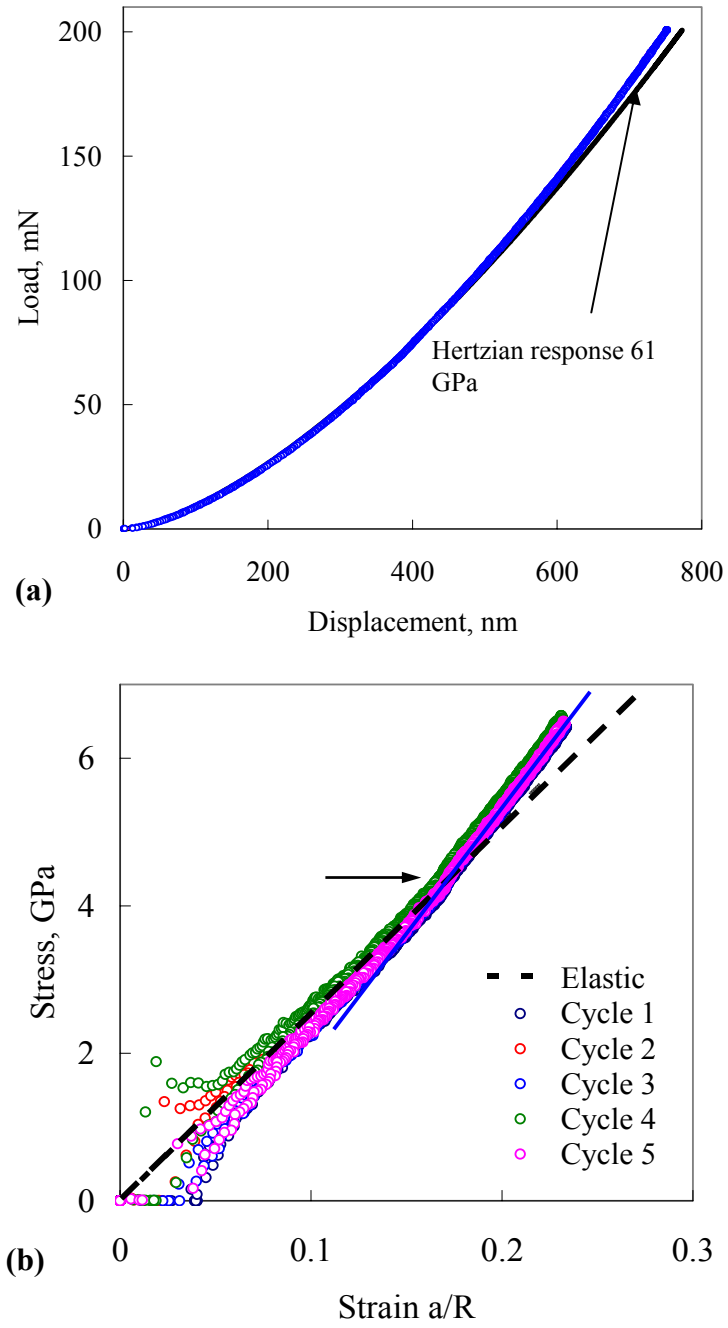

Figure 35: a) Typical load vs. depth of penetration for grade A mica at higher loads. A Hertzian response is also plotted (black line). b) Corresponding stress strain response, there is change in modulus value from 61 GPa to 67 GPa, at about 4 GPa in this case, denoted by the arrow

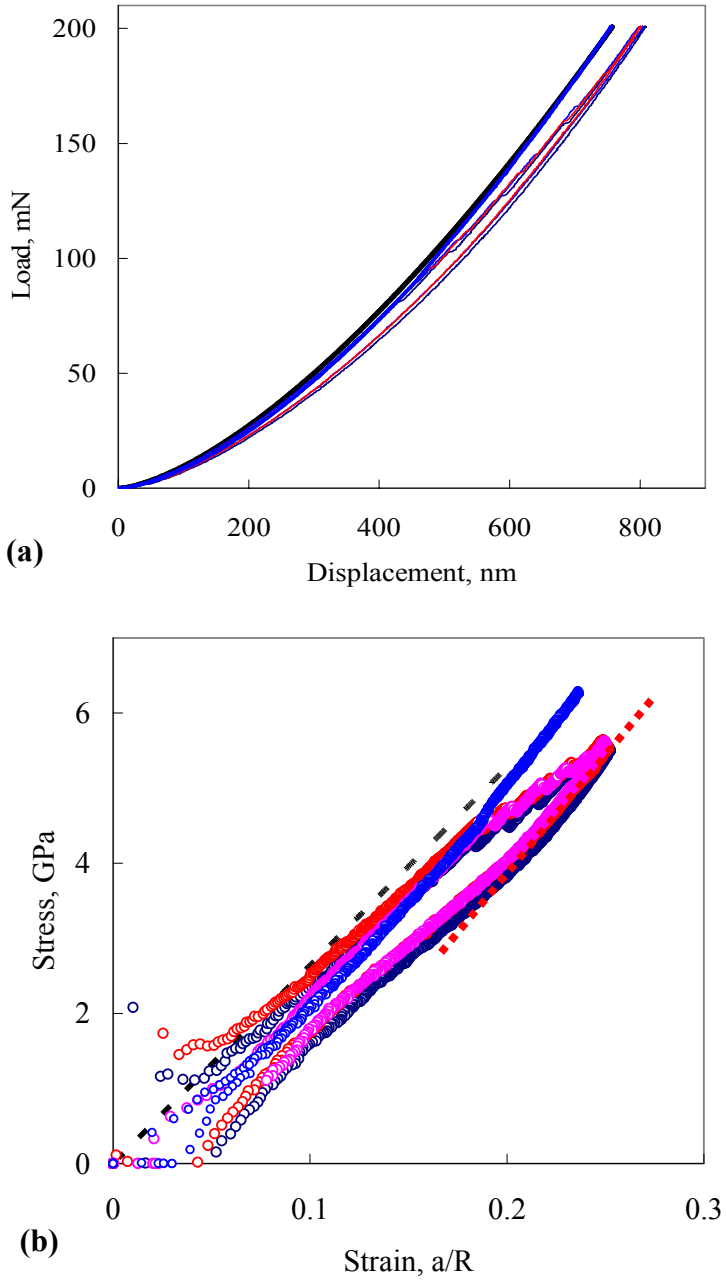

Figure 36: Hysteretic response observed in grade A micas – a) Load displacement at 200 mN - note full scale or reversibility in the load displacement loops. Also plotted (in blue) is elastic response observed in some locations, plotted here for comparison. b) Corresponding stress strain loops. The black dotted line during loading corresponds to a modulus of 61 GPa. The modulus value during unloading is 67 GPa (dotted red line), similar to what is observed as in cases of purely elastic response.

3. In other cases the response was hysteretic reversible with distinct pop-ins as shown in Fig 37a. However, and despite pop-ins of the order of 30 nm, the sample shows almost fully reversible hysteresis. Pop-ins usually result in permanent deformation, as evidenced in graphite, Ti_3SiC_2 and in some cases in mica as shown below. However, these pop-ins observed in grade A micas seem to heal after the load is removed as shown in Fig. 37a. The insets expands regions at low loads and at the pop-ins. The displacement due to pop-ins is ≈ 30nm, while the apparent residual displacement is only ≈ 18 nm. This implies that the sample recovers despite the pop-ins. It has been known that microcracks in ceramics can heal completely in conditions of high vacuum after the applied stress is removed, as the broken bonds can reattach as long as there is no source of contamination or impurities (such as oxygen) [68]. Such healing of mica has been observed during cleavage tests on mica under very high vacuum conditions (< 10-8 Nm^{-2}), where macroscopic cracks can be made to advance and retreat with little loss of energy through successive cycles [68]. In the case of these pop-ins observed to heal, the damage (or delamination) occurs at a certain stress under the surface of the sample, where the damage in contained and isolated within the sample. Thus the delaminated/damaged layers do not come in contact with any possible contamination and thus can and do heal almost fully. This behavior is observed even in repeated loadings and successive pop-ins are observed.

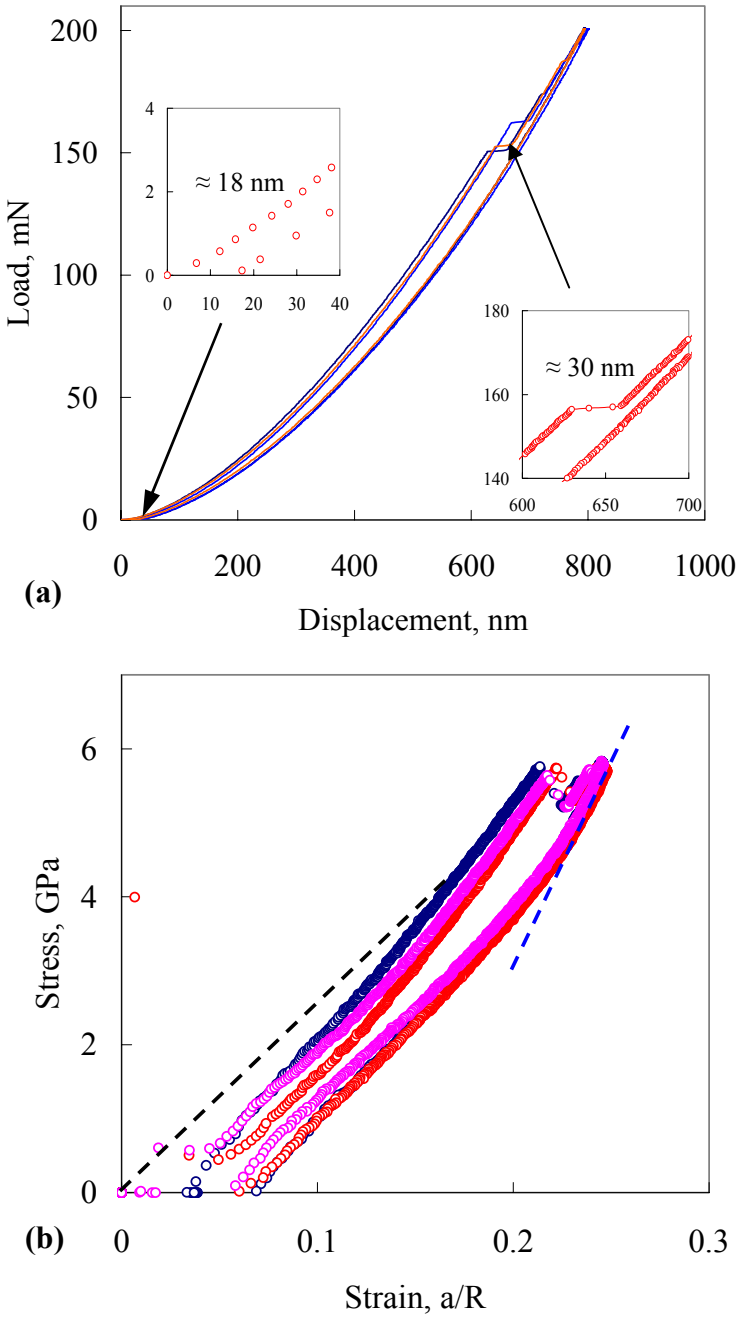

Figure 37: a) Load vs. displacement showing distinct pop-ins during loading. Further repeated loadings resulted in almost reversible hysteresis loops and repeatability of such pop-ins. The insets show the displacement due to pop-ins ≈ 30 nm and the apparent residual displacement ≈ 18 nm, which is less than the displacement due to pop-ins. This implies the sub-surface delaminations/cracks heal after the load is removed. b) Corresponding stress strain curves show a higher modulus during unloading despite the pop-ins. The loading modulus is 61 GPa (black dotted line) and the unloading modulus (blue dotted line) in this particular case was 120 GPa

4. In some cases, sudden and massive pop-ins were observed, resulting in permanent deformation at higher loads due to delamination/damage (500mN) with the mica layers exposed as a crater, as shown in Fig. 38, such massive pop-ins do not heal. It is crucial to note that *only* when loaded to the maximum load possible on our indenter (500 mN) and *only* in some cases did we observe the massive penetrations shown, however, subsequent indentations in the same location, once again resulted in loops that became progressively harder and less open with cycling. In the absence of such massive pop-ins, and despite the fact that the Hertzian stresses at the tip of the indenter were of the order of 5 GPa or more, typically *no trace* of the indentations was found in the FESEM or in AFM. This prompts us to suggest that despite the purity of the samples, presence of defects such as inclusions are necessary to act as a nucleation sites in order for such massive pop-ins to occur.

5.3.4 Compression tests

Compressive tests were carried out on a mica-containing glass-ceramic - Maycor™ (Ceramic Products Inc, Palisades Park, NJ) cylinders (12.7 mm in diameter; 31mm long) for comparison. Testing was carried out on a MTS 810 testing machine in load-control mode. The loading and unloading rate were 3kN/second; the strain was measured using a MTS axial extensometer (25mm gauge length) attached directly to the sample. The stress strain exhibited fully closed hysteresis loops [Adapted from ref. 37 - Tiejun Zhen, Dissertation, Drexel University, Philadelphia, PA – 19104, 2004] (Fig. 39).

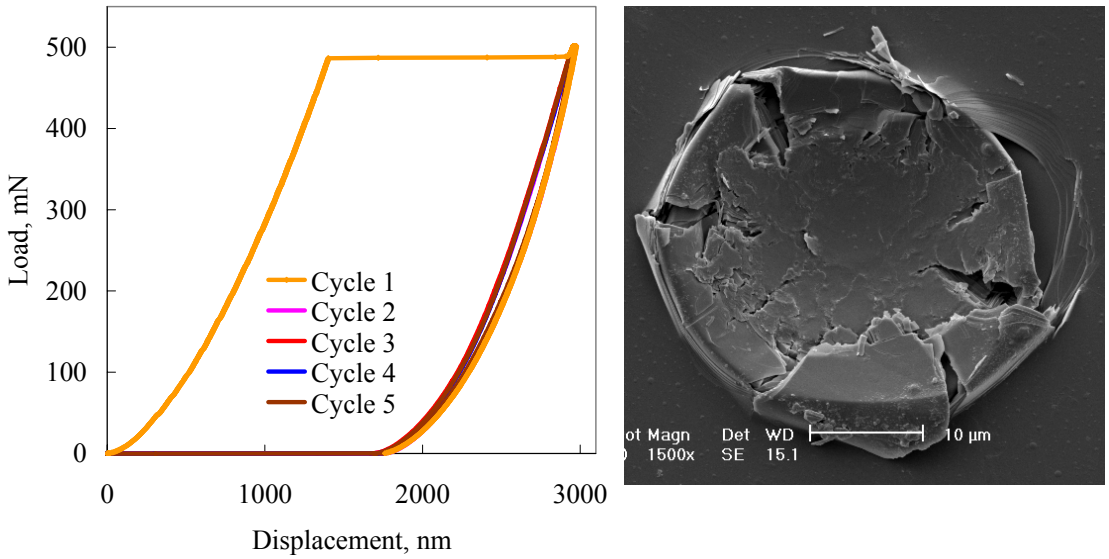

Figure 38: a) Sudden and massive pop-ins at higher loads (500mN) in grade A micas - similar to those observed in grade B at high loads, resulting in permanent deformation. b) due to delamination/damage of the mica layers exposed as a crater. Multiple loading on the same location resulted in loops that were repeatable.

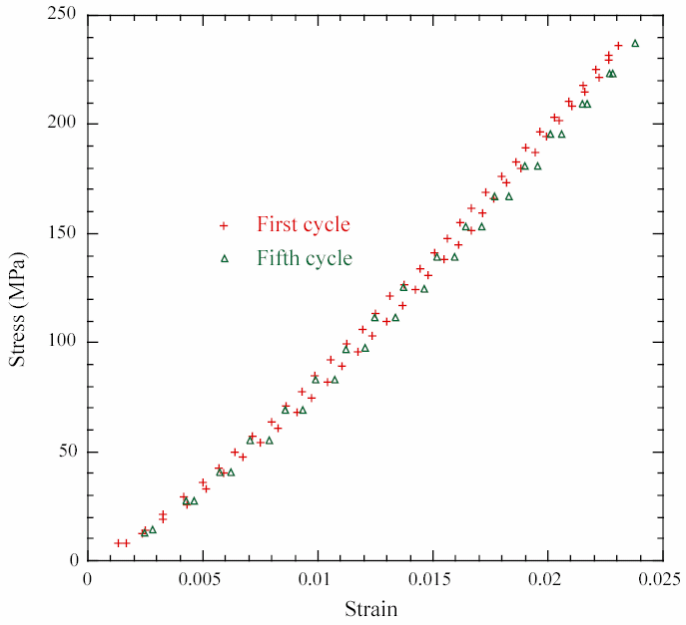

Figure 39: Stress-strain curves obtained by compressing Maycor™ (Ceramic Products Inc, Palisades Park, NJ) cylinders (12.7 mm in diameter; 31mm long). Testing was carried out on a MTS 810 testing machine in load-control mode. The loading and unloading rate were 3kN/second; the strain was measured using a MTS axial extensometer (25mm gauge length) attached directly to the sample.

5.4 Discussion

Similar to what was shown in our previous work [44], the reversibility and hardening in the indentation load-displacement response of mica, despite the observed pop-ins, comprised *all* the features observed in Ti_3SiC_2 and graphite (chapters 3, 4) [43,46]. It is remarkable that the response observed is similar despite the differences in the nature of bonding in these layered solids - a combination of metallic, ionic and covalent in Ti_3SiC_2, van der Walls in graphite and weak ionic bonding in the case of mica. One feature that is common for all these solids is their layered nature. Most of these solids are also characterized by high c/a ratios (such as in Ti_3SiC_2, graphite and mica). Twinning is generally precluded if c/a ratio is > 2, owing to energy considerations for a twin to form, particularly non basal twins, thus kinking is the preferred mode of non elastic deformation in these solids. Evidence for kink bands under the indenter were published recently [44] and is shown in Fig. 34.

A log-log plot of W_d vs. σ is shown Fig. 18a for grade B micas. Also plotted are the corresponding values for Ti_3SiC_2 and graphite, obtained from bulk [22] and nanoindentation experiments (chapters 3, 4) [43,46] similar to the ones shown here.

The W_d values for the bulk mica-containing glass-ceramics tested in simple compression fall in between those of Ti_3SiC_2 and graphite (Fig. 18a). These results cannot be directly compared to the nanoindentation ones, however because the bulk samples were not natural mica, but rather a synthetic glass-ceramic in which fluorphlogopite-based elongated grains are embedded in an amorphous matrix [69].

The hardening, the large areas encompassed by the loops and their *full reversibility* are totally consistent with our model. The reversibility is inherent to IKBs, as by definition, IKBs are fully reversible. At higher stresses the IKBs become mobile walls and collapse of these mobile walls to form permanent KBs, which is accompanied by hardening at higher loads. On further loading after the onset of the formation of KBs, the reproducibility and lack of hardening *in subsequent loading cycles* is in total in agreement with the model proposed. As noted above, the formation of KBs reduces α, which in turn increases the stress needed to initiate new IKBs. The very large energy dissipated per cycle is consistent with the fully reversible back and forth motion of dislocation loops comprising the IKBs. The confinement of dislocations to the basal planes [70,71] allows the dislocation loops to extend over relatively large distances resulting in large values of W_d (Fig. 18a). Note the glide of dislocations per se *cannot* explain this phenomenon if the dislocations are allowed to entangle in which case the process would not be reversible [70-72].

The large values of W_d imply that the areas swept by the dislocation lines must be huge, a conclusion reached by both Meike [70] and Kronenberg et al. [71]. The former directly observed basal dislocation motion in the TEM and reported dislocation separations – attributed to stacking faults - of the order of 100 to 500 nm. In the same paper, Mieke showed dislocation segments in mica of the order of 20 μm. Kronenberg et al. [71], working with biotite single crystals also concluded that the activation areas were "enormous" and could not be reconciled with the dearth of stacking faults found in TEM foils of deformed samples.

At higher stresses, the IKBs are sundered and devolve into parallel *mobile* dislocation walls. It is the coalescence of these walls into kink boundaries that eventually give rise to kink bands [18-20], and simultaneously lead to the cyclic hardening observed. Given that hardening *has* to be dislocation-based and kinking is known to occur in mica [63-66,70,71], it is reasonable to conclude that our kinking based model - used successfully to explain similar behavior in Ti_3SiC_2 and graphite – is also applicable here.

The most compelling evidence, however, that the *same* mechanisms are operative in all three quite different compounds is shown in Fig. 18b. In this plot, both axes are normalized by the appropriate elastic stiffness along the indentation axis; (i.e. 61 GPa in the case of grade B mica [67]). Based on the resulting *universal* curve it is fair to conclude that the same kinking-based mechanisms are operative in all 3 solids.

Typical FESEM micrographs of post-indentation craters formed after massive penetrations of the indenter in grade B micas are shown in Fig. 34b and c. Examination of Fig 34 reveals that the indenter clearly left an indent with some large cracks emanating from its center (Fig. 34a). Clear evidence for the formation of kink boundaries can be seen in Fig. 34b. The sharp bends - denoted by red arrows such as those observed in Fig. 34b and their orientation relative to the basal planes - have to be kink boundaries. The massive rotation of the lattice planes is also unambiguous.

At higher magnifications the pileups around the indenter are revealed to be delaminated basal planes (inset Fig. 34b). Note fine scale of delaminations. Such features are ubiquitous in Ti_3SiC_2 and other MAX phases and have been observed at all lengths scales [8,14,18-20,73,74]. This figures also provide irrefutable direct evidence for the breakup of the single crystal into smaller grains [Fig. 34b]; a key component of

our model. Almost identical microdomains were observed in indented graphite single crystals (chapter 4) [43].

Delaminations are inherent to the IKB to KB transformation. The ends of an IKB cannot dissociate without delamination. Such delaminations at tips of dislocation walls subjected to shear stresses were predicted by Stroh [42]. Without such delaminations, the lamellae would fracture, which is clearly not the case here (inset Fig. 34b). The delaminations most probably occur at the intersection of dislocation walls and arrays, eliminating the latter [20]. Note dislocation arrays are also inherent to the overall process; without them, the various lamellae could not shear relative to each other, the precursor for all that follows [18,20]. Such arrays have been observed in mica [6].

CHAPTER 6: EVIDENCE THAT $YBa_2Cu_3O_6$ IS A KINKING NONLINEAR ELASTIC SOLID

6.1 Introduction

Since the discovery of high T_c superconductors in 1985-86, there has been a great deal of interest in understanding the mechanical properties of $YBa_2Cu_3O_{6.5+\delta}$ (YBCO - where if δ is negative, the crystal structure is tetragonal and if δ is positive, the crystal structure is orthorhombic) and related compounds. The purpose of these studies were twofold; first to understand and optimize the shaping process, and second, to introduce structural defects by plastic deformation to act as pinning centers for vortices in bulk materials [75].

YBCO exists in two major polymorphs; a tetragonal $YBa_2Cu_3O_{6+\delta}$ (a = b = 0.3858 nm, c = 1.184 nm) phase and an orthorhombic $YBa_2Cu_3O_{7-x}$ (a = 0.38185 nm, b= 0.38856 nm, c = 1.16804 nm) phase. The latter is superconducting and is obtained by oxygenation of the former.

When YBCO is deformed at high temperatures, or at low temperatures under confining pressures, for the most part plasticity is achieved through grain-boundary sliding and movement of dislocations with <100> and <110> Burgers vectors. The confining pressures result in plasticity in the orthorhombic phase, at temperatures where climb is not a relevant mechanism. Consistent with its lamellar structure, in all cases, only basal (001) slip was observed. As far as we are aware, only one study evidenced non-basal slip but under very specific conditions, viz. shock compaction [76]. Other attempts of deforming confined samples with specific orientations designed to inhibit (001) glide, failed to demonstrate any dislocation activity out of this plane [77]. This

result is not too surprising given that dislocations with Burgers vector out of the (001) plane would be prohibitively expensive [78].

Some dislocations were also found to be dissociated in (001) following the reaction:

$$[010] \longrightarrow 1/6[03\bar{1}]+1/6[031]$$

Those dissociations, however, are not related to any plastic deformation mechanism but result from the local precipitation of a phase, which is favored on dislocations [79].

As discussed earlier (chapters 3, 4 and 5), solids with high c/a ratios – provided they do not twin - will deform by the formation of incipient and regular kink bands [22,43,44,46,80]. The reason this is a sufficient but not necessary condition is simple: with high c/a ratios the Burgers vectors of non-basal dislocations render them prohibitively expensive. These solids thus have only two mechanisms to relieve the stress: fracture and/or kinking. The latter can thus be described as kinking nonlinear elastic, or KNE, solids.

The purpose of this work is to present the results of nanoindentation experiments that strongly suggest that the tetragonal form of YBCO, with a c/a ratio of ≈ 3 is a kinking nonlinear elastic solid.

6.2 Experimental Details

Nanoindentations were performed using a 13.5 μm radius spherical diamond tip as explained in chapter 2. The experiments were carried out under load control up to maximal loads of 10, 100, 200 and 500 mN, held there for 15 s, and unloaded. The loading rate was between 0.3 and 2.5 mN/s. The corrected or shifted load/displacement curves were then converted to stress/strain curves.

6.3 Results and Discussion

Typical load-displacement curves obtained when the spherical indenter is loaded parallel to the c-axis repeatedly, in the same location are shown in Fig. 40a. Like similar experiments on Ti_3SiC_2 [46], graphite [43], and mica [44], the first cycle is open. In this case a permanent indentation of ≈ 50 nm was recorded. The subsequent curves, however, are fully reversible and reproducible. Furthermore, the areas enclosed by the first loop are roughly three times those of the repeat cycles. The corresponding stress-strain curves (Fig. 40b) are characterized by:

a) an initial elastic regime with moduli that varied slightly from location to location. The average for 8 different locations was 172±10 GPa. This value is ≈ c_{33} and lies in between the *ab initio* values of 138 GPa reported by Ledbetter et al.[81] and 271 GPa reported by Menon et al.[82]. It is much closer to the former than the latter, though. Note some of the scatter can indubitably be traced to the presence of the 211 phase and therefore a more precise determination of c_{33} would have to await work on purer samples.

Note in Fig. 40b, the initial slopes on loading, even during the first cycle, are identical to those upon unloading for all cycles. This result is not typical; for most other indentation experiments, the moduli calculated from the first loading were < 150 GPa. However, in all indentations, bar none, the moduli calculated from unloading or those calculated from subsequent initial reloading, were comparable. This result is not too surprising since there are many mechanisms that could result in lower moduli such as surface asperities, for example. Another possible factor is if the indenter on the first loading was not perfectly normal to the basal planes.

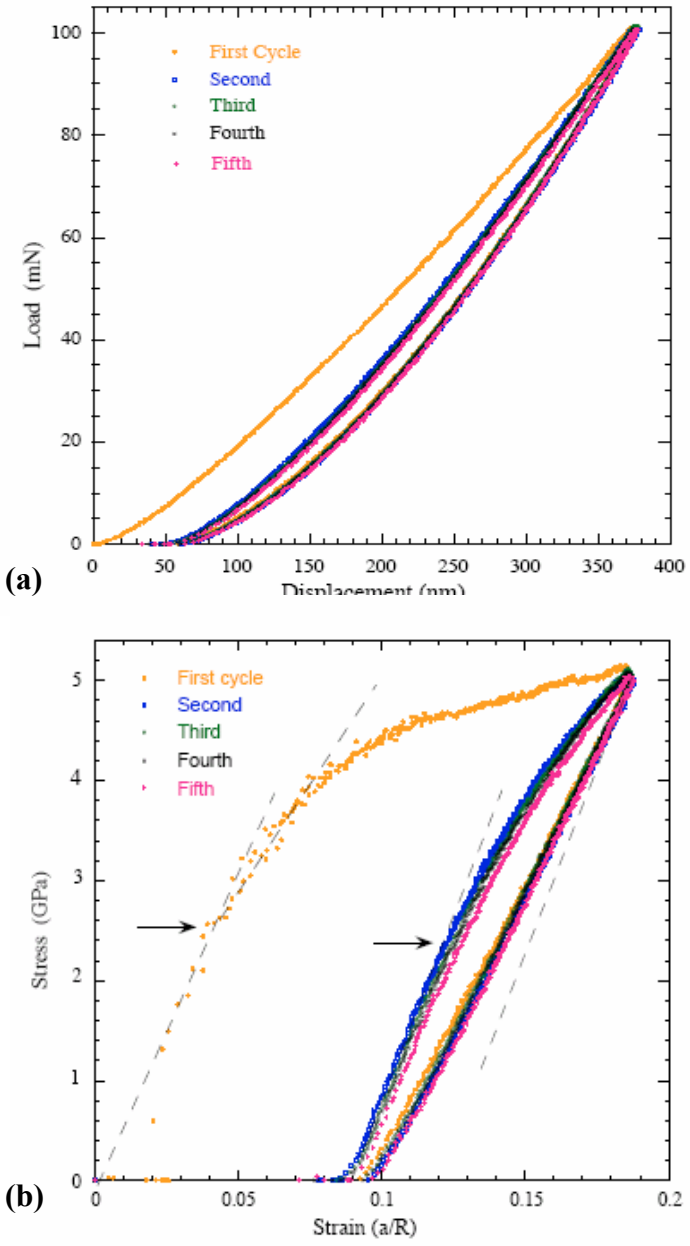

Figure 40: a) Load vs. depth-of-penetration results for a (001) surface of $YBa_2Cu_3O_6$ containing ≈ 20 vol. % Y_2BaCuO_5 loaded with a 13.5 µm spherical indenter five times in the same location. Cycles 2 to 5 were shifted to the right such that their unloading curves coincided with the first unloading curve. b) Stress-strain of results shown in a. Dashed lines are all parallel to each other, and correspond to a modulus ≈ c_{33} of 150 GPa. Note excellent reproducibility of the repeat cycles in both a and b.

With the testing of more oxides it is becoming clear that the moduli calculated on the first loadings are, more often than not, lower than theoretical. The presence of a second phase in this case could also have contributed to the scatter.

b) In Fig. 40b, at a contact stress of ≈ 2.5 GPa, which corresponds to a shear stress under the indenter, τ_{in}, of ≈ 1.25 GPa, a yield point, σ_y, is observed. This is followed by a region of strain hardening. Like the value of c_{33}, the yield points varied from region to region with an average value of 3±1 GPa. In previous work [43], σ_y was shown to be proportional to τ_c - viz. the stress needed to create a dislocation pair - because it was shown to be related to c_{44} according to:

$$\tau_c \approx \tau_{in} \approx \sigma_y /2 \approx c_{44}/n \qquad (3)$$

The value of n was ≈ 30 for graphite [43] and ≈ 60 for Ti_3SiC_2 [46]. For YBCO, the c_{44} values derived from *ab initio* calculations range from 61 GPa [81] to 84 GPa [82]. Therefore in this work n varied from ≈ 30 to 60, which are reasonable numbers and span the values measured for Ti_3SiC_2 and graphite. Note that the more perfect the crystal, the smaller the value of n.

The shear stress of Eq. 1 should not be confused with τ_c; the former is a remote stress and applies to polycrystalline samples (see below). The grains that kink first in a polycrystal are, i) the largest, ii) ones whose c-axes are normal to the compressive load, and iii) ones that contain defects that can act as potent stress concentrators. Interestingly enough, and not surprisingly, in a polycrystal, the distribution of kinking stresses is given by Weibull statistics [37].

c) The repeat cycles are fully reversible, reproducible and closed despite the fact that a small gap seen in Fig. 40b on total unloading of the second and subsequent cycles. We believe this is an artifact of the experiment for two reasons: First the load deflection curves are fully reproducible and reversible (Fig. 40a). Second, a few experiments were repeated at 100 mN over 30 times on the same location. Post-test examination in the SEM did not find a trace of the indentation, a fact that would not have been the case had each indentation incrementally increased the size of the crater (see below).

The reasons for these features and characteristics have been discussed previously and the details will not be repeated here [43,44,46]. In short, they can be explained by invoking the formation of IKBs that are fully reversible. At higher loads, the IKBs give rise of mobile walls that result in the permanent deformations observed in the first cycle. These in turn are swept into KBs, the formation of which reduces the domain size upon reloading. It is this reduction in α that results in the hardening observed. Note the area enclosed by each cycle is directly proportional to the cumulative dislocation activity during that cycle.

When the energy dissipated during each cycle, W_d, is plotted on a log–log plot versus the applied stress, σ, (Fig. 41) the slope is ≈ 2, in accordance with theory [37] and previous results (chapters 3, 4, 5) [22,43,44,46]. The results obtained herein fall in between those of Ti_3SiC_2 (chapter 3) [46] and graphite (chapter 4) [43], but are much closer to the former.

At loads less than 100 mN, no trace of the indentation was found in the FESEM. The same was observed for mica (chapter 5) [44], graphite (chapter 4) [43] and Ti_3SiC_2 (chapter 3) [46] and was attributed to two factors. First, the extent of the recovery is high at low loads. Second, the SEM is not the most sensitive technique to observe small shallow spherical depressions. Atomic force microscopy scans are indicated and planned. Indentations made with maximum loads of 200 or 500 mN resulted in shallow depressions clearly observable in SEM micrographs (Fig. 30a). Some of the indents, especially at higher loads, are characterized by a pileup of material, which is a characteristic of KNE solids [43,44,46]. For reasons that are not entirely clear, and in contradistinction to mica and graphite, clear evidence for KB formation was not found in the SEM micrographs (Fig. 42). However, similar to mica and graphite, the breakup of the single crystal into smaller domains is obvious at higher magnifications (Fig. 42b). This result cannot be overemphasized; it is crucial to our KB-based model because it is only be invoking a domain-size dependent, dislocation-based mechanism (i.e. Eq. 1) that the microstructure shown in Fig. 42b – with all the microcracks, defects, etc. - can actually be *harder and stiffer* than the original surface.

It is important to note that our KB interpretation can, for the most part, also account for the results of Huimin et al [83], who have shown that the first stress-strain curves of polycrystalline $YBa_2Cu_3O_{7-\delta}$ samples were open, but that successive re-loadings to the same stress resulted in fully closed, reversible and reproducible stress-strain curves. (Note the same behavior was observed in polycrystalline graphite; a fact that for many years had resisted interpretation, but that has recently been shown to be due to the formation of KBs [43]). Given the similarities between KBs and twinning, one cannot

disregard the possibility of fully "reversible" twinning as an alternate, though unlikely, interpretation. The results of this work are certainly intriguing enough to warrant further experiments on single crystals of $YBa_2Cu_3O_{7-\delta}$ to resolve this issue.

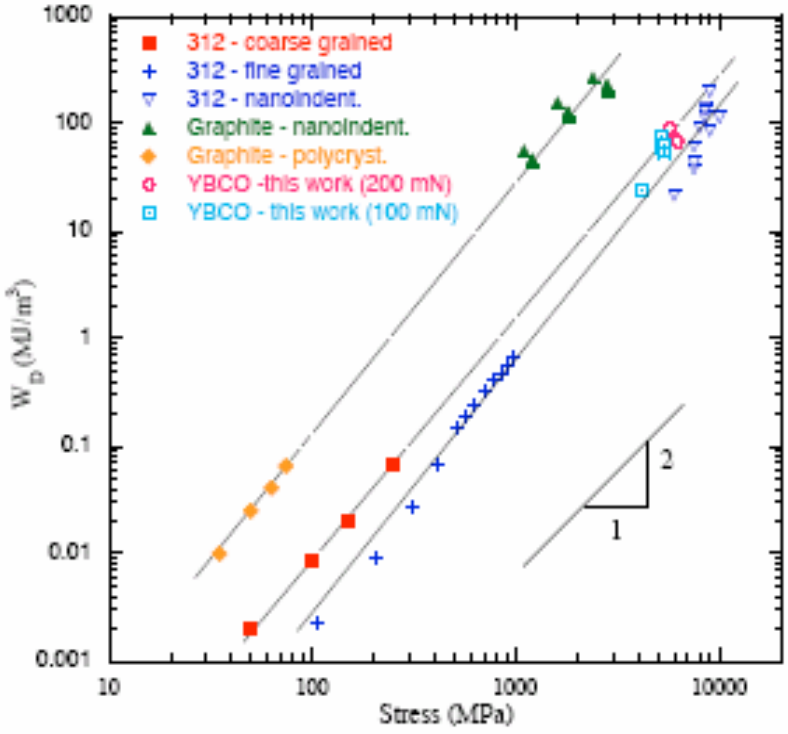

Figure 41: Log-log plot of W_d, versus maximum stress applied for $YBa_2Cu_3O_6$, bulk Ti_3SiC_2[6] and graphite[9], as well as from nanoindentations in Ti_3SiC_2[8] and single crystal graphite[9]. The W_d values for $YBa_2Cu_3O_6$ are comparable to those of Ti_3SiC_2.

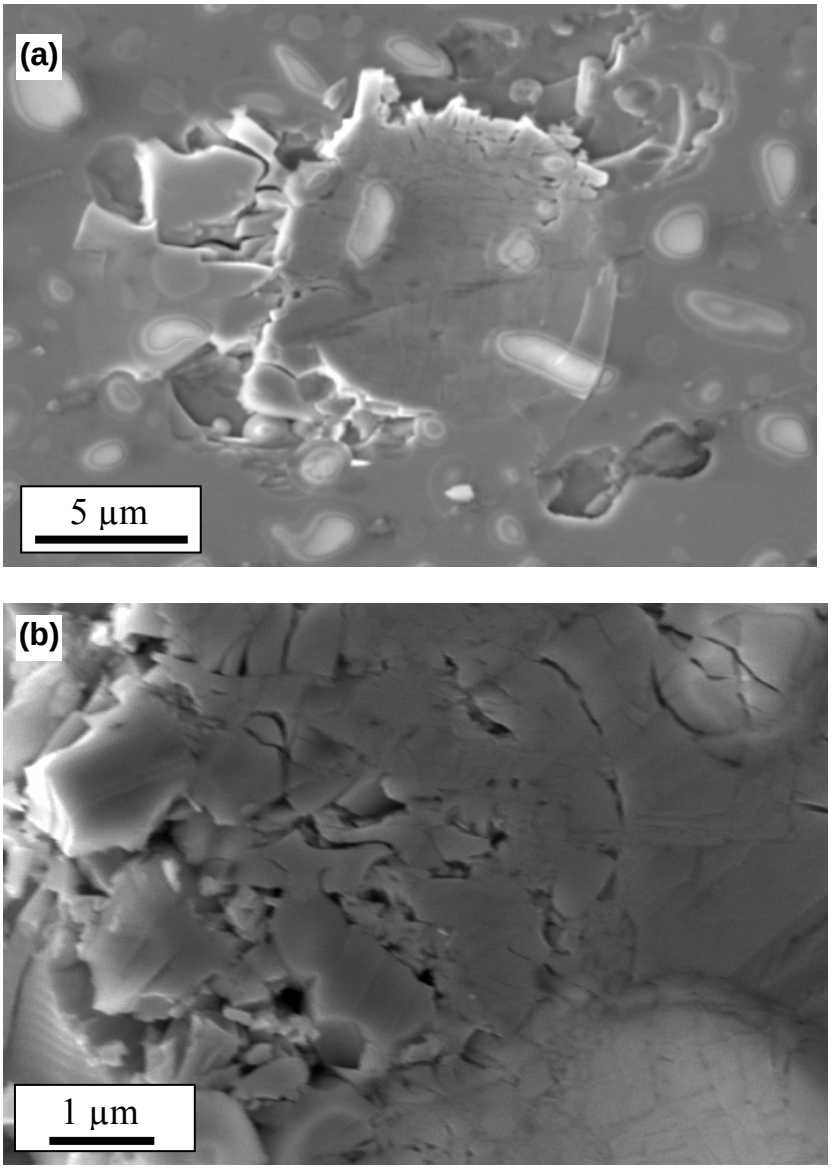

Figure 42: Field emission SEM micrographs of indents on a (001) $YBa_2Cu_3O_6$ surface containing ≈ 20 vol.% Y_2BaCuO_5 (bright phase in micrographs) at: a) low magnification showing indent and characteristic pileup around indentation; b) Higher magnification showing the breakup of the pristine surface into a multitude of smaller domains as a result of the indentation, a necessary component of our model.

CHAPTER 7: CONCLUSIONS AND FUTURE WORK

7.1 Conclusions

This work originally started out to study the deformation behavior of the MAX phases, Ti_3SiC_2 in particular, with respect to different microstructures such as fine grained, coarse grained, oriented grains and more importantly the behavior of single crystals. To this end, new processing routes were adapted and evolved such as pressureless sintering, tape casting, sinter forging and hot extrusion, with emphasis on the former two methods. This work shows that it is not only possible to pressureless sinter –325 mesh Ti_3SiC_2 powders to full density at 1600 °C, but it is also possible to orient the surface grains in the process with grain sizes in the order of few hundred microns. Sintering in the presence of C results in the formation of TiC_x, which, in turn, inhibits grain growth. Similarly, sintering in high Si activities results in the formation of Ti-silicides at the grain boundaries which also inhibit grain growth. Annealing of the latter in Ar at 1600 °C, for extended periods rids the samples of the silicides, which in turn allows for the grains to grow. The advantage of the latter process is that the final grain size distribution is more uniform from surface to bulk. The commercial availability of –325 mesh Ti_3SiC_2 and other MAX-phase powders, that can be pressureless sintered to full density without sintering aids represents a significant and noteworthy step towards synthesizing various microstructures.

To study the mechanical properties of single crystals at very high stresses, nanoindentation experiments were carried out with a 13.5 μm spherical indenter. This work showed that the mechanical response of Ti_3SiC_2 - and other layered solids such as graphite, mica, layered superconductors and as an extension all solids that have high c/a ratios that do not exhibit twinning - exhibit fully reversible closed hysteresis response. This hysteretic, reversible response without microscopic damage is attributed to the formation of incipient kink bands, which with increasing load levels generate mobile dislocation walls that eventually collapse into immobile kink boundaries.

The first indentations at high loads often produced some permanent deformation that signified the formation of kink bands. Repeated indentations in the same location to the same load level, however, resulted in the development of an equilibrium microstructure that was evidenced by fully reversible and repeatable load-displacement and stress strain curves. There was clear evidence of hardening in these repeated indentations lending further support to the kinking models proposed here to explain the measurements. For the most part, and despite significant plastic deformation under the indenter at stresses of the order of a few GPa, no traces of the indentations are found in post-indentation examination in these materials in a SEM, consistent with the fully reversible nature of the process. At high enough stresses, pop-ins were observed, resulting in permanent deformation. In the case of graphite the pop-ins resulted in the rupture of the basal planes and the indenter caused massive delaminations, kink bands and concomitant lattice rotations. These pop-ins under the SEM show unambiguous evidence for the reduction of the domain sizes under the indenter for these materials. In the case of mica, small pop-ins produced at high enough stresses healed completely. However, much higher stresses

resulted in large pop-ins that did not heal and were very similar to those observed in graphite.

A comparison of W_d from the nanoindentation measurements showed remarkable agreement with corresponding measurements from simple compression experiments when plotted against stress. This result suggests that the underlying mechanisms continue to be the same even at the high stress levels experienced in the nanoindentation experiments. Because the dislocations are confined to the basal planes, they do not entangle, and thus can move reversibly over relatively large distances. This feature results in the dissipation of substantial amounts of energy per cycle and accounts for the increase in W_d with increased stress levels. The proposed mechanism is valid over a wide range of stresses as seen from the work done vs. stress plots that show very good agreement over more than 4 orders of magnitude, between nanoindentations and simple compression experiments.

Nanoindentations on Ti_3SiC_2 reveal three distinct regimes of mechanical response:

(i) Linear elastic response with an Young's modulus of about 320 GPa, in directions parallel and normal to the c-axis of the crystal.

(ii) Hysteretic, reversible response without microscopic damage that is attributed to the formation of incipient kink bands, which with increasing load levels generate mobile dislocation walls, and eventually generate immobile kink bands. In this regime (up to about 200 mN loads) the first indentations often produce some permanent deformation that signifies production of kink bands. Repeated indentations in the same location to the same load level resulted in

the development of an equilibrium microstructure that was evidenced by fully reversible load-displacement curves. There was clear evidence of hardening in these repeated indentations lending further support to the kinking models proposed here to explain the measurements.

(iii) Plastic response with damage i.e. microcracking/delaminations. It is important to note here that when the samples were loaded parallel to the c-axis, with the highest load possible, little to no damage was observed.

Back extrapolated yield values were established. The indentation yield points in directions normal and parallel to the c-axis were estimated to be about 4.5 GPa and 4 GPa, respectively.

The work described here is of paramount importance for two main technological reasons. First, the fact that KBs can be initiated without apparent macroscopic damage raises several exciting possibilities. When this process is better understood, it could well lead to the development of processing methods for Ti_3SiC_2 for effectively refining a microstructure (possibly to nanolength scales!) without associated damage. Second, Ti_3SiC_2, and by extension the other $M_{n+1}AX_n$ phases, can be loaded repeatedly without damage, while simultaneously dissipating significant portions of the energy during each cycle. Based on this response it is fair to assume that such surfaces would be highly resistant to fatigue damage. When taken together with the fact that the friction coefficients of the basal planes are extremely low [23], the possibility of having high wear resistant surfaces that are very low friction is a tantalizing prospect. Furthermore, the prospect of exploring the more than 50 $M_{n+1}AX_n$ phases known to exist [8], and

innumerable combinations of solid solutions, is a wonderful one indeed, and one that should prove to be of technological and scientific importance and benefit. The absorption of energy during loading-unloading cycles could also in principle render the $M_{n+1}AX_n$ phases excellent surfaces for applications where vibration damping is desired; an important consideration for many Micro-Electro-Mechanical Systems (MEMS) applications.

This kinking-based model also explains the response of graphitic surfaces indented with a 13.5 μm radius spherical nanoindenter along the c-axis, and polycrystalline samples to mechanical stress. The model also can account for many aspects of the deformation of graphite that to date have resisted explanation. The key to the model is the identification of a fully reversible hysteretic element – labeled incipient kink bands - comprised of near parallel dislocation walls that are strongly attractive. As long as the stress level is insufficient to sunder the IKB's the mechanical response is characterized by fully reversible hysteretic loops. At higher stresses, the IKB's give way to mobile dislocation walls that result in plastic strain. The ultimate coalescence of these walls into kink boundaries that reduce the domain size account for the cyclic hardening observed.

For the most part, and despite significant plastic deformation under the indenter at loads corresponding to stresses of ~ 1 GPa, no traces of the indentations are found in post-indentation examination of the graphitic surfaces in a FESEM field emission microscope, consistent with the near fully reversible nature of the process. At high enough stresses, however, pop-ins of the order of 50 μm are observed as the basal planes rupture and the indenter causes massive delaminations, kink bands and concomitant

lattice rotations. These micrographs show unambiguous evidence for the reduction of the domain sizes under the indenter

The proposed model also explains the deformation behavior observed in layered superconductors. When (001) YBCO surfaces were indented with a 13.5 μm radius spherical indenter, all the telltale signs of KNE solids were observed. An initial elastic deformation with a modulus $c_{33} \approx 172 \pm 10$ GPa, was followed by a well-defined yield point that occurred at stresses of the order of $c_{44}/30$ to $c_{44}/60$. And while the first loop is open, subsequent loops are fully reversible, reproducible and closed. The totality of the results presented herein all indicate that the tetragonal phase of YBCO is another KNE solid wherein the permanent deformation during the first cycle is due to the formation of MDWs and kink boundaries. The latter reduce the size of the domains available to initiate new IKBs, which leads to the cyclic hardening observed between the first and subsequent cycles. Since the IKBs are by definition fully reversible, subsequent loadings do not lead to any further changes. The energy dissipated per unit volume per cycle is substantial: increases with increasing stress and results from the to-and-fro motion of basal plane dislocations.

When W_d was normalized by the appropriate elastic stiffness along the indentation axis (such as 325 GPa for Ti_3SiC_2, 36.5 GPa for graphite, 61 GPa for mica), the results collapsed on a single *universal* curve, from which it is fair to conclude that the same kinking-based mechanisms are operative in all these layered solids. This is a remarkable conclusion; despite the vast difference in the nature of bonding between the layers, the underlying physical mechanism for all these layered solids is apparently the same.

At first glance any relationship between nanoindentations and geology may seem farfetched. However, since the deformation under an indenter, like that of many rocks, is constrained it is possible to reach much higher stresses - and thus better mimic geologic conditions - than would normally be possible. Furthermore, the relationship between σ and W_d – which at high stresses may be a unique function - allows for extrapolations to even higher stresses with reasonable certainty (Fig. 18). Note W_d cannot increase indefinitely - an upper limit must exist when α is of atomic dimensions - further enhancing our predictive capabilities.

The relevance of the results presented herein to geology cannot be overemphasized. First and foremost, the identification of the origin of the hysteretic mesoscopic units (HMU), viz. the formation of IKB's, operative in NME solids should rapidly lead to a much deeper understanding – including the development of the requisite constitutive equations - of this important class of solids. Needless to add our model is consistent with all HMU-based models for which there has been a flurry of activity lately [6,60,61,84-87]. For example, based on this insight the response of NME solids can now be directly related to the volume fraction of the KB-prone phase. Such understanding is crucial for example, in predicting the "site response" in earthquake engineering, which in turn has a major influence on designing structures for minimal damage due to earthquakes [60]. This is especially true since it has been concluded that many of the materials near Earth's surface belong to this class of solids [60].

There are other important ramifications. First, since α is proportional to $1/\sqrt{\sigma}$ and W_d at high stresses appears to be a unique function of σ (Fig. 18), measurements of α can

lead to the estimation of the maximal geo-stress any KB-containing geologic formation had experienced.

Second, the mechanical response of a geologic formation comprised of a layered mineral becomes not only a function of its composition, but also its thermo-mechanical history – the more a rock is deformed the more it hardens. Third, the elastic properties of any layered rocks that deform by KBs measured by ultrasound – which is how much of the information is obtained in the first place - are of very dubious utility in predicting their macroscopic response. This is especially true since the ultrasound does *not* initiate IKBs; for example, the damping of Ti_3SiC_2 at room temperature as measured by ultrasound is not exceptional. Along the same lines, a solid under stress with a high density of KB's will have innumerable dislocation loops that in turn will respond to a perturbation, such as ultrasound, quite differently than the same rock with a different density of KB's.

Fourth, the presence of KB's and the nonlinear nature of the deformation can significantly amplify the amount of strain energy stored in a rock as compared to a purely elastic deformation, with obvious implications for seismology. As Fig. 18 shows, if the deformations are confined, energies of the order of 100 MJ/m^3 are possible.

Based on this, and previous [22,46] work it is evident that mechanically anisotropic solids – where a high c/a ratio is a sufficient, *but <u>not</u> necessary, condition* – will deform by kinking, provided they do not twin Thus a good descriptor of these solids is kinking nonlinear elastic (KNE) solids. KNE solids include layered minerals and ceramics - including possibly high T_c superconductors - NME solids [60,61], the $M_{n+1}AX_n$ phases [22,46], graphite [43], hexagonal BN and probably ice [21], among many others. Given

the diversity and ubiquity of these materials it is clear that IKB's and KB's play a much more important role in our daily life than has hitherto been appreciated.

The cross-fertilization that will ensue, together with the very large amount of work already existing on these materials much of which will have to be reinterpreted, should yield to quantum jumps in our understanding of all of them. Furthermore, the fact these solids, in all their diversity and ubiquity, are subject to the same physics - two dislocation walls attracted to each other, with dislocations confined to basal slip and complications arising from twinning absent - is not only truly sublime but one that can be readily visualized by undergraduate students.

The ramifications of this study cannot be overstated. First, the mechanical response of graphite - which has been studied for over a century but whose behavior has not been not well understood to date - is now clearer. This work accounts for most aspects of the deformation of graphite that to date have resisted explanation. Secondly, the conclusions from this study also bode well for rapid understanding of the mechanical properties of all of these layered solids, many of which have been studied extensively over the years. It now appears that solids with high c/a ratios - a sufficient but not necessary condition - will deform by kinking.

Third, the implication of this study to geology is enormous, given the fact that so many geologic materials are layered. Many rocks and most materials that comprise the earth's crust, have been classified as nonlinear mesoscopic elastic (NME) solids. The phenomenon of their reversible hysteresis was satisfactorily explained by the P-M space model, however, the underlying physics was totally unknown. This work clearly shows IKBs to be the hysteretic mesoscopic units (HMU) that were used to model their

mechanical behavior, thus proving that IKBs are responsible for the unique mechanical response of these solids. As expounded in chapter 5, this study should rapidly lead to a much deeper understanding of these materials, including the development of the requisite constitutive equations of this important class of solids. Understanding their behavior is critical, for example, in the prediction of "site response" in earthquake engineering and designing structures for minimal damage due to earthquakes.

Most importantly, understanding the physical mechanisms and thus having an in depth understanding of the mechanical behavior of these materials – individually and as a group – would be of immense benefit in harnessing these materials to their fullest potential for various applications.

The results of this work demonstrate the power of instrumented nanoindentation in general, and spherical indentations in particular, in furthering our understanding of the deformation mechanisms of KNE solids. The availability of a relatively simple non-destructive technique, that requires tiny samples to probe such solids at geologically relevant stresses, is a huge advantage that should lead to rapid advancement in our understanding and one that should prove of immense benefit. That nanoindentations can tell us anything about how an earthquake will shake the earth - a 15 orders of magnitude span of lengths scales - is remarkable.

Lastly, based on this work it is evident that mechanically anisotropic solids – where a high c/a ratio is a sufficient, *but <u>not</u> necessary, condition* – will deform by kinking, provided they do not twin. Thus a good descriptor of these solids is kinking nonlinear elastic (KNE) solids. KNE solids include layered minerals and ceramics - including possibly high T_c superconductors - NME solids, the $M_{n+1}AX_n$ phases, graphite, hexagonal

BN and probably ice, among many others. Given the diversity and ubiquity of these materials it is clear that IKB's and KB's play a much more important role in our daily life than has hitherto been appreciated.

7.2 Future Work

This study has conclusively proven that the mechanical response of layered solids can be explained in terms of IKBs that devolve to mobile walls at higher stresses and ultimately form KBs. Most of the work in these materials was performed on single crystals; it was, however, shown in the case of Ti_3SiC_2 at least, that polycrystalline samples also exhibit similar behavior despite the very high stresses under a nanoindenter. The effect of grain boundaries on the behavior of these solids is an interesting one, as seldom are these materials used and subjected to, as single crystals. It is thus important to understand the effects of the grain boundaries, if any, on the response of these materials.

IKBs by definition are reversible and thus observing them or detecting them directly is non trivial. However, it is possible that they might leave some evidence in the form of residual impressions such as possible dislocation entanglements near inclusions and subtle changes in crystal orientations where they could have formed after they have devolved to mobile walls. These could also be observed in *in situ* TEM experiments where the samples are loaded. Thus observing cross sections of the indentations could be very useful to observe and understand the evolution of IKBs to mobile walls and eventually to KBs. This would also give very useful information such as the dislocation distances, the parameters α and β defining the size of the IKBs, with respect to the grain size and applied maximum stresses.

Such reversible behavior could also be exhibited by other solids that are not necessarily layered, such as in rutile phase of TiO_2. It would be very interesting to study the mechanical response of these materials and to relate their response to the formation of IKBs.

To truly harness these materials to their fullest potential, constitutive equations and simulations, such as with finite elements, of their response to multi-axial stress states must be developed. One way to approach this problem would be to model these IKBs as HMUs, with associated properties and criteria for their nucleation, growth and dissociation. HMUs have already been studied and modeled, though without knowing the actual mechanism behind them. Thus modeling with IKBs would mimic reality and could include fundamental material properties such as dislocation interactions in the particular solid (such as lattice resistance to dislocation motion, dimensions of the IKB with respect to the grain size such as α and β and so on). This model would be truly remarkable in that atomistic scale modeling (in the sense of dislocation interactions) would lead to describing a phenomenon affecting literally on the "global" scale such as in the case of earth quake engineering.

LIST OF REFERENCES

1. Kelly BT. Physics of Graphite. Applied Science Publishers, London, 1981.

2. Sakai M, Nakano Y, Shimizu S. Elastoplastic indentation on heat-treated carbons. J Am Cer Soc 2002;85:1522.

3. Field JS, Swain MV. The indentation characterization of the mechanical properties of various carbon materials: glassy carbon, coke and pyrolytic graphite. Carbon 1996;34:1357.

4. Iwashita N, Swain MV, Field JS, Ohta N, Bitoh S. Elasto-plastic deformation of glass-like carbons heat-treated at different temperatures. Carbon 2001;39:1525.

5. Rieder M, Cavazzini G, D'yakonov Yu.S, et al. Nomenclature of the micas. Canadian Mineralogist 1998;36:905.

6. Christoffersen R , Kronenberg AK. Dislocation interactions in experimentally deformed biotite. J Struc Geolg 1993; 15: 1077.

7. Paterson MS and Weiss LE. Experimental folding in rocks. Nature 1962;195:1046.

8. Barsoum MW. The $M_{n+1}AX_n$ phases: A new class of solids: Thermodynamically stable nanolaminates. Prog in Sol State Chem 2000;28:201.

9. Molina-Aldareguia JM, Emmerlich J, Palmquist J-P, Jansson U, Hultman L. Kink formation around indents in laminated Ti_3SiC_2 thin films studied in the nanoscale. Scripta Mater 2003;49:155.

10. Pampuch R, Lis J, Stobierski L, Tymkiewicz M. Solid combustion synthesis Ti_3SiC_2. J Eur Ceram Soc 1989;5:283.

11. Barsoum MW and El-Raghy T. Synthesis and characterization of a remarkable ceramic: Ti_3SiC_2 . J Amer Cer Soc 1996;79:1953.

12. El-Raghy T, Barsoum MW, Zavaliangos A, Kalidindi SR. Processing and mechanical properties of Ti_3SiC_2: II, Effect of grain size and deformation temperature. J Am Cer Soc 1999;82: 2855.

13. El-Raghy T, Zavaliangos A, Barsoum MW, Kalidinidi S. Damage mechanisms around hardness indentations in Ti_3SiC_2. J Amer Cer Soc 1997;80:513.

14. Gilbert CJ, Bloyer DR, Barsoum MW, et al. Fatigue-crack growth and fracture properties of coarse and fine-grained Ti_3SiC_2. Scripta Mater 2000;42:761.

15. Radovic M, Barsoum MW, El-Raghy T, Wiederhorn S. Tensile Creep of Fine Grained (3-5μm) Ti_3SiC_2 in the 1000-1200°C Temperature Range. Acta Mater 2001;49:4103.

16. Low IM, Lee SK, Lawn B, Barsoum MW. Contact damage accumulation in Ti_3SiC_2. J Amer Cer Soc 1998;81:225.

17. Kuroda Y, Low IM, Barsoum MW, El-Raghy T. Indentation responses and damage characteristics of hot isostatically pressed Ti_3SiC_2. J Aust Ceram Soc 2001;37:95.

18. Barsoum MW, El-Raghy T. Room temperature ductile carbides. Met Mat Trans A 1999;30A:363.

19. Farber L, Levin I, Barsoum MW. HRTEM study of low angle boundary in plastically deformed Ti_3SiC_2. Phil Mag Lett 1999;79:4103.

20. Barsoum MW, Farber L, El-Raghy T. Dislocations, kink bands and room temperature plasticity of Ti_3SiC_2. Met Mat Trans 1999;30A:1727.

21. Barsoum MW, Radovic M, Finkel P, El-Raghy T. Ti_3SiC_2 and Ice. Appl Phys Lettrs 2001;79:479.

22. Barsoum MW, Zhen T, Kalidindi S, Radovic M, Murugaiah A. Fully reversible, dislocation-based compressive deformation of Ti_3SiC_2 to 1 GPa. Nature Materials 2003;2:107.

23. Myhra S, Summers JWB, Kisi EH. Ti_3SiC_2- A layered ceramic exhibiting ultra-low friction. Materials Letters 1999;39:6.

24. Field JS, Swain MV. Determining the mechanical properties of small volumes of material from submicrometer spherical indentations. J. Mater. Res. 1993;10:101.

25. Swain MV. Mechanical property characterization of small volumes of brittle materials with spherical tipped indenters. Mat. Sci. and Eng. A. 1998;253:160.

26. Gogotsi Y, Dominich V. High pressure surface science and engineering, Institute of physics 2004.

27. Tabor D. Hardness of Metals. (Clarendon Press, Oxford, United Kingdom, 1951).

28. Johnson KL. Indentation Contact Mechanics. Cambridge University Press, Cambridge, MA, 1985.

29. Fischer-Cripps AC. Review of analysis methods for sub-micron indentation testing. Vacuum 2000;58:569.

30. Oliver WC, Pharr GM. An improved technique for determining hardness and elastic modulus using load and displacement sensing indentation experiments. J. Mater. Res. 1992;6:1564.

31. Lawn BR, Padture NP, Cai H, Guiberteau F. Making Ceramics 'Ductile'. Science 1994;263:1114.

32. Guiberteau F, Padture NP, Lawn BR. Effect of grain size on Hertzian contact in alumina ceramics. J. Amer. Cer. Soc. 1994;77:1825.

33. Adams BL. Orientation imaging microscopy: Emerging and future applications. Ultramicroscopy.1997;67:11.

34. Field DP. Recent advances in the application of orientation imaging. Ultramicroscopy. 1997;67:1.

35. Kooi BJ, Poppen RJ, Carvalho NJM, De Hosson JTh.M, Barsoum MW. Ti_3SiC_2: A damage tolerant ceramic studied with nano-indentations and transmission electron microscopy. Acta. Mater. 2003;51:2859.

36. Sakai M, Nakano Y, Shimizu S. Elastoplastic indentation on heat-treated carbons. J. Amer. Cer. Soc. 2002;85:1522.

37. Tiejun Zhen. Dissertation, Drexel University, Philadelphia, PA – 19104, 2004

38. Katagiri G, Ishida H, Ishitani A. Raman spectra of graphite edge planes. Carbon 1988;26:565.

39. Piñol S, Sandiumenge F, Martinez B, Gomis V, Foncuberta J, Obradors X, Snoeck E, Roucau C. Enhanced critical currents by CeO_2 additions in directionally solidified $YBa_2Cu_3O_7$. Appl Phys Lett 1994;65:1448.

40. Holm B, Ahuja R, Johansson B. Ab initio calculations of the mechanical properties of Ti_3SiC_2. App. Phy. Lett. 2001;79:1450.

41. Barsoum MW, El-Raghy T, Rawn CJ, Porter WD, Wang H, Payzant A, Hubbard C. Thermal properties of Ti_3SiC_2. J. Phys. Chem. Solids. 1999;60:429.

42. Frank FC, Stroh AN. On the theory if kinking. Proc. Phys. Soc. 1952;65:811.

43. Barsoum MW, Murugaiah A, Kalidindi SR, Zhen T, Gogotsi Y Kink bands, nonlinear elasticity and nanoindentations in graphite. Carbon 2004;42:1435.

44. Barsoum MW, Murugaiah A, Kalidindi SR, Zhen T. Kinking nonlinear elastic solids, nanoindentations and geology. Phy. Rev. Lett. in press.

45. Swain MV, Field JS. Investigation of the mechanical properties of two glassy carbon materials using pointed indenters. Phil. Mag. 1996;74:1085.

46. Murugaiah A, Barsoum MW, Kalidindi SR, Zhen T. Spherical nanoindentations in Ti_3SiC_2. J. of Mat. Res. 2004;19:1139.

47. Iwashita N, Field JS, Swain MV. Indentation hysteresis of glassy carbon materials. Phil. Mag. A 2002;82:1873.

48. Gogotsi Y, Welz S, Ersoy DA, McNallan MJ. Conversion of SiC to crystalline diamond structured carbon. Nature 2001;411:283.

49. Richter A, Ries R, Smith R, Henkel M, Wolf B. Nanoindentation of diamond, graphite and fullerene films. Dia. and Rel. Mat. 2000;9:170.

50. Domnich V, Gogotsi Y. High Pressure Surface Science. In Nalwa HS editor. Handbook of Surfaces and Interfaces of Materials, Academic Press, NY 2001;2:195.

51. Stroh AN. Cleavage of metal single crystals. Phil. Mag. 1958;3:597.

52. Lorenz D, Zeckzer A, Hilpert U, Grau P. Pop-in effect as homogeneous nucleation of dislocations during nanoindentation. Phy. Rev. B 2003;67:172101.

53. Vidano R, Fischbach DB. New lines in the raman spectra of carbons and graphite. J. Am. Cer. Soc. 1978;61:13.

54. Dresselhaus MS, Dresselhaus G, Pimenta MA, Eklund PC. Analytical applications of Raman spectroscopy: Ed. Pelletier MJ, Blackwell Science Ltd., 1999.

55. Rand B. Mechanical Properties in Graphite and Precursors, Ed. Delhaes P, Gordon and Breach Science Publishers 2001:111.

56. Farber L, Barsoum MW, Zavaliangos A, El-Raghy T. Dislocations and stacking faults in Ti_3SiC_2. J. Am Ceram. Soc. 1998;84:1677.

57. Taylor R, Brown R, Gilchrist KE, Hodds AT, Kelly BT, Morris F, Hall E. Carbon 1967;5:519.

58. Woolley RL. Philos Mag 1965;11:799.

59. Medvedeva N, Novikov D, Ivanovsky A, Kuznetsov M, Freeman A. Electronic properties of Ti_3SiC_2 based solid solutions. Phys. Rev. B 1998;58:16042.

60. Guyer RA, Johnson PA. Nonlinear mesoscopic elasticity: Evidence for a new class of materials. Physics Today 1999;April:30.

61. Guyer RA, McCall KR, Boitnott GN. Hysteresis, discrete memory, and nonlinear wave propagation in rocks. Phys. Rev. Letters, 1995;74:3491.

62. Holcomb DJ. Memory, relaxation, and microfracturing in dilatant rock. J. Geophys. Res. 1981;86:6235.

63. Anderson TB. Nature 1964;202:272.

64. Donath FA. Am. Geophys. Union Trans. 1964;45:103.

65. Paterson MS, Weiss LE. Nature 1962;195:1046.

66. Paterson MS, Weiss LE. Experimental deformation and folding in Phyllite. Geolg. Soc. Am. Bull. 1966;77:343.

67. McNeil LE, Grimsditch M. J. Phys. Condens. Matter. 1993;5:1681.

68. Lawn BR, Wilshaw TR. Fracture of Brittle Solids, Cambridge Solid State Science Series, Cambridge University Press, 1975

69. Beall GH. Ann. Rev. Mater. Sci. 1992;22:91.

70. Meike A. In situ deformation of micas: A high-voltage electron-microscope study Am. Mineral. 1989;74:780.

71. Kronenberg A, Kirby S, Pinkston J. Basal slip and mechanical anisotropy in biotite. J. Geophys. Res. 1990;95:19,257.

72. Bell I. A, Wilson CJ. Tectophysics 1981;78:201.

73. Barsoum MW, Brodkin D, El-Raghy T. Layered Machinable Ceramics for High Temperature Applications.Scrip. Met. et. Mater. 1997; 36: 535.

74. Barsoum MW, El-Raghy T. A progress report on Ti_3SiC_2, Ti_3GeC_2 and the H-phases, M_2BX. J. Materials Synthesis and Processing 1997;5:197.

75. Sandiumenge F, Obradors X, Puig T, Rabier J, Plain J. Ceramic Transactions 2003; 140: 285.

76. Verwerft M, Dijken DK, De Hosson J Th M., Van der Steen AC. Different types of dislocations in $YBa_2Cu_3O_{7-\delta}$ Phys Rev. B 1994;50:3271.

77. Richard L, Dissertation thesis, University of Poitiers, 1997

78. Rabier J. Plastic deformation of ceramic materials. Plenum Press, Bradt RC, Brookes CA, Routbort JL, edt. 403 (1995).

79. Rabier J, Tall PD, Denanot M-F. On the dissociation of dislocations in $YBa_2Cu_3O_{7-\delta}$ Phil Mag A 1993;67:1021.

80. Zhen T, Barsoum MW, Kalidindi SR, Drexel University, private communication

81. Ledbetter et al. J Mater Res 1992;7:2905.

82. Menon et al. Solid State Comm 1992;81:357.

83. Huimin S, Yening W, Zhifang Z, Shiyuan Z, Linhai S. J Phys C: Solid State Phys 1987;20:889.

84. Capogrosso-Sansone B. Dynamic model of hysteretic elastic systems. Phys. Rev. B. 2002;66:2241011.

85. Delsanto PP, Scalerandi M. Modeling nonclassical nonlinearity, conditioning, and slow dynamics effects in mesoscopic elastic materials. Phys Rev B 2003;68:064107.

86. Moussatov A, Gusev V. Self-induced hysteresis for nonlinear acoustic waves in cracked material. Phys Rev Lett 2003;90:124301.

87. Gusev V. J Acoust Soc Am 2000;107:3047.

88. El-Raghy T, Barsoum MW. Processing and mechanical properties of Ti_3SiC_2: I, Reaction Path and Microstructure Evolution. J Am Cer Soc 1999;82:2849.

89. Li JF, Matsuki T, Watanabe R. Fabrication of highly dense Ti_3SiC_2 ceramics by pressureless sintering of mechanically alloyed elemental powders. J. Mater. Sci., 2003;38:2661.

90. Zhang GJ, Yue XM, Watanabe T. Al_2O_3/TiC/ ($MoSi_2$+Mo_2B_5) multilayer composites prepared by tape casting. J. Euro. Ceram. Soc., 1999;19:2111.

91. Qin S, Jiang D, Zhang J, Qin J. Design, fabrication and properties of layered SiC/TiC ceramic with graded thermal residual stress. J. Eur. Cer. Soc., 2003;23:1491

92. Ya Nan Liang, Soo Wohn Lee, Dong Soo Park. Effects of whisker distribution and sintering temperature on friction and wear of Si_3N_4-whisker-reinforced Si_3N_4–composites. Wear1999;225–229:1327.

93. Goswami AP, Das GC. Role of fabrication route and sintering on wear and mechanical properties of liquid-phase-sintered alumina. Ceramics International 2000;26:807.

94. Lim DS, Park DS, Han BD, Kan TS, Ho Jang. Temperature effects on the tribological behavior of alumina reinforced with unidirectionally oriented SiC whiskers. Wear. 2001;251:1452.

95. Tajima S, Tani T, Isobe S, Koumoto K. Thermoelectric properties of highly textured $NaCo_2O_4$ ceramics processed by the reactive templated grain growth (RTGG) method. Mat. Sci. and Eng. 2001;B86:20.

96. e,g. www.3ONE2.com.

97. El-Raghy T, Barsoum MW. Diffusion kinetics of the carburization and silicidation of Ti_3SiC_2. J. Appl. Phys. 1998;83:112.

98. Haihui Ye, Drexel University, unpublished results.

APPENDIX A: TAPE CASTING, PRESSURELESS SINTERING AND GRAIN GROWTH IN Ti_3SiC_2 COMPACTS

A.1. Introduction

The effect of different processing routes, such as reactive hot isostatic pressing (HIPing) and hot pressing (sinter forging), on the microstructural evolution of Ti_3SiC_2 were studied previously [11,88]. The reactive hot isostatic pressing of titanium, silicon carbide and graphite powders resulted in fully dense, predominantly single phase Ti_3SiC_2 samples with varying microstructures. Eight hours at 1450°C resulted in fine-grained (3-5 μm) samples; longer times (24 h) resulted in coarser (~200 μm) grains. The latter were also obtained at higher temperatures (1600 °C) and soaking times of at least 4 hrs. Between the two extremities of fine and coarse grains, a duplex microstructure having large grains (100-200 μm) embedded in a finer matrix was also obtained at intermediate processing times and temperatures. The growth rates were anisotropic; growth along the a-axes was higher than along the c-axis. The presence of TiC in the samples was also observed to inhibit grain growth. Very large oriented grains were obtained through sinter forging [18] of porous preforms of Ti_3SiC_2 obtained by pressureless sintering of cold pressed powders of Ti, SiC and graphite. The porous preforms were uniaxially compressed in a graphite channel die; the grains deformed under plane strain conditions and grew to sizes of the order of millimeters.

Recently, Li et al. [89] reported that mechanically alloyed elemental Ti, Si and C powders could be pressureless sintered to full density to yield compacts that were 80 vol. % Ti_3SiC_2; balance TiC_x. As far as we are aware this is the only report in the literature on the pressureless sintering of Ti_3SiC_2-based compacts.

Finally all of our work to date has been on samples fabricated by reactive HIPing. This strategy was adopted for two reasons. The first is to ensure that the grain boundaries of the samples made were as clean as possible so as to allow us to measure the intrinsic properties of the carbides fabricated. The second was one of necessity; it is non-trivial to make large quantities of very fine powders at the lab scale without undue contamination of the powder surfaces. The very recent commercial availability of – 325 mesh Ti_3SiC_2 powders, however, renders this study possible.

The ultimate objective of this work was to fabricate very large grained, preferably single crystal, samples of Ti_3SiC_2, with highly oriented microstructures for characterization of mechanical properties at the crystal level. In the process of this study we were able to gain insight in the grain growth kinetics of Ti_3SiC_2 sintered compacts. To achieve our objective we employed two techniques. The first was tape casting, followed by cold pressing and pressureless sintering. Tape casting is a well-established process used for the fabrication of substrates, multilayered structures such as capacitors, primarily in the electronic industry, solid oxide fuel cells, etc. [90-95].

Tape casting is a fabrication process for powders to produce thin sheets with an aid of a binding and plasticizing agent. Tape casting uses a doctor blade, or a thin slit through which the powder in the form of thick slurry, mixed with the binder and plasticizer is passed through, as schematically shown in Fig. 43. The slurry thus coming out is in the form of thin sheet, determined by the thickness of the nozzle/doctor blade. The slurry then dries, forming a tape that can be sintered to obtain the desired product.

The powder is milled with an appropriate binder, a deflocculant for dispersion of the particles and a plasticizer for flexibility of the tapes in an appropriate medium such

water (aqueous) or any other medium such as alcohols. The quality of the tape cast depends on the choice of the binder, deflocculant, plasticizer and the medium. The slurry is milled well and the resultant slurry is thixiotropic and shear thinning. The morphology of the powder should be flaky, thus when the slurry is fed through a narrow opening such as a nozzle or a doctor blade, viscosity drops due to the shear thinning effect of the slurry.

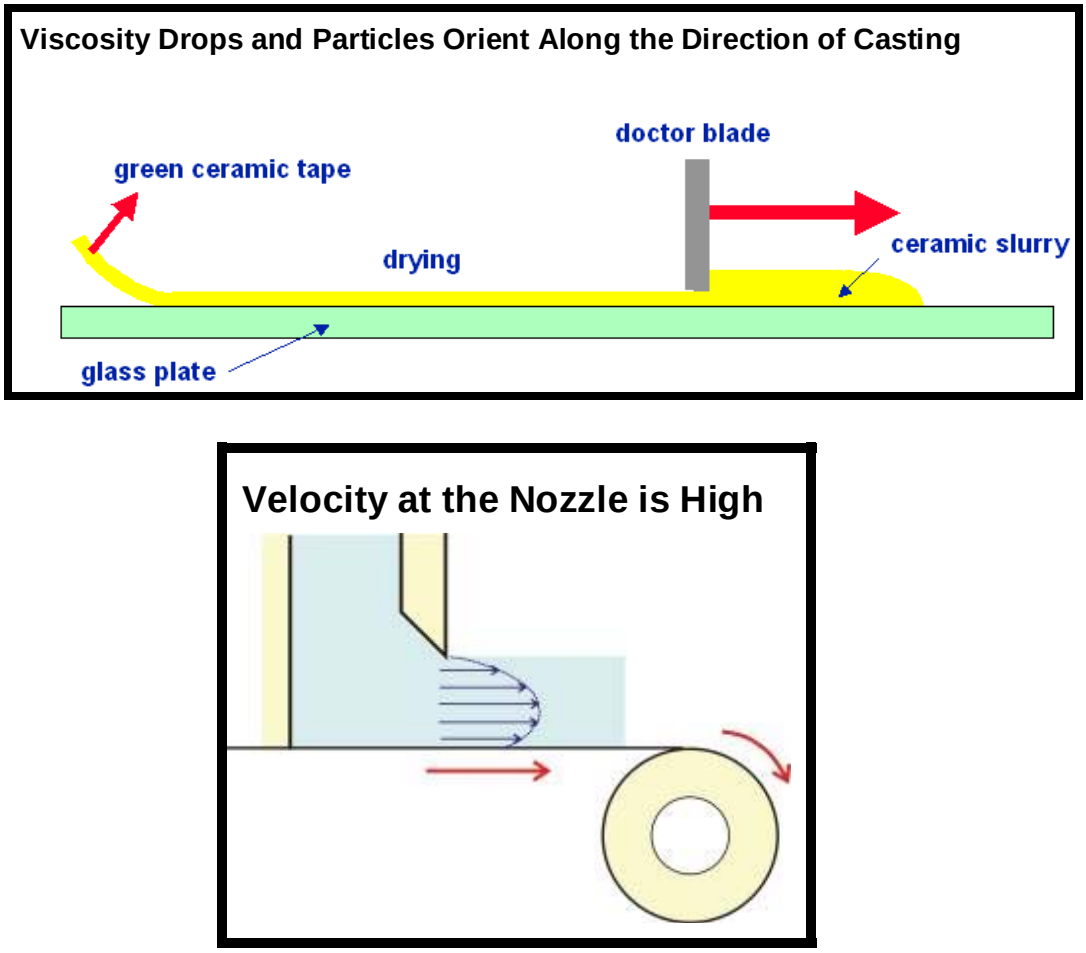

Figure 43: Schematic of tape casting process

The powder aligns along the direction of the flow and results in an oriented lay-up of the powder particles on the base. The viscosity of the slurry increases as soon as the slurry leaves the nozzle of the doctor blade, trapping the grains in a highly oriented lay-up.

A second approach involved the manual shaking of flaky Ti_3SiC_2 powders in a die prior to compaction. A third approach was also tried in which a new method to orient the particles was attempted by using a device to lay successive thin layers of powders that were oriented, to the desired thickness.

A.2. Experimental Details

A.2.1 Tape Casting

The Ti_3SiC_2 powders obtained (3ONE2, Vorhees, NJ) were somewhat flaky, and thus almost ideal for tape casting. The powders were mixed to an aqueous slurry with a 35 wt. % solid loading, 0.25 wt. % deflocculant (Darvan C®), 0.5 wt. % plasticizer (Polyethylene glycol) and 3 wt.% binder (hydroxypropylmethyl cellulose). All the ingredients, except the Ti_3SiC_2 powder, were added to distilled water and magnetically stirred. Once the binder dissolved, the Ti_3SiC_2 powder was added and the mixture was stirred with a rotary blade for about ~ 2 h to mix the powders with the binder. The mixture was then ball milled for 8 h in a ball mill using alumina balls.

Two powders were used; one with an average particle size of 40 μm; the other 5 μm. Both powders contained ≈ 5 vol. % TiC. Two different viscosity binders were tried; low, (60 cps) and high (3500-5600 cps). The finer (5 μm) Ti_3SiC_2 powder formed a viscous thixiotropic slurry which gave good flexible tapes and thus further experiments were

carried out only with the 5 μm powders and the high viscosity slurry. A doctor blade was used for the tape-casting; the gap thickness was fixed at around 400 μm. The tape was cast and allowed to dry overnight; the thicknesses of the tapes after drying were ≈ 100 μm. SEM image of one such tape is shown in Fig. 44. The tape was cut into smaller pieces of 1.5 x 3cm^2, stacked (40 to 50 tapes, roughly 10 mm) and warm pressed for 10 minutes at 200°C at 2.5 MPa or 6 MPa. To burn out the binder, the tapes were heated at the rate of 5°C/min to 500°C for 3 hrs in Ar, before heated directly to 1600°C at a rate of 8 °C/min. The samples were held at temperature for 4 h. The resulting sample surface was shiny and large grains were visible to the naked eye.

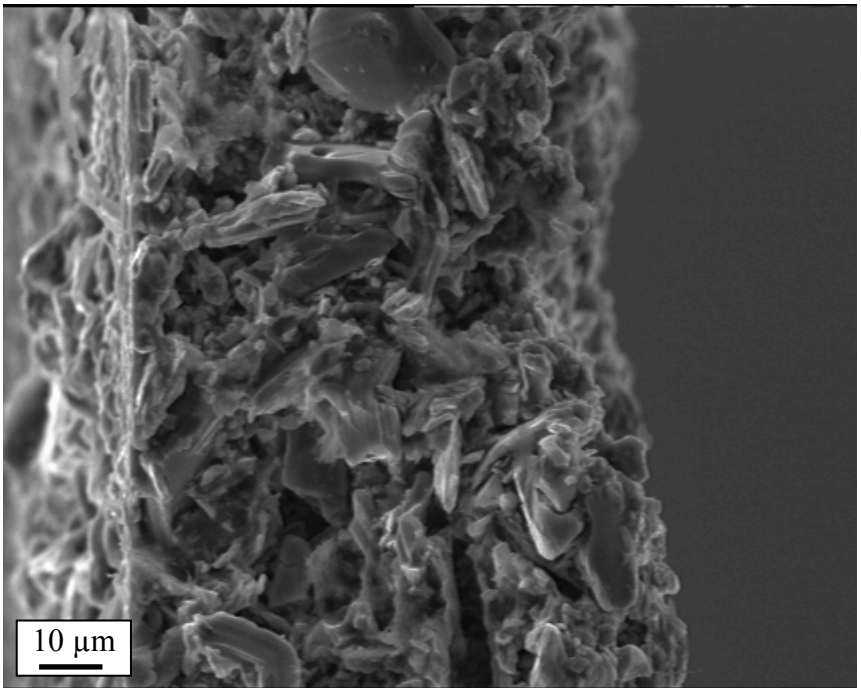

Figure 44: SEM image of the cross section of dried tape.

A.2.2 Cold Pressing

In another set of experiments, the powders were simply poured in a steel mold and manually vibrated in an attempt to orient the grains. To avoid delaminations and cracking during sample ejection from the die, a few drops of methanol were added to aid in particle packing and increase the green strength. In this case, the pressed samples were directly heated to 1600 °C at 8°C/min and held at temperature for 4 h.

Another new approach to orient the particles was attempted by using a device to lay thin layers of powder that were oriented – this was achieved by pressing a thin layer of powder on the mold surface. Due to the flaky nature of the particles, pressing a thin layer of the powder aligned the particles – this was evident from the X-ray scans (not shown). Further layers were laid on top thereby having a controlled layer by layer build to adequate sample thickness. Fig. 45 shows a schematic of the device consisting of a plexiglass die with a movable punch and mold. A layer of oriented powder was generated by squeezing the powder between 2 glass slides that make the particles to lie flat along their basal planes. This layer of oriented powder was then laid in the die cavity created by lowering the punch. This is similar to what happens in tape casting, except there was no binder. The punch was then slightly lowered and a new layer was laid. The process was repeated till sufficient thickness was achieved. A few drops of methanol was added to enhance particle packing and green strength. The powder preform was then transferred to a steel mold, cold pressed and sintered.

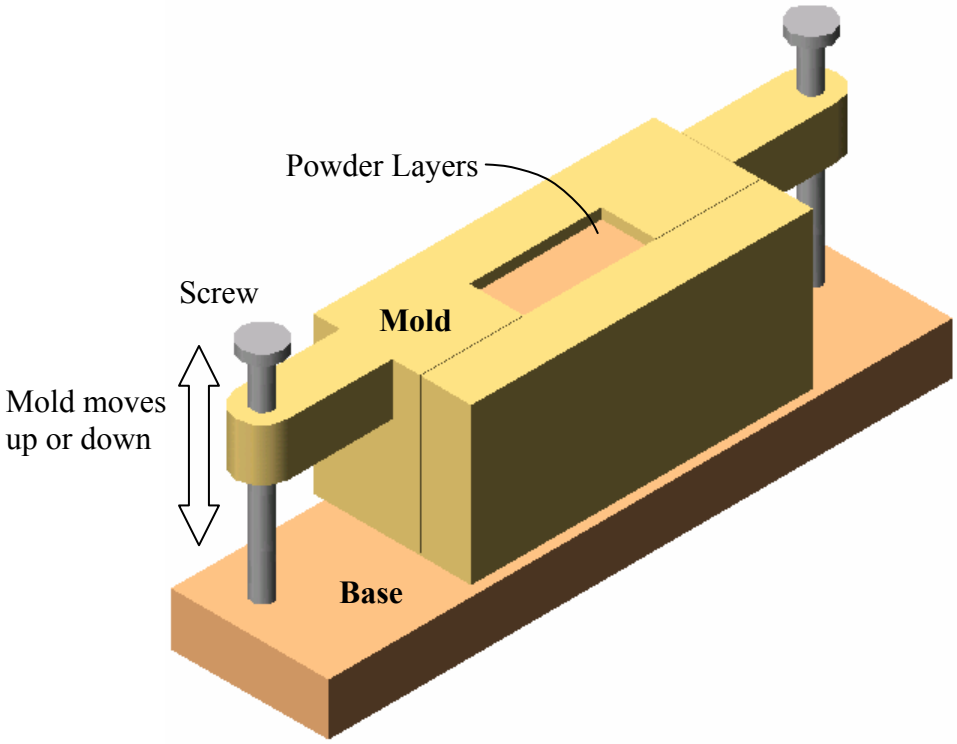

Figure 45: Schematic of the fixture used for layering powder in layers

The grain growth kinetics at 1600 °C were studied by further annealing the samples in an alumina tube under flowing Ar. On the assumption that the loss of Si results in TiC_x, which, as discussed below, is believed to retard grain growth, we heated three different powder configurations at 1650°C for 8 h in a graphite-heated vacuum furnace. First, a cold pressed sample of Ti_3SiC_2 powders was placed in an alumina boat next to a small mound of Si powder (< 20 μm - Elkem Metals Company, Niagara Falls, NY). Another sample was a compact of a mixture of 10 wt. % Si powder, balance Ti_3SiC_2. The third sample of pressed Ti_3SiC_2 powders was used as control. All samples were

sintered in covered alumina crucibles to minimize exposure to carbon from the heating elements.

Most sintered samples were studied by X-ray diffraction (XRD - model D-500, Siemens, Karlsruhe, Germany), with scanning step (2θ) of 0.05° and a scanning rate of 0.1°/s. Cross sections of polished and etched sintered samples were observed under an optical microscope (OM), and the grain sizes were measured by the intercept method. Since, for the most part, the grains grow as thin plates, the grain sizes reported here are the *diameters*, or longer axes, of the grains. The samples were studied with field emission scanning electron microscopy (FESEM) and energy dispersive spectroscopy (EDS).

A.3. Results and Discussion

A comparison of the XRD patterns of the as-received powders (Fig. 46a) and those of a tape-cast and sintered surface (Fig. 46b) makes it clear that the basal planes in the latter are strongly aligned parallel to the surface. The intensities of most non-basal peaks almost vanish, while those of the basal planes are pronounced (compare Fig. 46a to 46b).

Typical microstructures of sintered tapes are shown in Fig. 47. Note that apart from a few large cracks, the samples are fully dense. However, and invariably after sintering in Ar for 4 h at 1600 °C, the surface grains were significantly larger than the ones in the center, with the former penetrating roughly 100 to 200 μm into the bulk (Figs. 47a and b). Further annealing in Ar for 24 h resulted in the growth of the core grains faster than the surface ones (Fig. 47c).

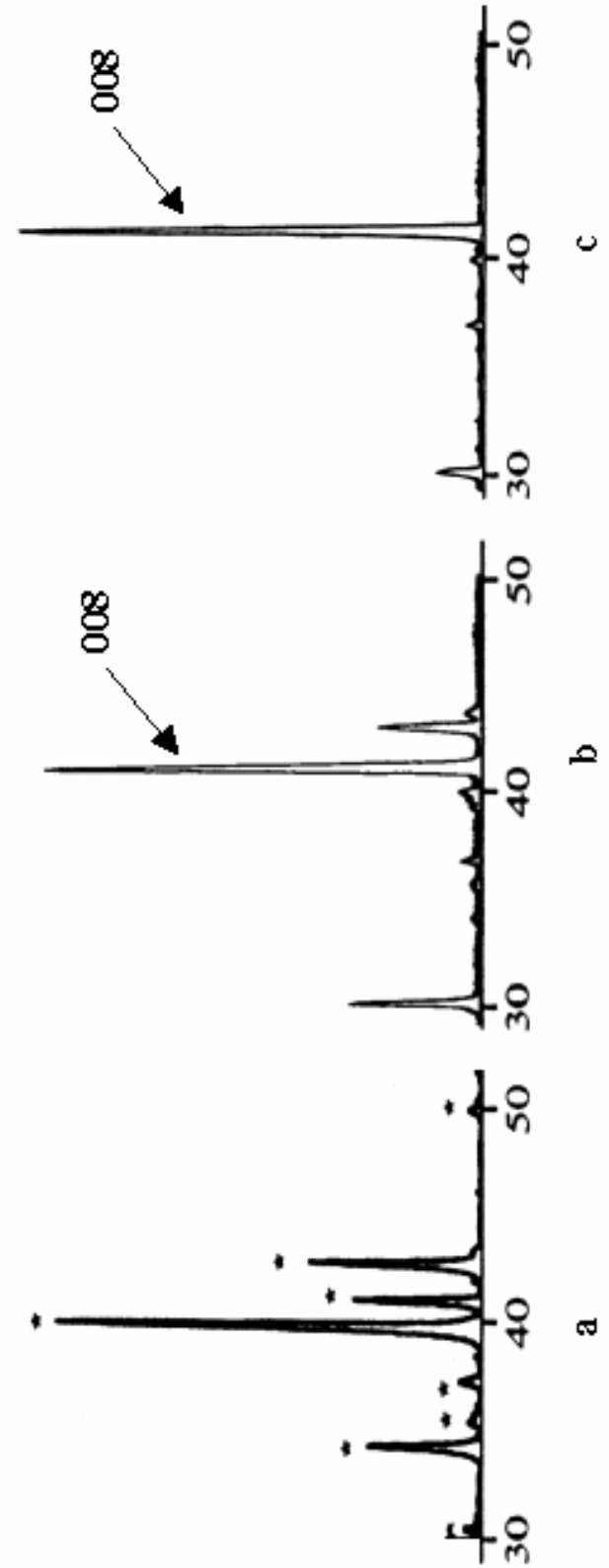

Figure 46: XRD of Ti_3SiC_2: **a)** as-received powders where the grains are randomly oriented; **b)** Top surface of tape cast and sintered sample, **c)** Top surface of tapped and sintered sample - note intensity of the 008 peaks.

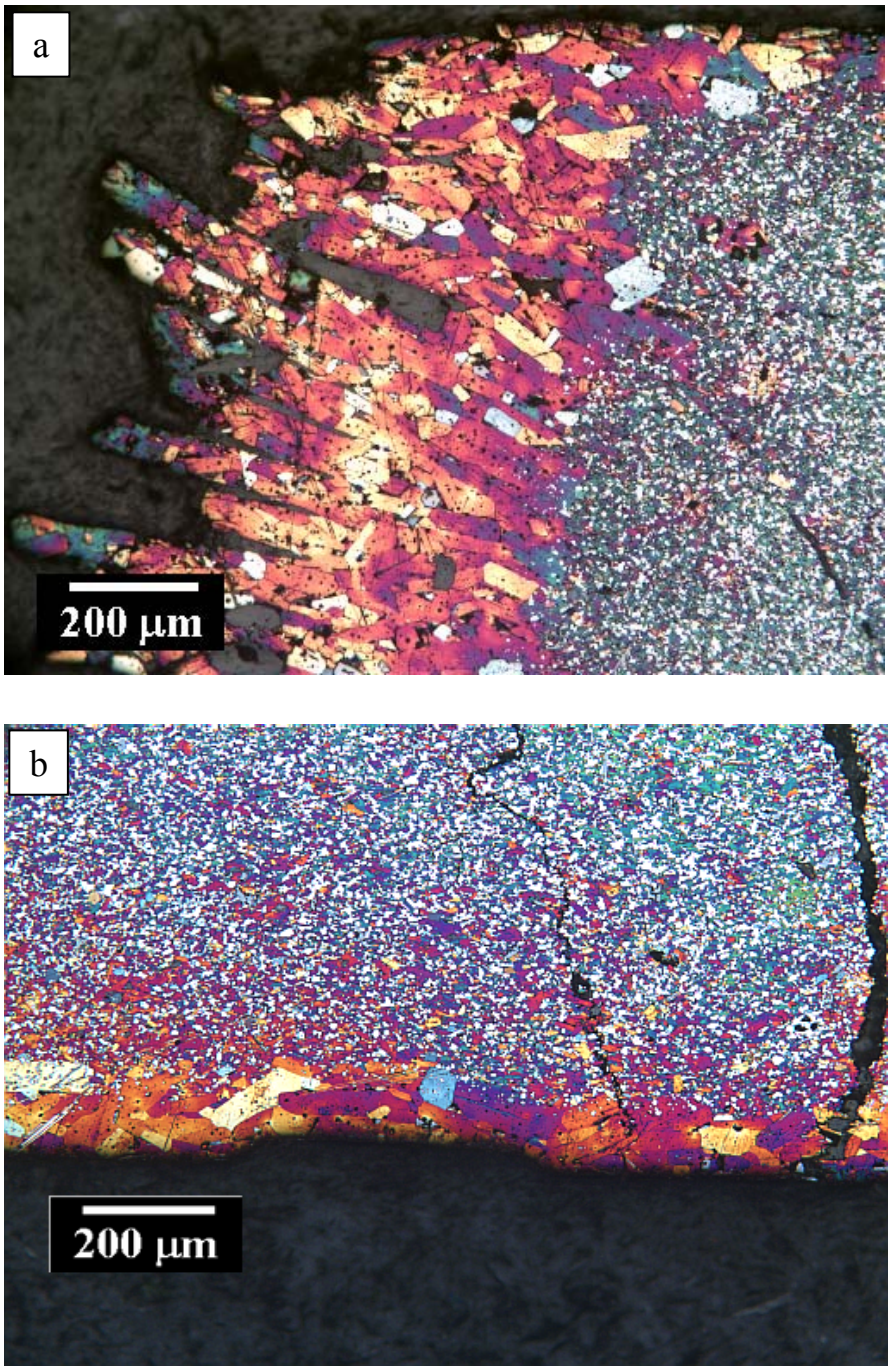

Figure 47: Typical OM micrographs of polished and etched cross sections of tape cast and sintered Ti_3SiC_2: **a**) Cross-section near corner of sample annealed at 1600 °C for 4 hrs. Note each protrusion represents one tape cast film. **b**) Same as **a**, but emphasizing the differences in size between surface and core grains. White specs in microstructure are TiC_x particles

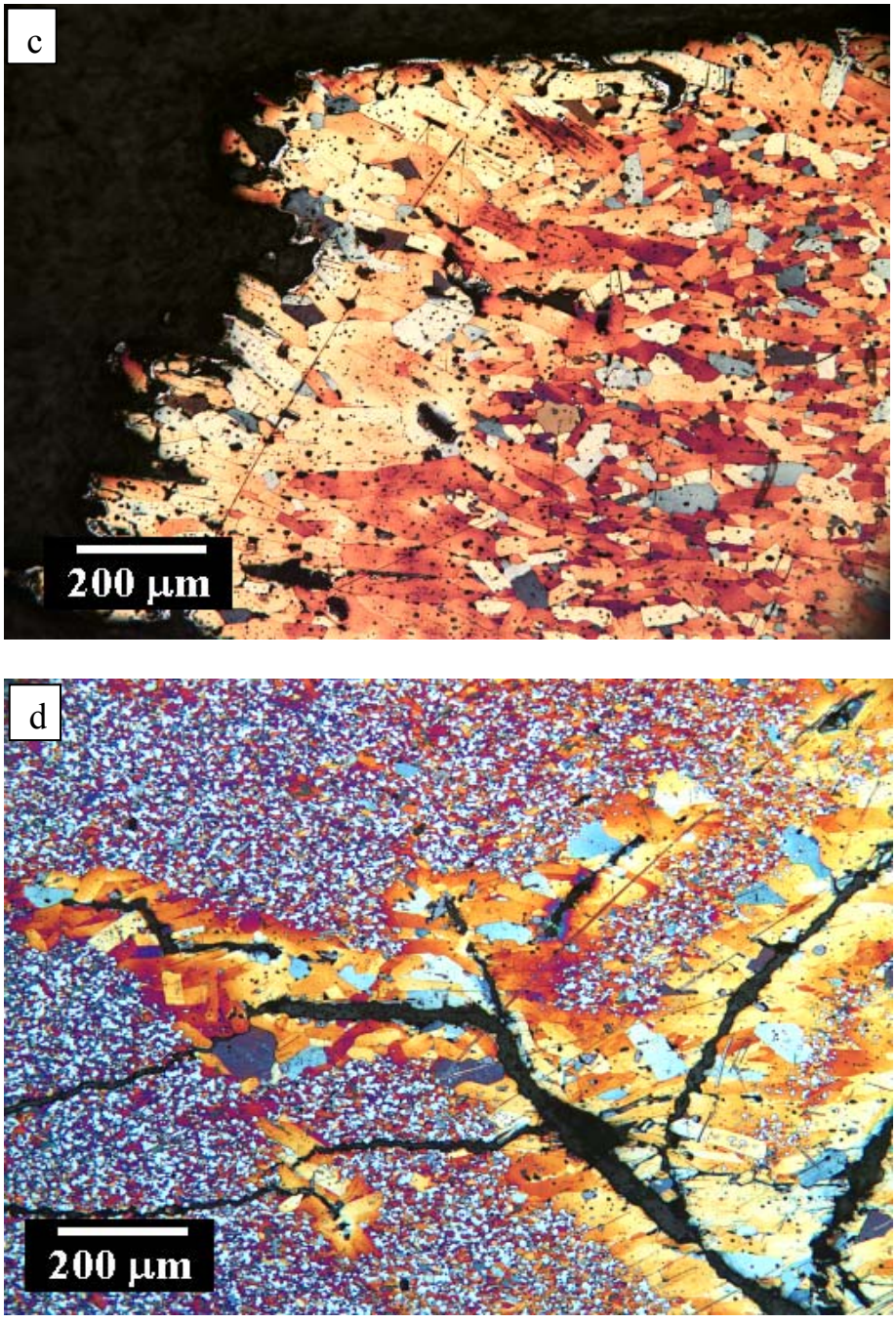

Figure 47: **c**) Same as a, after further annealing at 1600 °C for 24 hrs. Note center grains are now significantly larger. **d**) Effect of cracks in green body on grain growth.

The first 3 rows in Table 2 summarize the aforementioned results. It is important to note that the cracks observed were formed either during ejection of the samples from the dies or as a result of binder burnout. This problem does not occur when parts are cold isostatic pressed (CIPed) without binder. Fully dense (4.5 Mg/m^3) large parts are routinely sintered and are currently commercially available [96].

Table 2: Summary of grain size results as a function of the various heat treatments and anneals carried out in this work.

Processing Details	Cumulative time (h)	Temp (°C)	Surface grains (μm)	Core grains (μm)
Tape Cast (2.5 MPa) for	4	1600	112±44	11±5
+ 24 hrs.	28	1600	157±64	68±33
Tape Cast (6 MPa)	28	1600	120±44	10±6
Press and sinter for	4	1600	300±165	20±9
+ 24 h	28‡	1600	530±300	30±17
+ 24 h	52	1600	633±320	31±12
Sintering with 10 wt. % Si in compact	8	1650	71±43	74±41
Sintering with Si in boat	8	1650	17±9	15±9
+ 24 h	32‡‡	1600	175±90	175±90
Control (no Si)	8	1650	13±7	13±7

‡ This represents cumulative time at temperature.

‡‡ In this case while the cumulative time is 32, the first 8 h were at 1650 °C.

The core microstructures of the sintered tapes were characterized by: i) much smaller grains than those near free surfaces; and, ii) contained a significantly higher volume fraction of TiC_x (15-25 vol.%) than the starting powders. TiC_x is known to be a potent

inhibitor of grain growth in Ti_3SiC_2 [88] and it is therefore not surprising that, at least initially, the core grains did not grow as fast as the surface grains. Note that below a critical volume fraction the Ti_3SiC_2 grains can, and do, grow around and engulf the TiC_x particles. The role of the latter in those circumstances is that of delaying grain growth, rather than totally suppressing it. This is best seen in Table 2 (core grains in rows 1 and 2); clearly after the initial 4 h sintering, the rate of growth of the core grains is higher than the surface grains.

Since it is well established that Ti_3SiC_2 reacts with C to form TiC_x [97], the likely source of the latter is the binder. The most compelling evidence for this conjecture is the OM micrograph shown in Fig. 47d, where it is clear that grains in the near vicinity of cracks linked to the surface are significantly larger than ones in the bulk. It is thus fair to conclude that the presence of the cracks allows the binder to escape from the compact during heating, reducing the activity of C, which in turn reduces the vol. fraction of TiC_x. To further test this hypothesis we compared the microstructures of two tape compacts warm compacted at two different pressures, 2.5 and 6 MPa. After sintering for 4 hrs. at 1600 °C, they were further annealed for an additional 24 hrs at the same temperature. The samples that were pressed at 6 MPa had a significantly higher volume fraction of TiC_x and the grains were significantly smaller (compare rows 2 and 3 in Table 2). Based on these observations it appears that lower compaction pressures (2.5 MPa) allow for easier binder burnout and ultimately larger grains.

These results prompted us to attempt to align the grains by forgoing the binder altogether and simply vibrating the powders in the mold. The fact that the powders were flaky to begin with was deemed to be useful. XRD spectra of the sintered samples made

by simple tapping (Fig. 46c) revealed that the alignment was comparable to that obtained by tape casting. However, optical micrographs of sintered samples indicated that the large surface grains were not as well oriented as those of tape cast samples; some grains also had prismatic orientations. Interestingly, the core grains, while still small, were reasonably well oriented. Careful examination of the sintered compacts indicate that the TiC_x content in starting powders was of the order of ≈ 5 vol. %.

The results of the grain growth study carried out at 1600 °C in Ar, on samples made from the tapped powders are shown in Fig. 48 and listed in Table 2. In ≈ 50 h, the core grains grow from ≈ 20±9 μm to 30±12 μm; the surface grains grow from 300±165 μm to 630±320 μm (Fig. 48). At this juncture the pertinent question that holds the key to understanding this gradient in grain sizes from the surface into the bulk is: did the surface grains grow abnormally fast *or* was the growth of the core grains stunted?

At 1600 °C, the grain boundary velocity parallel to the basal planes in Ti_3SiC_2 is estimated to be ≈ 120 μm/hr [88]. Because this value was measured on reactively HIPed Ti_3SiC_2 samples for which the grain boundaries were shown to be free of any second phases [98], these velocities are believed to approach the intrinsic grain boundary velocities for Ti_3SiC_2. In practical situations however, impingement limits the final size of the grains to roughly 100-300 μm after 4 hrs. at 1600 °C [88].

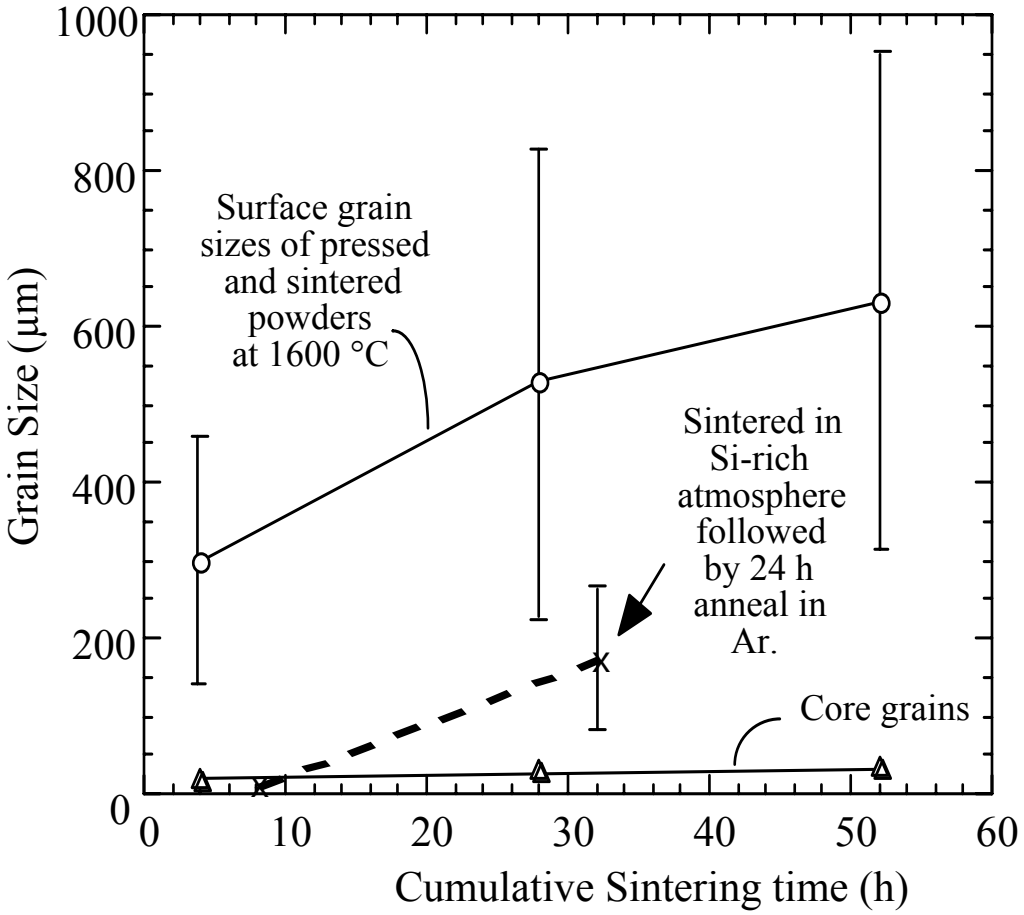

Figure 48: Results of grain growth study carried out at 1600 °C in Ar on samples made from the tapped and cold pressed powders. Dashed line represents sample sintered initially in the presence of silicon in a vacuum furnace and subsequently sintered in Ar for 24 hrs.

Comparing these values with those shown in Fig. 48, it is clear that the surface grains are the ones growing at rates comparable to those in the reactively HIPed samples; the core grains, on the other hand, are growing at a significantly slower rate. In other words, grain boundary mobility is reduced in the compacts made from pre-reacted Ti_3SiC_2 powders. It is thus fair to conclude that annealing in Ar cleanses and/or somehow thermally etches the powder surfaces near the compact surfaces prior to densification,

removing impurities that reduce grain boundary mobilities. Once cleansed, the grains appear to grow rapidly. In the remainder of this paper we present further evidence consistent with these notions.

The best evidence can be found in the optical micrographs of tapped and sintered samples (Fig. 49). Here again surface grains, and those in the near vicinity of cracks are larger than the core grains (Fig. 49b and c). These results directly show, that, at least initially, even in the absence of a binder, the grain growth rates at, or near, free-surfaces are significantly higher from those in the bulk. Note in this case no binder was used, and thus the beneficial effect of annealing in Ar on mobility is intrinsic to the Ar atmosphere.

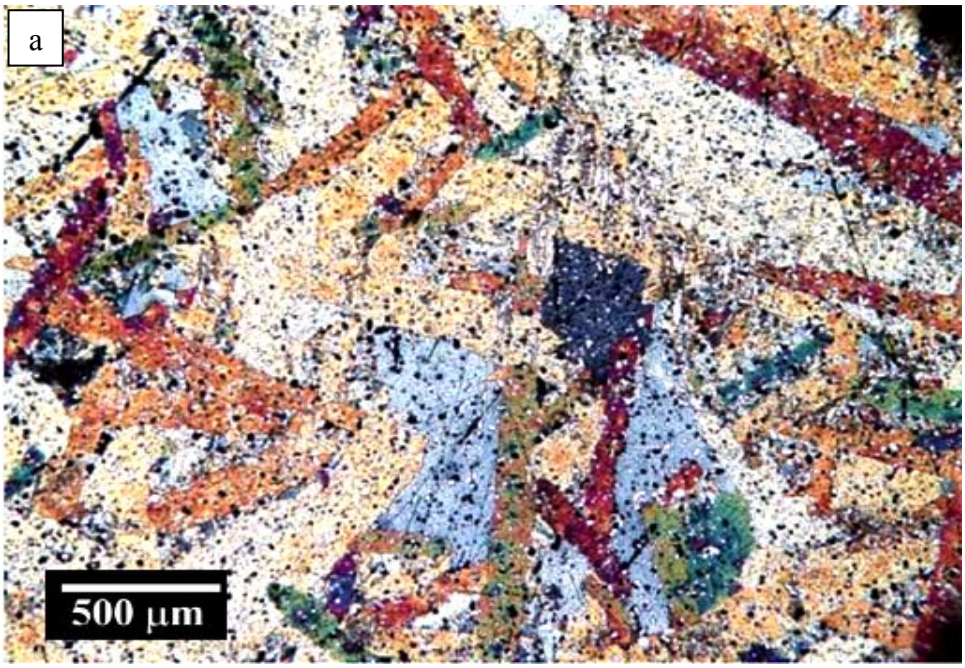

Figure 49: Typical OM micrographs of tapped and sintered Ti_3SiC_2 sample sintered at 1600 °C for 24 hrs. a) Top view showing large plate-like grains with their basal planes mostly parallel to the surface.

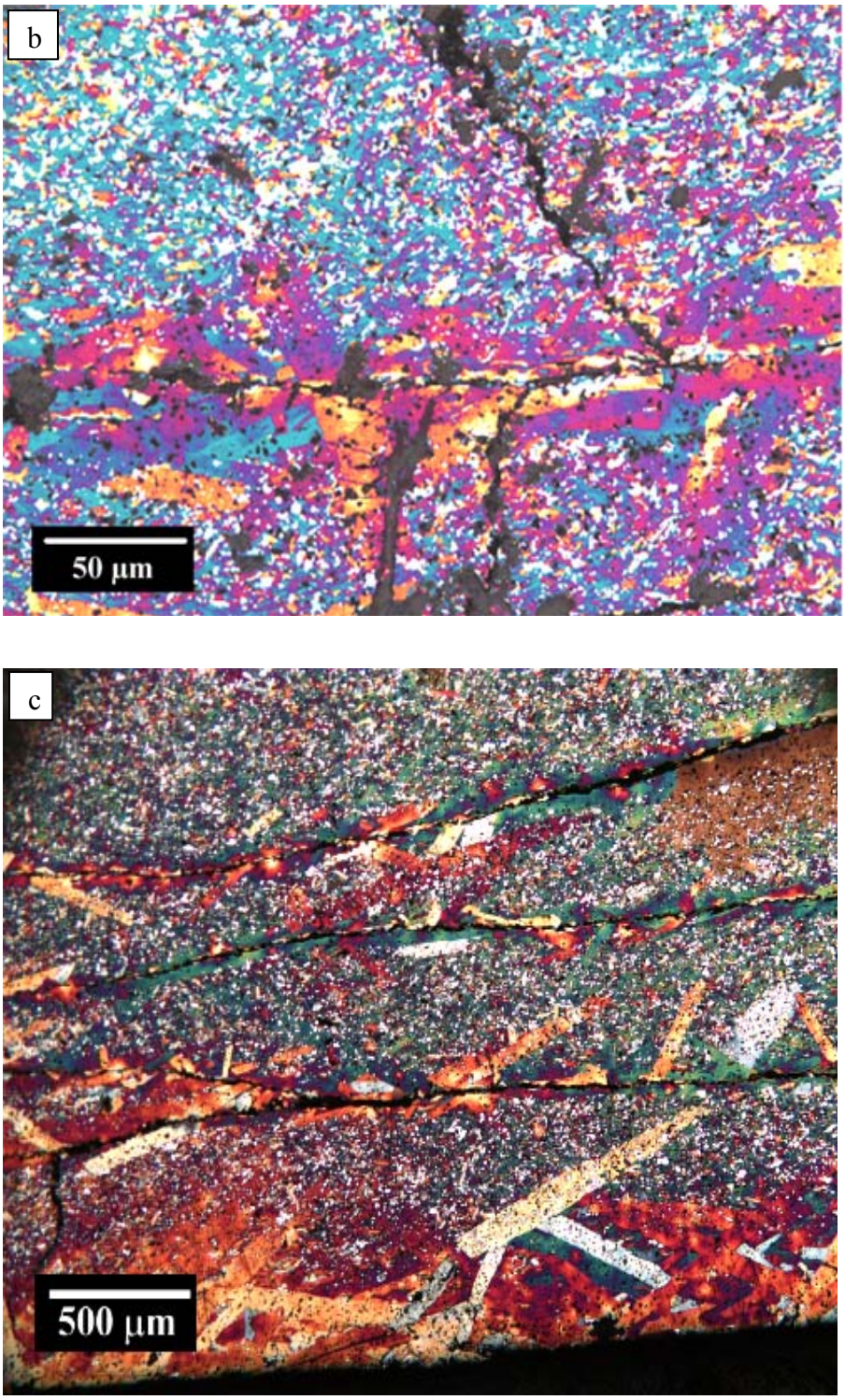

Figure 49: b) Cross-section showing large surface grains. c) In vicinity of cracks, the grains are larger than the core grains. In all micrographs, the white specs are TiCx.

An alternate explanation, albeit somewhat far-fetched, is that during cold-pressing and handling of the samples enough impurities are introduced near the surfaces to result in a liquid forming at the grain boundaries during sintering. Such a liquid would in turn greatly enhance grain boundary mobility. To eliminate that possibility we carried out the following experiment. A Ti_3SiC_2 compact was cold pressed in a steel die. The compact was then buried in more Ti_3SiC_2 powder and the entire assembly was in turn CIPed. This resulted in a good bond between the compact and the external powder bed, but clearly did not eliminate contamination from the die. Annealing this compact resulted in a microstructure (not shown) where the grains at the compact/powder interface were small, but the grains at the surface of the CIPed outer layer grew large. This experiment conclusively proves that; i) cold pressing is not responsible for the large surface grains, and, ii) the grains only grow large when they are adjacent to free surfaces and/or surface connected cracks.

In an attempt to orient the grains further without the use of binders such as in tape casting, the samples were made by building layers of oriented powders, one at a time as previously described (Fig. 45). The resulting samples had similar or only slightly better orientation compared to cold pressing. A few micrographs of the sample obtained by this process are shown in Fig. 50. However, though this process showed promise, it was discontinued due to the tedious and exhausting nature of the experiments and lack of reproducibility. The orientation of the powder in a layer depended on the thickness of the layer: the smaller the layer, better the orientation. However, very thin layers were difficult to handle and significantly increased the time to build to a certain thickness for the sample.

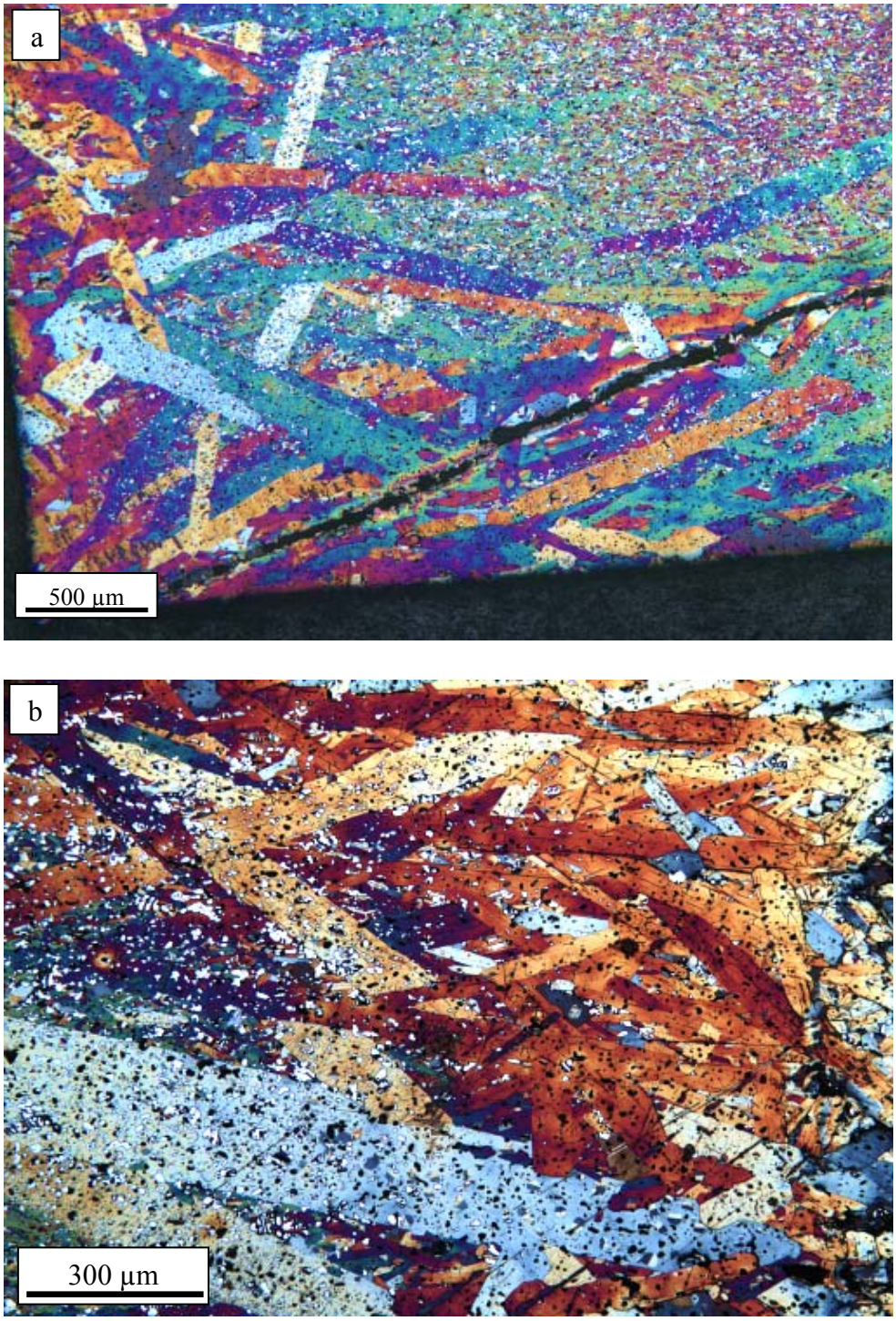

Figure 50**:** OM micrographs of sintered Ti_3SiC_2 sample made by building oriented powders layers, one at a time - sintered at 1600 °C for 24 hrs. a) Cross section showing both large surface grains and smaller core grains. b) Grains near the surface. The results were similar to tapped and sintered samples

Despite having clean and large grains at the surface, the problem of TiC_x and smaller grains at the core of the samples could not be eliminated. Thus, to over-come the loss of silicon and or saturation of carbon in the bulk (thus forming TiC_x), some of the cold pressed green compacts were surrounded by loose Ti_3SiC_2 powders during sintering in Argon atmospheres. This was done for two reasons: to increase the activity of silicon around the sample (thus preventing the loss of silicon), and to maintain the beneficial effect of Ar cleansing and/or thermally etching the powder surfaces near the compact surfaces (Fig. 51). The sample seemed to have lesser TiC_x, thus it was decided to further study the effects of silicon on the sintering and grain growth kinetics. Sintering the samples with silicon in the tube furnace however resulted in reaction of silicon with the refractory alumina tube, thus destroying the tubes. Thus, the studies were conducted in a vacuum furnace with graphite heating elements.

The microstructures of the three samples annealed at 1650 °C for 8 hrs in the vacuum furnace are shown in Fig. 52. The sample containing 10 wt. % Si had no TiC_x (Fig. 52a) Most importantly the microstructure was uniform; the grain size distributions at the surface (≈ 71±45 μm) and the core (74±41) were statistically indistinguishable (Table 2). This sample also contained some large voids (Fig. 52b) that probably formed as a result of the melting of Si aggregates. A closer look at one of the voids in the SEM (Fig. 52c) reveals the flaky morphology of the Ti_3SiC_2 grains. In some locations, the voids clearly showed evidence of a liquid phase – probably liquid Si or a silicide phase as shown in Figs. 52d and e.

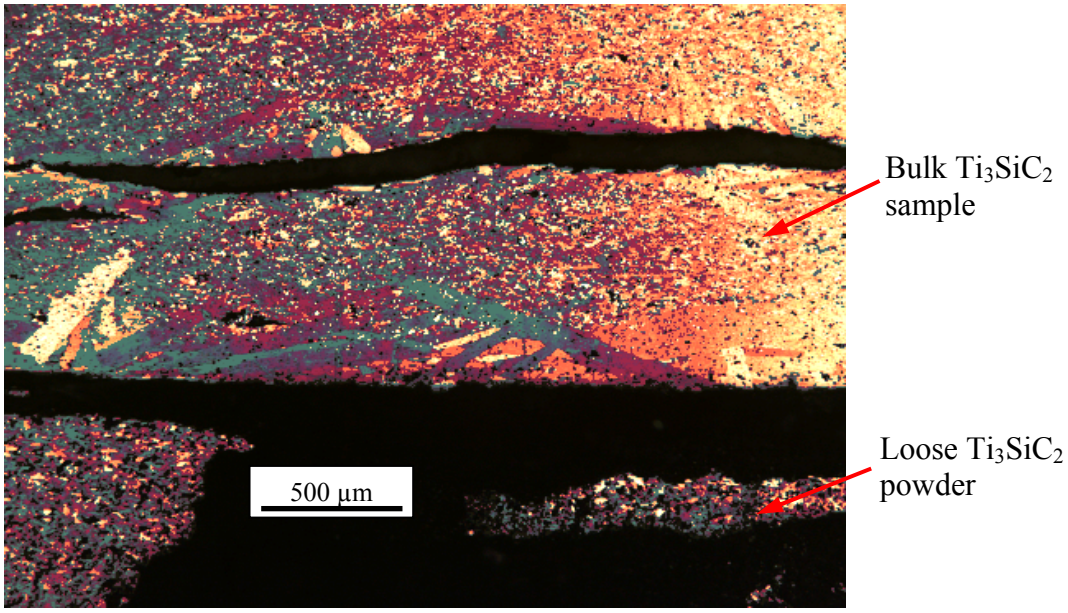

Figure 51: OM micrographs of tapped and sintered Ti_3SiC_2 sample covered with loose Ti_3SiC_2 powders, sintered at 1600 °C for 24 hrs. The surface grains are larger than the core grains. The loose powder surrounding the sample has also densified, the sample had lesser TiC_x.

The sample that was adjacent to a pool of molten Si also showed a uniform grain size distribution, wherein the grain size distributions, both in the core and at the surface, were also statistically indistinguishable (Fig. 53a and Table 2, row 8). The average grain size, however, was smaller than the sample for which the Si was mixed in with the Ti_3SiC_2 powders.

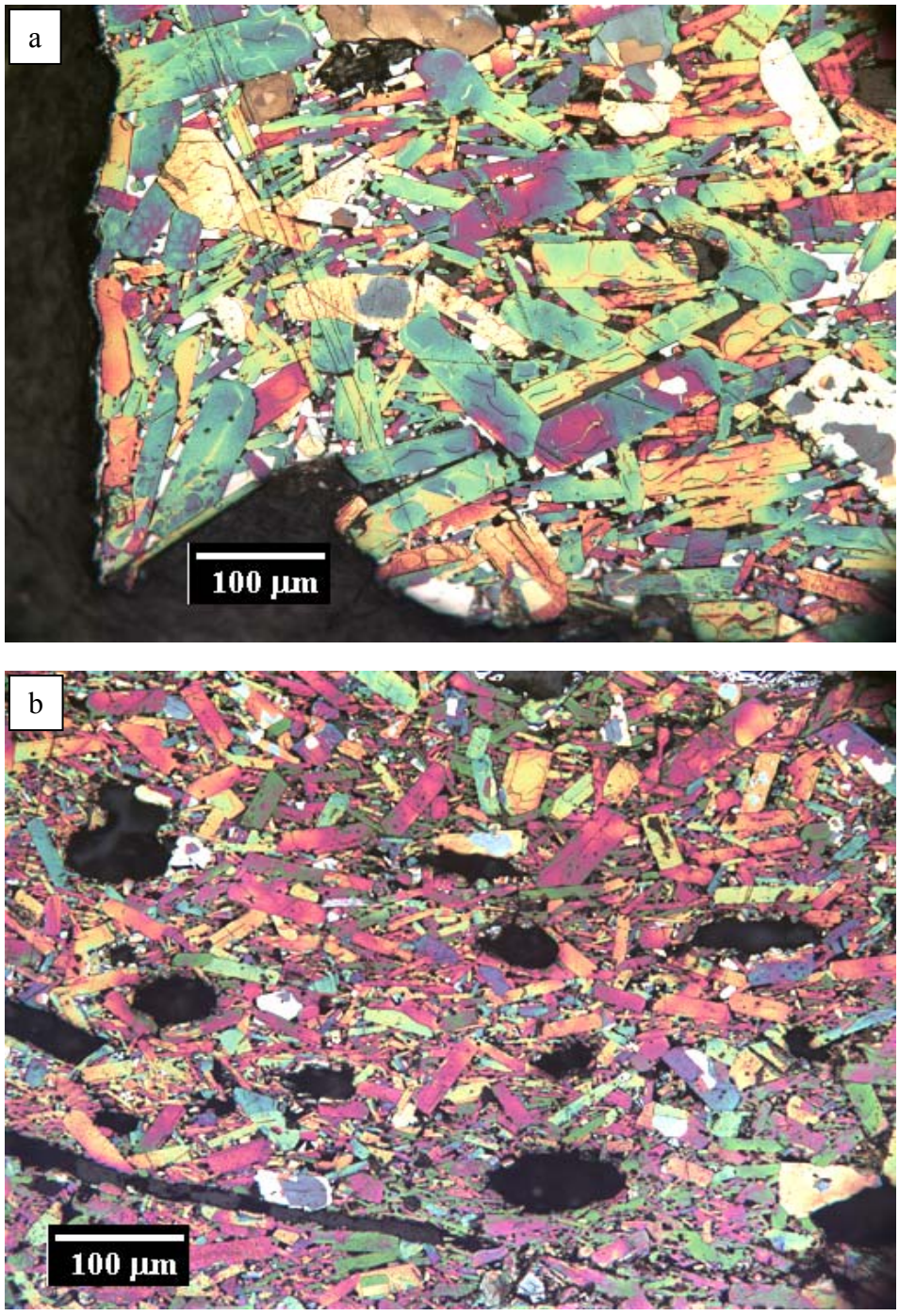

Figure 52: Micrographs of Ti_3SiC_2 compacts sintered for 8 hrs and 1650 °C for sample where 10 wt.% Si was mixed with Ti_3SiC_2. a) OM micrograph showing almost no TiC. b) Large voids in the sample possibly due to Si melting and forming aggregates.

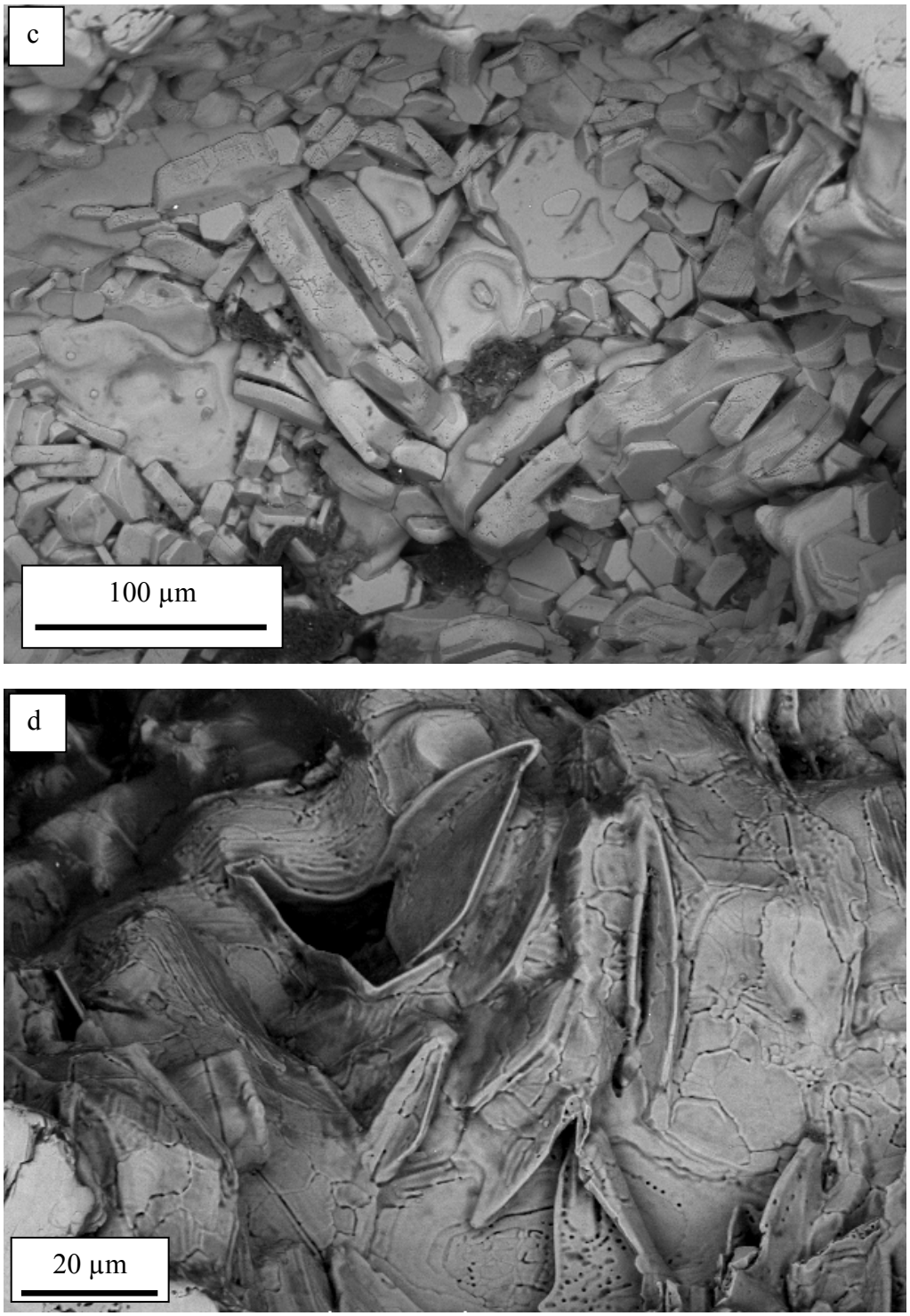

Figure 52: c) Backscattered SE image of one of the voids showing the plate like grains of Ti_3SiC_2. d) Backscattered SE image in another void showing evidence of a liquid phase that collected through the tiny pores or conduits

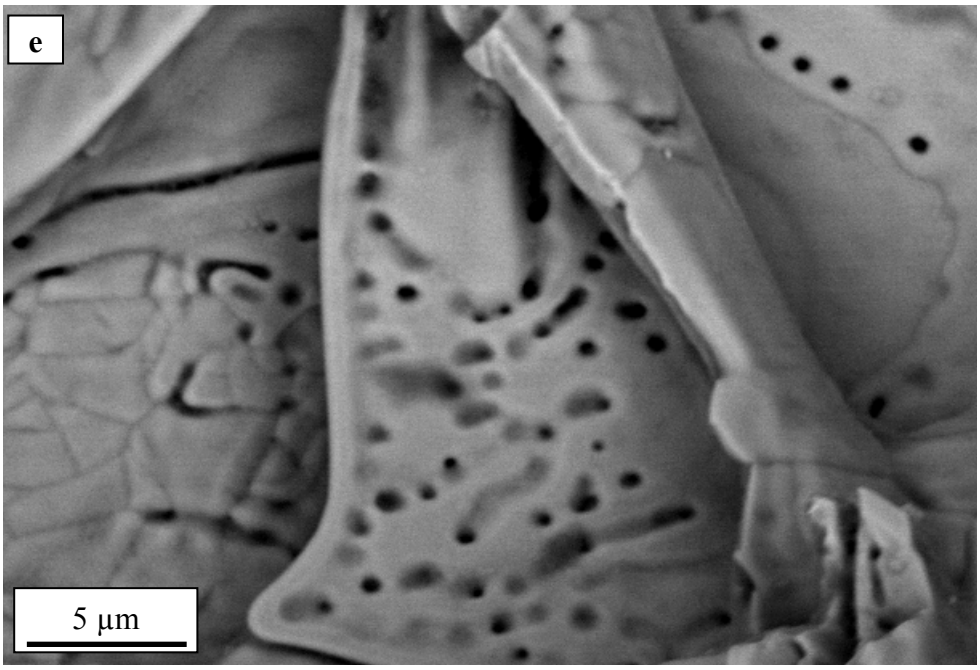

Figure 52: e) Magnified image of some of the tiny pores

Interestingly enough in some areas, the sintered compact was covered by large grains of SiC (surface grains in bottom left of micrograph shown in Fig. 53a). This is not too surprising given that SiC lies in the reaction path when Ti_3SiC_2 is in contact with Si [97]. In contradistinction, the control sample, placed in the vacuum hot press with no Si, was characterized by a ≈ 200 µm thick layer of pure TiC_x (Fig. 53b). At 13±7, the core grains were significantly smaller than the other two runs, once again confirming the potent role of TiC_x in reducing grain boundary mobility. This experiment is also in agreement with our previous finding that high C activities lead to loss of Si and the conversion of Ti_3SiC_2 to TiC_x [97].

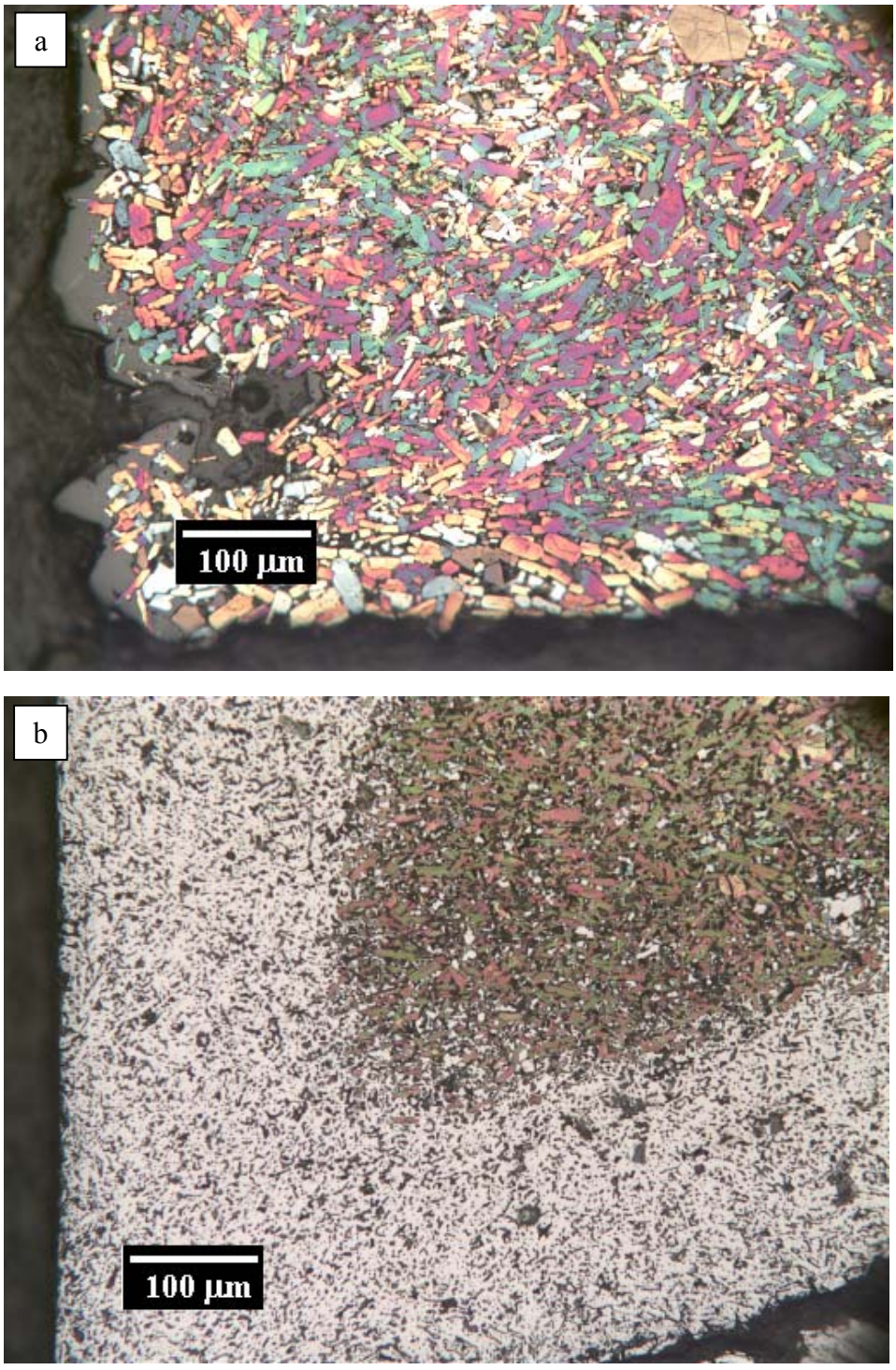

Figure 53: OM micrographs of Ti_3SiC_2 compacts sintered for 8 hrs and 1650 °C for: a) Ti_3SiC_2 compact was placed near, but not in contact with, silicon (note almost total absence of TiC_x). b) Control sample with no Si.

It is important to note that while the presence of Si eliminated the gradient in grain size from the center to the core, it did *not* enhance but rather *retarded* grain growth. Even after 8 h at 1650 °C, the grains were still significantly smaller than the surface grains of the pressed and Ar-sintered samples held for less time and lower temperatures (compare rows 4 and 7 in Table 2). These observations are important because they strongly suggest that the grain boundary phase that retards grain boundary migration of Ti_3SiC_2 powders must be Si-containing. Careful analysis of backscattered FESEM micrographs together (Fig. 54a) with EDS confirmed the grain boundary phase was a Ti-silicide, most likely $TiSi_2$; however, $Ti_3Si_5C_x$ cannot be ruled out at this time. To confirm that the phase was a silicide, polished samples were etched in a 1:1:1 by volume of $HF:HNO_3:H_2O$ for a few seconds. OM of the etched samples (Fig. 54b) clearly showed cavitations at the grain boundaries. When these samples were further annealed for 24 h at 1600 °C the grains grew significantly and rapidly (Fig. 54b and Table 2). The growth rate (≈ 150 μm in 24 h) was the fastest measured for both the core and surface grains in this work (Fig. 48 dashed line). As important, post-annealing examination of the grain boundaries showed them to be clean (Fig. 54b). These results suggest that annealing at 1600 °C for extended periods of time, results in the vaporization and/or dissolution of this Ti-silicide grain boundary phase.

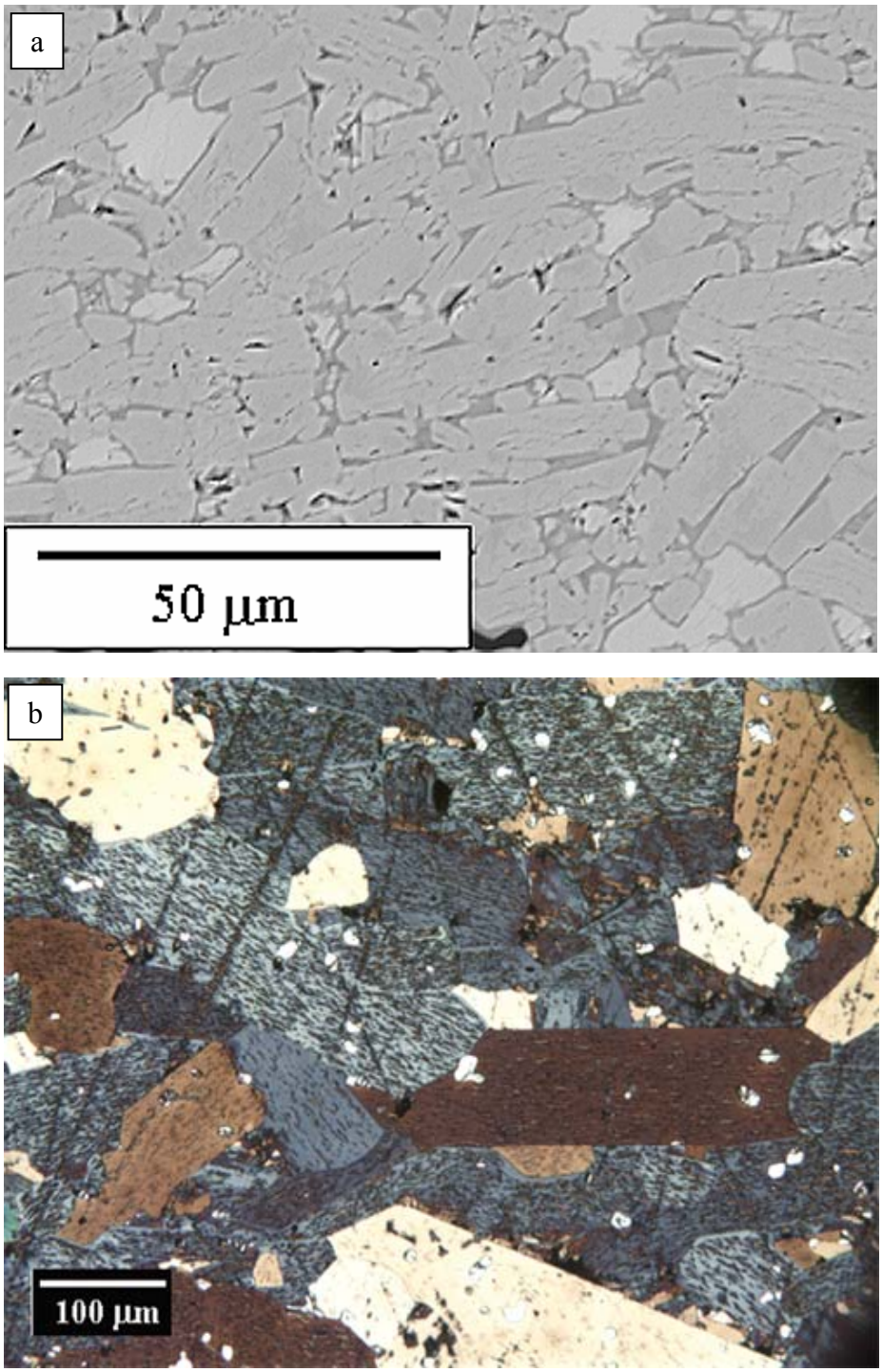

Figure 54: a) Backscattered SEM micrograph of cross-section of a Ti_3SiC_2 compact sintered near but not in contact with Si. Note dark grain boundary phase, which is most probably$TiSi_2$. Etching the samples dissolves the $TiSi_2$ in the grain boundaries. b) OM of sample shown in a, after further sintering further in Ar, with no Si present. There is no evidence for silicide phases.

The samples produced by the above methods, though had large grains were not used for the nanoindentation tests. This was due to the number of steps involved in sample preparation. Instead samples with very large oriented grains made by hot pressing were used for the nanoindentation testing.

VITA

EDUCATION

Ph.D. in Materials Science and Engineering, Drexel University, Philadelphia, PA, May 2004
MS in Mechanical Engineering, Louisiana State University, Baton Rouge, LA, Dec 1999
BS in Mechanical Engineering , Bharathidasan University, Trichy, India, Apr 1995

PUBLICATIONS

A. Murugaiah, M. W. Barsoum, S. Basu and J. Rabier, "Evidence $YBa_2Cu_3O_6$ is a Kinking Nonlinear Elastic Solid", *submitted for publication*
M. W. Barsoum, **A. Murugaiah**, S. R. Kalidindi and T. Zhen, "Kinking Nonlinear Elastic Solids, Nanoindentations and Geology", *Physical Review Letters, in press*
M. W. Barsoum, **A. Murugaiah**, S. R. Kalidindi, and Y. Gogotsi, "Nanoindentations and Kink Bands in Graphite Single Crystals**",** Carbon, **42**, 1435, 2004
A. Murugaiah, M. W. Barsoum, S. R. Kalidindi, and T. Zhen, "Spherical Nanoindentations and Kink Bands in Ti_3SiC_2", *Journal of Materials Research,* **19**, 1139-1148, 2004
A. Murugaiah, A. Souchet, T. El-Raghy, M. Radovic, Mats Sundberg and M. W. Barsoum, "Tape Casting, Pressureless Sintering and Grain Growth in Ti_3SiC_2 Compacts, *Journal of the American Ceramic Society*, **87,** 550-56, 2004
M. W. Barsoum, T. Zhen, S. Kalidindi, M. Radovic, **A. Murugaiah**, "Fully reversible, dislocation-based compressive deformation of Ti_3SiC_2 to 1 GPa" *Nature Materials, **2***, 107-111, 2003

HONORS AND AWARDS

Graduate Student Research Award 2003 - Recognition by the College of Engineering for Graduate Research Achievement, Drexel University
College of Engineering Dean's Award Winner for Best Poster at the 6th Drexel University Research Day [One of the top ten out of 450 posters presented], May 2004
First place, American Society of Materials, Philadelphia chapter annual graduate student poster competition, March 2004
First place, Graduate level research paper competition at the American Institute of Aeronautics and Astronautics (AIAA) Region IV Conf., Albuquerque, NM, 1999
Work (micrographs) published on the cover of the Journal of the American Ceramic Society, April 2004 and again in May 2004

AFFILIATIONS

American Society of Materials (ASM international), The Minerals, Metals, and Materials Society (TMS), The American Ceramic Society (ACERS), Materials Research Society (MRS), American Institute of Aeronautics and Astronautics (AIAA), 1998–99